Denoising and Compression of Digital Images using Wavelets

Nikhil Gupta

A Thesis

in

The Department

of

Electrical and Computer Engineering

Presented in Partial Fulfillment of the Requirements
for the Degree of Master of Applied Science at
Concordia University,
Montreal, Quebec, Canada

April 2004

Your file Votre référence
ISBN: 0-612-91038-5
Our file Notre référence
ISBN: 0-612-91038-5

ABSTRACT

Denoising and Compression of Digital Images using Wavelets

Nikhil Gupta

This thesis concentrates primarily on two problems that concern noise corrupted images and looks to the wavelet domain for the solutions.

Firstly, the issue of noise reduction in digital images is addressed. Most of the popular thresholding techniques are either subband adaptive, i.e., do not adapt spatially according to individual subband coefficients, or rely heavily on subband statistics for adaptation, which makes them computationally expensive. A low-complexity adaptation of the subband-optimal thresholds according to the individual coefficients is presented. The correlation that exists in consecutive subbands in wavelet domain is exploited to adapt the subband optimal thresholds using the magnitude of the corresponding parent coefficients. Using simulated experiments, the ability of the proposed algorithm to preserve the edges and fine details in an image, while successfully reducing the noise from the smooth regions, is demonstrated.

Secondly, the relatively uncharted area of simultaneous denoising and compression of images that are corrupted with noise is explored. A data adaptive subband (wavelet) coder that performs joint denoising and compression of the input image based on both the additive white Gaussian noise level in the image and the compression rate desired is developed. A simple uniform threshold quantizer (UTQ), with centroid reconstruction, is adapted to have a joint noise level (data) and output bitrate adaptive zero-zone and reconstruction. To improve the performance of this variable-rate-coder, a context-based classification scheme that improves the quantization of the fine detail in the image is also proposed.

The joint denoising and compression scheme is further extended for the removal of multiplicative speckle from medical Ultrasound images using homomorphic filtering.

ACKNOWLEDGEMENTS

It has been a great privilege for me to work with Dr. M. N. S. Swamy and Dr. Eugene Plotkin, my research advisers, who introduced me to signal processing in wavelet domain and allowed me to pursue research in image processing, a subject close to my heart. Exceptional teachers and researchers, they have been extra-ordinarily patient and supportive, having been always available for discussion and speedily responding to queries and research reports. I would like to take this opportunity to thank them for their continued encouragement and guidance through the course of my research.

I sincerely thank Dr. Purnendu Sinha, Dr. Aishy Amer, Dr. William Lynch and Dr. Weiping Zhu for insightful and timely discussions on research related problems at one point or another during the course of this thesis.

I extend my whole-hearted gratitude to my family for their encouragement and support, without which it would have been impossible to finish this work. Finally, I would like to thank my colleagues at CENSIPCOM and my friends for their valuable discussions, support and advice.

Nikhil Gupta, April 2004

I dedicate this work to my loving family ...

Contents

List of Figures ix

List of Tables xiii

List of Algorithms xv

List of Symbols xvi

List of Abbreviations xviii

1 Introduction 1

1.1 Introduction and motivation 1

1.2 Scope of the thesis 4

1.3 Organization of the thesis 5

2 Introduction to Wavelets 7

2.1 From Fourier transform to wavelets 7

2.2 Why wavelets? 10

2.3 Wavelets and multi-resolution analysis 11

2.3.1 Multi-resolution analysis 11

2.3.2 Wavelet functions 12

2.3.3 The fast wavelet transform (FWT) 13

2.3.4 Orthogonal wavelets 14

2.3.5 Bi-orthogonal wavelets 15

2.3.6 Higher dimensions 17

2.4 The wavelet transform and translation invariance 19

3 Image Denoising Using Wavelets 21

3.1 Introduction 21

3.2 Input signal models and notations 22

3.2.1 Time domain representation 22

3.2.2 Wavelet domain representation 23

3.3 Noise variance estimation 25

3.4 State-of-the-art overview of wavelet domain denoising 26

3.4.1 Image denoising using wavelet thresholding 26

3.4.2 Image denoising using multi-scale products 28

3.4.3 Bayesian methods for image denoising 29

3.5 Denoising by wavelet thresholding 30

3.5.1 Hard and soft thresholding 31

3.5.2 Threshold selection 32

3.6 Hierarchical adaptation of thresholds 36

3.7 Image denoising algorithm 37

3.8 Performance evaluation in image denoising 39

3.9 Experimental results and discussions 39

4 Joint Denoising and Compression of Images 48

4.1 Introduction and motivation 48

4.2 Problem statement 49

4.3 Data and rate adaptive quantizer 51

4.4 Optimal bit allocation 56

4.5 Context-based classification 58

4.5.1 Activity computation 59

4.5.2 Classification thresholds 60

4.6 Final algorithm for joint denoising and compression of images 60

4.7 Joint denoising and compression of medical ultrasound images 63

4.7.1 Introduction 63
4.7.2 Speckle noise model and the modified algorithm 64
4.8 Experimental results and discussions 68
4.8.1 For additive White Gaussian noise 68
4.8.2 For multiplicative speckle noise 79
4.9 Summary 85

5 Conclusion **87**
5.1 Conclusion 87
5.2 Future work 89

References **91**

List of Figures

2.1 Time-frequency tilings and the basis functions for the (a) Fourier, (b) short time Fourier, and (c) wavelet transforms. 9

2.2 The filter bank algorithm for orthogonal wavelets: filtering and down-sampling of the signal I yields the low-pass signal LP and the high-pass signal HP. Signal S is reconstructed by up-sampling and filtering with the corresponding filters. In case of perfect reconstruction, the input and the output signals are the same 14

2.3 Orthogonal scaling and wavelet functions. (a) Daubechies scaling function with 4 vanishing moments, (b) Daubechies wavelet function with 4 vanishing moments, (c) Scaling function for the least asymmetric compactly supported wavelet, Symmlet, with 8 vanishing moments (Symmlet-8), and (d) Symmlet-8 wavelet function. 16

2.4 The filter bank algorithm for bi-orthogonal wavelets: filtering and down-sampling of the signal I yields the low-pass signal LP and the high-pass signal HP. Signal S is reconstructed by up-sampling and filtering with the corresponding filters. The filters used for decomposition are the dual of the ones used for reconstruction. In case of perfect reconstruction, the input and the output signals are the same 17

2.5 Scaling and wavelet functions for the Bi-orthogonal 1-3 case. (a) Dual scaling function, (b) Dual wavelet function, (c) Scaling function, and (d) Wavelet function. 18

2.6 The two-dimensional wavelet transform (square variant) with two successive levels of decomposition. 19

2.7 The filter bank algorithm for a two-dimensional orthogonal wavelet transform of the two-dimensional signal I (e.g., image). The one dimensional transform is first applied along the columns and then on each row. The resultant output has the same size as the input signal. 20

3.1 (a) Test image *Lena*, and (b) 3-level dyadic wavelet decomposition of the test image using Symmlet-8 orthogonal wavelet. The detail subbands have been scaled for display purposes. 22

3.2 The subband structure for a 4-level DWT decomposition and the parent-child relationship among the wavelet coefficients in successive subbands. 24

3.3 (a) Hard-thresholding of a noisy signal, and (b) Soft-thresholding of a noisy signal 33

3.4 Block diagram for image denoising in the wavelet domain using hierarchically adapted thresholding 38

3.5 Performance comparison for different denoising methods with *Lena* corrupted with AWGN having $\sigma = 20$ as input. 43

3.6 Performance comparison for different denoising methods with *Goldhill* corrupted with AWGN having $\sigma = 35$ as input. 44

3.7 Performance comparison for different denoising methods with *Barbara* corrupted with AWGN having $\sigma = 30$ as input. 45

3.8 Performance comparison for different denoising methods with *Mandrill* corrupted with AWGN having $\sigma = 20$ as input. 46

4.1 Similarity between soft-thresholding used for denoising in the wavelet domain and quantization used for compression 50
4.2 Data and rate adaptive quantizer: (a) $\Delta_Z > T_B$; (b) $\Delta_Z < T_B$ 54
4.3 (a) Causal template composed of 6 quantized coefficients that is used as the classification context, (b) Classification of the predicted activity into different classes 59
4.4 Block diagram of the data and rate adaptive encoder for images corrupted with AWGN. 62
4.5 Block diagram of the data and rate adaptive encoder for medical ultrasound images corrupted with multiplicative speckle noise. 67
4.6 The Q-Q plot of the HL_1 subband coefficients of image *Lena* against a Laplacian distributed set of data. The magnitude of the subband coefficients has been taken for the plot. 69
4.7 4-level classification of one subband each of *Lena* and *Barbara* images corrupted with AWGN having $\sigma = 20$ 71
4.8 (a)-(e) Performance comparison of various methods on *Goldhill* corrupted with AWGN having $\sigma = 25$. (f) Rate-Distortion curve for the proposed methods with *Goldhill* corrupted with AWGN having $\sigma = 25$ as input. 73
4.9 (a)-(e) Performance comparison of various methods on *Lena* corrupted with AWGN having $\sigma = 35$. (f) Rate-Distortion curve for the proposed methods with *Lena* corrupted with AWGN having $\sigma = 15$ as input. . 74
4.10 (a)-(e) Performance comparison of various methods on *Barbara* corrupted with AWGN having $\sigma = 15$. (f) Rate-Distortion curve for the proposed methods with *Barbara* corrupted with AWGN having $\sigma = 10$ as input. 75

4.11 (a)-(e) Performance comparison of various methods on *Mandrill* corrupted with AWGN having $\sigma = 10$. (f) Rate-Distortion curve for the proposed methods with *Mandrill* corrupted with AWGN having $\sigma = 10$ as input. 76

4.12 (a)-(e) Performance comparison of various methods on *Synthetic* corrupted with AWGN having $\sigma = 20$. (f) Rate-Distortion curve for the proposed methods with *Synthetic* corrupted with AWGN having $\sigma = 20$ as input. 77

4.13 Comparing the effect of classification on the performance of the subband coder having the data and rate adaptive quantizer at its core. . 78

4.14 Rate-Distortion curves comparing the performance of the proposed scheme with JPEG compression and a two stage scheme wherein the speckled image is first despeckled using Frost filter and then compressed using JPEG compression standard. The comparison has been made for the speckled Lena image with ENL=14 and PSNR=17.90 dB. The 5x5 window has been chosen for the design of the Frost filter. 81

4.15 Performance comparison of the proposed scheme with JPEG compression and a two-stage scheme where the speckled image is first denoised and the compressed using the corrupted *Lena* image. 82

4.16 Performance comparison of the proposed scheme with JPEG compression and a two-stage scheme where the speckled image is first denoised and the compressed using the corrupted *Goldhill* image. 83

4.17 Performance comparison of the proposed scheme with JPEG compression and a two-stage scheme where the speckled image is first denoised and the compressed using the original speckle corrupted Ultrasound image, *Brain*. 84

List of Tables

3.1 PSNR results for denoising experiments with *Lena* image corrupted with different noise powers. 40

3.2 PSNR results for denoising experiments with *Barbara* image corrupted with different noise powers. 40

3.3 PSNR results for denoising experiments with *Boat* image corrupted with different noise powers. 40

3.4 PSNR results for denoising experiments with *Mandrill* image corrupted with different noise powers. 41

3.5 PSNR results for denoising experiments with *Goldhill* image corrupted with different noise powers. 41

3.6 PSNR results for denoising experiments with *Airplane* image corrupted with different noise powers. 41

3.7 PSNR results for denoising experiments with *House* image corrupted with different noise powers. 41

3.8 PSNR results for denoising experiments with *Peppers* image corrupted with different noise powers. 42

3.9 PSNR results for denoising experiments with *Cameraman* image corrupted with different noise powers. 42

3.10 PSNR results for denoising experiments with *Monarch* image corrupted with different noise powers. 42

3.11 Averaged PSNR results for denoising experiments. 42

4.1 Mean and variance of coefficients in different classes for a 4-level classification of the HL_2 detail subband of *Lena* and the HL_1 detail subband of *Barbara*. 70

4.2 Performance comparison (in PSNR) for the test image *Goldhill* corrupted with different additive noise powers. 70

4.3 Performance comparison (in PSNR) for the test image *Lena* corrupted with different additive noise powers. 70

4.4 Performance comparison (in PSNR) for the test image *Barbara* corrupted with different additive noise powers. 70

4.5 Performance comparison (in PSNR) for the test image *Mandrill* corrupted with different additive noise powers. 72

4.6 Performance comparison (in PSNR) for the test image *Synthetic* corrupted with different additive noise powers. 72

4.7 Performance comparison (in PSNR) for the test image *Lena* corrupted with different multiplicative noise powers. 80

4.8 Performance comparison (in PSNR) for the test image *Goldhill* corrupted with different multiplicative noise powers. 80

List of Algorithms

1 Image denoising using hierarchically adapted threshold 38

2 Optimal bit allocation using the generalized BFOS algorithm 57

3 Estimation of classification thresholds 61

4 Proposed scheme for joint denoising and compression of images corrupted with AWGN 61

5 Modified algorithm for joint denoising and compression of ultrasound images corrupted with multiplicative speckle 66

List of Symbols

$\phi(x)$	:	scaling or father function
$\psi(x)$	:	wavelet or mother function
$\widetilde{\phi}(x)$	:	dual scaling or father function
$\widetilde{\psi}(x)$	:	dual wavelet or mother function
h_k	:	low-pass filter coefficients
g_k	:	high-pass filter coefficients
$\widetilde{h}_k$	:	dual low-pass filter coefficients
$\widetilde{g}_k$	:	dual high-pass filter coefficients
$\langle ., . \rangle$	:	inner product
$\overline{x}$	:	closure of the set x
$p_y(y)$	:	probability density function of the random variable y
$p_y(y)$	:	probability density function of the random variable y
$\mathbf{x}$	:	matrix of discrete image pixel values in time domain
ε	:	matrix of additive noise in time domain
$\mathbf{g}$	:	matrix of corrupted pixel values in time domain
$\sigma, \widehat{\sigma}$	:	standard deviation of the corrupting additive white Gaussian noise and its estimate
$\sigma_X, \widehat{\sigma}_X$	:	standard deviation of the noise-free coefficients in a subband and its estimate
σ_Y	:	standard deviation of the noisy coefficients in a subband

$\mathbf{W}$, $\mathbf{W}^{-1}$	:	two dimensional discrete wavelet transform matrix and its inverse
$\mathbf{X}$, $\widehat{\mathbf{X}}$	:	matrix of wavelet coefficients of the original image and its estimate
$\mathbf{N}$	:	matrix of wavelet coefficients of the additive white Gaussian noise
$\mathbf{Y}$	:	matrix of wavelet coefficients of the corrupted image
$\mathbf{P}$	:	matrix of parent coefficients
$\widetilde{\mathbf{X}}$	:	soft-thresholded matrix of coefficients
T	:	threshold parameter value
T_B	:	threshold estimated as per the *BayesShrink* rule
N, M	:	number of rows and columns in the image
K, L	:	number of rows and columns in a subband
N_s	:	total number of coefficients in a subband
D_s, D	:	distortion for each subband and the total distortion
$\lambda, \widehat{\lambda}$	:	mean of the exponentially distributed random variables and its estimate
Δ	:	zero zone of the uniform threshold quantizer
b_j, r_j	:	break-points and reconstruction levels of the uniform threshold quantizer
M_{ij}	:	activity for the wavelet coefficient at location (i, j) in a subband
$\mathbf{v}$	:	matrix of image pixels corrupted by multiplicative noise
η	:	matrix of multiplicative speckle noise

List of Abbreviations

AQ	:	encoder with data and rate adaptive quantizer
AWGN	:	additive white Gaussian noise
C+AQ	:	encoder with classification and data and rate adaptive quantizer
CCD	:	charge coupled device
CDF	:	Cohen , Daubechies and Feauveau
DCT	:	discrete cosine transform
DWT	:	discrete wavelet transform
ECSQ	:	entropy-constrained scalar quantizer
ENL	:	equivalent number of looks
ENO	:	essentially non-oscillatory
FWT	:	fast wavelet transform
GGD	:	generalized Gaussian distribution
GSM	:	Gaussian scale mixture
HA	:	hierarchically adapted
HVS	:	human visual system
iid	:	independent and identically distributed
MDL	:	minimum description length
MDLQ	:	joint denoising and compression scheme based on MDL
MLE	:	maximum likelihood estimate
MMSE	:	minimum mean squared error

MPM	:	multi-scale product methods
MRA	:	multi-resolution analysis
MRF	:	Markov random field
MSE	:	mean squared error
PSNR	:	peak signal to noise ratio
R-D	:	rate-distortion
SNR	:	signal to noise ratio
STFT	:	short-time Fourier transform
SURE	:	Stein's unbiased risk estimate
UTQ	:	uniform threshold quantizer

Chapter 1

Introduction

1.1 Introduction and motivation

The phenomenal growth of the Internet, along with the ubiquitous use of digital cameras, scanners and camera phones have made the capture, display, storage and transmission of images, a routine experience. In addition, imaging is extensively used in medicine, law enforcement, Internet gaming and data collected by satellites. Inspired by the enhanced computing powers of the modern day computer and the ubiquitous presence of sensing devices, scientists are collecting and analyzing data at an ever increasing pace. Owing to natural human proclivity toward visual or pictorial representation of this data, more and more of the scientific data being generated is in the form of images.

In many fields such as astronomy, medical imaging, and computer vision, the data that is collected is often noisy as a result of data acquisition processes or due to natural phenomena such as atmospheric disturbances. Even acquiring an image with the use of a digital camera corrupts the image of the scene with the noise generated by the capturing media (such as the CCD sensors). Furthermore, noise is added to the data when it is transmitted over transmission channels. Noise is as common to

the image data generated as the data itself.

The corrupting noise might result in degradation of the visual quality of the images and may also mask important image information. Even if the perceived images do not show noise degradation due to the masking effects of the human visual system, many image analysis tasks, such as segmentation, might suffer in the presence of noise. Thus, it becomes imperative that the level of the noise present in digital images be reduced prior to any further processing.

Removing noise from data can be considered as the process of constructing optimal estimates of the unknown signal or image from the available noisy data. Spatial filters have long been used as the traditional means of removing noise from the images and signals [1]. These filters usually smooth the data to reduce the noise, but, in the process, also blur the data.

In general, image denoising imposes a compromise between noise reduction and preserving significant image details. To achieve a good performance in this respect, a denoising algorithm has to adapt to image discontinuities. In the last decade, several new techniques have been developed that improve on spatial filters by removing the noise more effectively while preserving the edges in the image. Some of these techniques borrow ideas from partial differential equations and computational fluid dynamics such as level set methods [2, 3], total variation methods [4, 5], nonlinear isotropic and anisotropic diffusion [6, 7], and essentially non-oscillatory (ENO) schemes [8]. Other techniques involve impulse removal filters with local adaptive filtering in the transform domain to remove not only white and mixed noise, but also their mixtures [9].

A different class of methods exploits the decomposition of the image data into the wavelet domain[10, 11, 12, 13, 14, 15, 16, 17]. The wavelet representation naturally provides a useful tool in the construction of spatially adaptive algorithms that can preserve edges in an image. It compresses the essential information in a signal into

a few, large coefficients which represent image signal details at different resolution scales and facilitates the removal of the corrupting noise. This sparse representation of the data in the wavelet domain also makes them ideal for compression applications. In addition, the human visual system (HVS) also employs multi-resolution decomposition to process the visual images.

It is this ability of the wavelet transform to form a bridge between theory and applications, and provide a suitable representation for processing the image data, that has enabled it to emerge as an important tool in denoising images.

Another aspect associated with this ever-increasing generation and transmission of digital images is the storage media. Despite rapid improvements in data storage, processing speeds, and digital communication system performance, this proliferation of digital media often outstrips the amount of data storage and transmission capacities. Thus, the compression of such signals has assumed great importance in the use, storage and transmission of digital images. However, this compression of the input images, performed in order to reduce the amount of storage space and transmission bandwidth required, also suffers in the presence of corrupting noise. The corrupting noise, being random in nature, tends to increase the entropy of the image data and as a result, causes more distortion in the compressed images for an available quota of bits. Despite this fact, the compression algorithms very seldom account for this corrupting noise. In the case where the input images are corrupted, the following scenarios are possible:

- The noisy images would be compressed as they are, which would result in increased distortion in the compressed images.
- Human intervention is provided to decide which image to denoise before compression, which, in view of the enormous amount of data, is practically impossible.

- All the images are passed through a denoising algorithm before they are compressed. Not only would this serve to increase the cost of the system, but would also tend to add further distortion in the output as the denoising algorithms generally do lead to some loss of information in case the corrupting noise level is low.

None of the solutions described are perfectly satisfactory when the input data would be corrupted with varying powers of noise. Thus, there is a need for compression algorithms that can adaptively remove any noise that occurs in an input image.

1.2 Scope of the thesis

The discussion provided in the previous section serves to establish the fact that noise corrupts all kinds of images: natural, scientific or medical. This thesis is concerned primarily with the following two problems associated with images corrupted with noise:

- Removal of noise from digital images.
- Compressing images corrupted with varying noise powers.

We investigate the wavelet domain for formulating solutions that address the considered problems.

Since additive white Gaussian noise is the most common type of noise that corrupts images and is also studied extensively in literature, we primarily consider this kind of noise in this thesis. However, keeping in view the prevalence of multiplicative speckle noise in images generated using scientic and medical processes, we also consider images corrupted with this kind of noise.

We try to provide solutions to these problems that yield better results than the ones already existing in the literature. In doing so, we merge theory and practice,

and employ heuristics too. The necessary review of the existing literature for each of the above problems is provided in the relevant chapters.

1.3 Organization of the thesis

This thesis is organized as follows. In Chapter 2, the background knowledge on wavelet theory is reviewed. Attempt is made to present a concise, yet self-contained review emphasizing the most relevant aspects for the topic of this thesis. We describe the benefits of the use of wavelets over the Fourier transform for the purpose of image denoising and compression. The multi-resolution analysis (MRA) of the input signal using wavelets is presented. We also describe the fast version of the discrete wavelet transform that is commonly employed in signal processing, using both orthogonal and bi-orthogonal wavelet families.

In Chapter 3, we explain the denoising of images in the wavelet domain. The signal notations employed throughout this thesis are explained. A detailed state-of-the-art overview pertinent to wavelet domain denoising of images is provided in this section. We describe denoising of images using thresholding of wavelet coefficients and present two commonly used methods for threshold estimation, *BayesShrink* [11] and *SureShrink* [14]. In the second half of the chapter, we present a new approach to hierarchically adapt these pre-existing thresholds. A comparative study of the original and the adapted thresholds is provided, via the use of simulations, to evaluate the performance of the proposed adaptation.

Chapter 4 presents our contribution toward the joint compression and denoising of images in the wavelet domain. We explain the adaptation of the uniform threshold quantizer (UTQ) and its application in a subband coder in wavelet domain. We also present a classification scheme to classify the data in order to improve the performance of the proposed coder. Simulated experiments are provided to show the efficacy of the

proposed schemes. The proposed joint compression and denoising scheme is applied to compress the images resulting from medical ultrasound scans. Such images are corrupted by multiplicative noise, and with the help of experiments we show that the proposed scheme works better than the compression methods normally used to compress such images. We also show the advantage of our scheme as compared to a two stage procedure, where the ultrasound image is first despeckled using a filter and then compressed.

In Chapter 5, we conclude this thesis by summarizing the results obtained and discuss some future work to be carried out.

Chapter 2

Introduction to Wavelets

This chapter presents an overview of wavelets and multi-resolution analysis. These can be found in many books and papers at many different levels of exposition. Some of the standard books are [18, 19, 20, 21, 22, 16]. Introductory papers include [23, 24, 25], and more technical ones are [26, 27, 28].

2.1 From Fourier transform to wavelets

In wavelet analysis, a signal f is decomposed into a basis of functions ψ_i:

$$f = \sum_i a_i \psi_i. \tag{2.1}$$

For an efficient decomposition of the signal f, a suitable family of the functions ψ_i is required that can represent the given signal using only a few coefficients a_i. These functions, ψ_i, should match the features of the signal to be decomposed.

Real-world signals usually are limited both in time (or space as in the case of images) and limited in frequency (band-limited). Time-limited signals can be represented efficiently using a basis of block functions (Dirac delta functions for infinitesimal small blocks). But block signals are not limited in frequency. Band-limited

signals can be represented efficiently using a Fourier basis, but sines and cosines are not limited in time. The Fourier representation reveals the spectral content of a signal, but makes it impossible to recover the particular moment in time (or the particular space coordinates in case of images) where a certain change has occurred. This makes the Fourier representation inadequate when it comes to analyzing transient signals. The corresponding time-frequency tilings of the Fourier transform are illustrated in Figure 2.1(a) along with the basis function.

In signal and image processing, concentrating on transients (such as image discontinuities) is a strategy for selecting the most essential information from often an overwhelming amount of data. In order to facilitate the analysis of transient signals, i.e., to localize both the frequency and the time information in a signal, numerous transforms and bases have been proposed (see e.g., [20, 22]). Among these, in signal processing, the wavelet and the short time Fourier Transform (STFT) are quite standard.

In the STFT transform (which is also called the window Fourier transform or the Gabor transform), the signal is multiplied by a smooth window function (typically Gaussian) and the Fourier integral is applied to the windowed signal. For a signal $f(x)$, the STFT is [20]

$$S(\tau, \omega) = \int_{-\infty}^{+\infty} f(x) g(x - \tau) e^{-j\omega x} dx, \tag{2.2}$$

where $g(x)$ is the window function. Note that the basis functions of a STFT expansion are $g(x)$ modulated by a sinusoidal wave and shifted in time, i.e., the modulation frequency is changing while the window remains fixed. A few of these functions and the corresponding tilings [29] of the time-frequency plane along with the basis functions are illustrated in Figure 2.1(b).

This gives rise to the need of a basis consisting of functions that are both time-

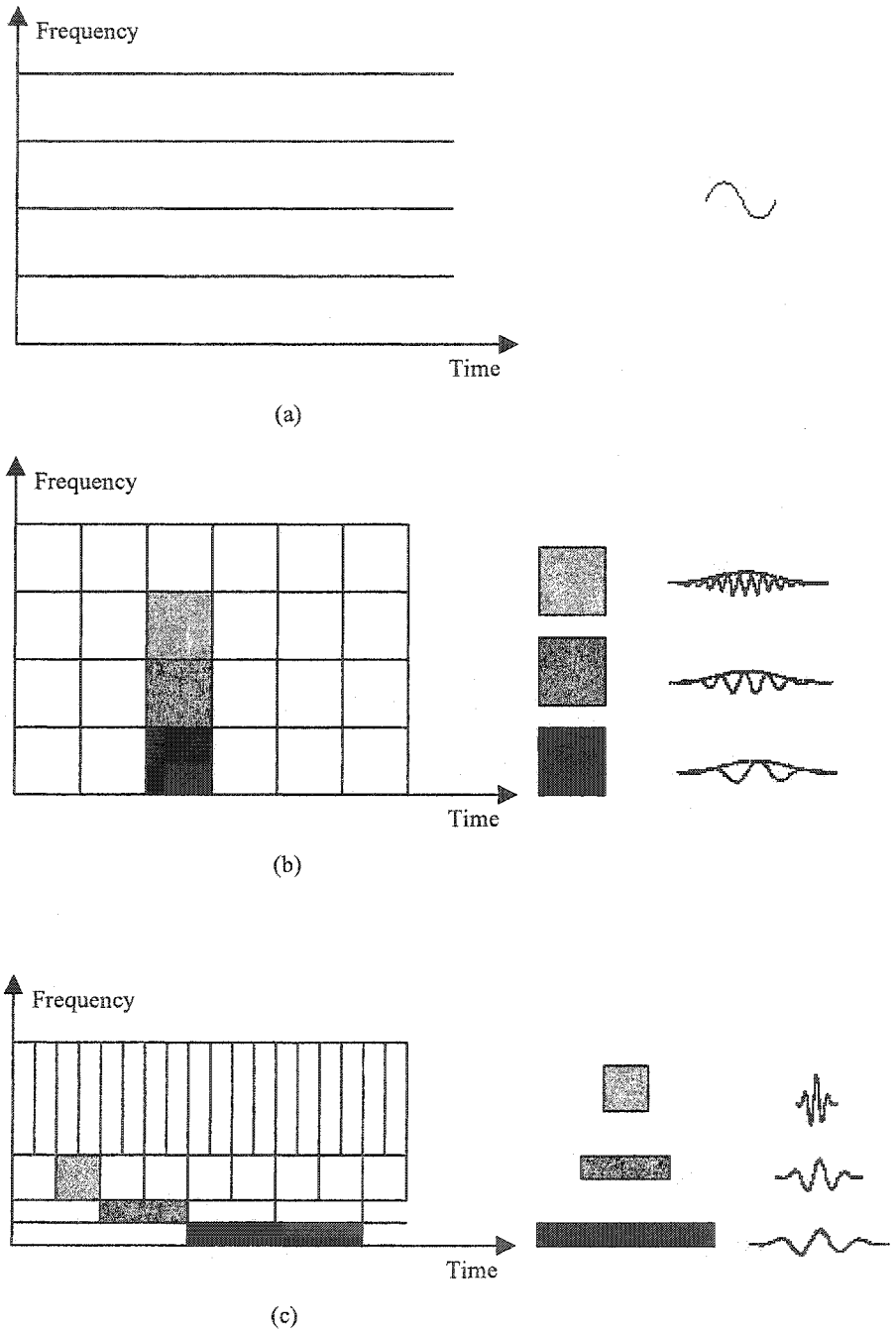

Figure 2.1: Time-frequency tilings and the basis functions for (a) the Fourier, (b) the short time Fourier and (c) the wavelet transforms.

limited and band-limited. Wavelets are such functions which literally mean small waves, and have been termed so due to the requirements that they should integrate to zero, waving above and below the axis, and that they should be localized. In wavelet analysis, the scale can be interpreted as the inverse of frequency. The corresponding tilling of the time-frequency plane and the wavelet bases are illustrated in Figure 2.1(c). As opposed to STFT, which divides the time-frequency plane into equal blocks, the wavelet transform acts as a microscope [22] focusing on smaller time phenomena as the scale decreases. This behavior permits a local characterization of signals, which the Fourier and the window Fourier transforms do not.

2.2 Why wavelets?

Two of the main features of wavelets that are important for the applications that we shall consider are their good decorrelation and sparse representation of signals. Wavelets not only represent the signals sparsely by concentrating most of the energy in a few number of coefficients, they also act as edge detectors. They cluster the coefficients having significant amount of energy near one another. The locations of these clusters corresponds to the location of the spatial edges in the signal.

Some of the characteristics of wavelets that make them ideal for signal representation are as follows:

- Wavelets are localized in both the space/time and scale/frequency domains. Hence, they can easily detect local features in a signal.
- Wavelets are based on a multi-resolution analysis. Wavelet decomposition allows us to analyze a signal at different resolution levels (scales).
- Wavelets are smooth, which can be characterized by their number of vanishing

moments. A function defined on the interval [a, b] has n vanishing moments if

$$\int_a^b f(x)x^i dx = 0 \tag{2.3}$$

for $i = 0, 1, \ldots, n-1$. The number of vanishing moments represents how well smooth signals can be approximated in a wavelet basis.

Furthermore, there exist fast and stable algorithms to calculate the discrete wavelet transform and its inverse. The computational complexity of this fast algorithm is $O(n)$.

2.3 Wavelets and multi-resolution analysis

Multi-resolution analysis forms the basis for the development of discrete wavelets and hence, it is introduced first in this section.

2.3.1 Multi-resolution analysis

Consider the vector space $\mathbf{L}^2$ of the square integrable functions in $\mathbf{R}$:

$$\mathbf{L}^2 = \left\{ f : \int_{-\infty}^{+\infty} f^2(x)dx < \infty \right\}. \tag{2.4}$$

In a multi-resolution analysis, $\mathbf{L}^2$ is decomposed in nested subspaces V_j

$$\ldots \subset V_{-2} \subset V_{-1} \subset V_0 \subset V_1 \subset V_2 \subset \ldots \tag{2.5}$$

such that

1. $\bigcap_{j=-\infty}^{+\infty} V_j = \{0\}$ and $\overline{\bigcup_{j=-\infty}^{+\infty} V_j} = \mathbf{L}^2$, where $\bar{\cdot}$ represents the closure of the set concerned

2. For any $f \in \mathbf{L}^2$ and any $j \in \mathbf{Z}$, $f(x) \in V_j$ if and only if $f(2x) \in V_{j-1}$

3. For any $f \in \mathbf{L}^2$ and any $k \in \mathbf{Z}$, $f(x) \in V_0$ if and only if $f(x-k) \in V_0$

If a function $\phi(x) \in V_0$, along with the set of its integer translates $\{\phi(x-k)\}_{k\in\mathbf{Z}}$, forms a basis for the space V_0, it is called a *scaling function* or *father function*. For the other subspaces V_j (with $j \neq 0$) we define:

$$\phi_{j,k}(x) \equiv 2^{\frac{j}{2}}\phi(2^j x - k). \tag{2.6}$$

2.3.2 Wavelet functions

The nested nature of the subspaces allows the decomposition of V_{j+1} in V_j and W_j, the orthogonal component of V_j in V_{j+1}:

$$V_j \oplus W_j = V_{j+1}, \tag{2.7}$$

$$W_j \perp V_j. \tag{2.8}$$

The direct sum of the subspaces W_j is equal to $\mathbf{L}^2$:

$$\overline{\bigcup_{j=-\infty}^{+\infty} V_j} = \overline{\bigoplus_{j=-\infty}^{+\infty} W_j} = \mathbf{L}^2. \tag{2.9}$$

Thus, V_j is a "coarse-resolution" representation of V_{j+1}, while W_j carries the "high-resolution" difference between V_j and V_{j+1}.

If any function $\psi(x) \in W_0$ obeys the translation property (Property 3, Section 2.3.1) and along with its integer translates, $\{\psi(x-k)\}_{k\in\mathbf{Z}}$, forms a basis for the space W_0, it is called a *wavelet function* or *mother function*. For the other subspaces W_j (with $j \neq 0$) we define:

$$\psi_{j,k}(x) \equiv 2^{\frac{j}{2}}\psi(2^j x - k). \tag{2.10}$$

2.3.3 The fast wavelet transform (FWT)

Because V_0 and W_0 are both subspaces of V_1, we can express $\phi(x)$ and $\psi(x)$ in terms of the basis functions of V_1:

$$\phi(x) \equiv 2\sum_k h_k \phi(2x-k), \tag{2.11}$$

$$\psi(x) \equiv 2\sum_k g_k \phi(2x-k). \tag{2.12}$$

Due to multi-resolution analysis, these relations are valid between V_{j+1}, V_j and W_j for any arbitrary j as well. In the above relations, h_k and g_k are the lowpass and high-pass filter coefficients, respectively, that define the scaling function $\phi(x)$ and the wavelet function $\psi(x)$.

We can also express a function $f(x)$ that is written in terms of the basis functions of V_{j+1} in terms of the basis functions of V_j and W_j:

$$f(x) = \sum_k \lambda_{j+1,k}\phi_{j+1,k}(x),$$

$$\Rightarrow f(x) = \sum_l \lambda_{j,l}\phi_{j,l}(x) + \sum_l \gamma_{j,l}\psi_{j,l}(x). \tag{2.13}$$

The transform coefficients, $\lambda_{j,l}$ and $\gamma_{j,l}$, are defined by:

$$\lambda_{j,l} = \sqrt{2}\sum_k h_{k-2l}\lambda_{j+1,k}, \tag{2.14}$$

$$\gamma_{j,l} = \sqrt{2}\sum_k g_{k-2l}\lambda_{j+1,k}, \tag{2.15}$$

This operation has a complexity $O(n)$ and is used to compute the discrete version of the wavelet transform (DWT) and hence, is known as the *Fast Wavelet Transform* (FWT). It is also known as the filter bank algorithm (Figure 2.2). The inverse wavelet transform can be obtained in a similar way.

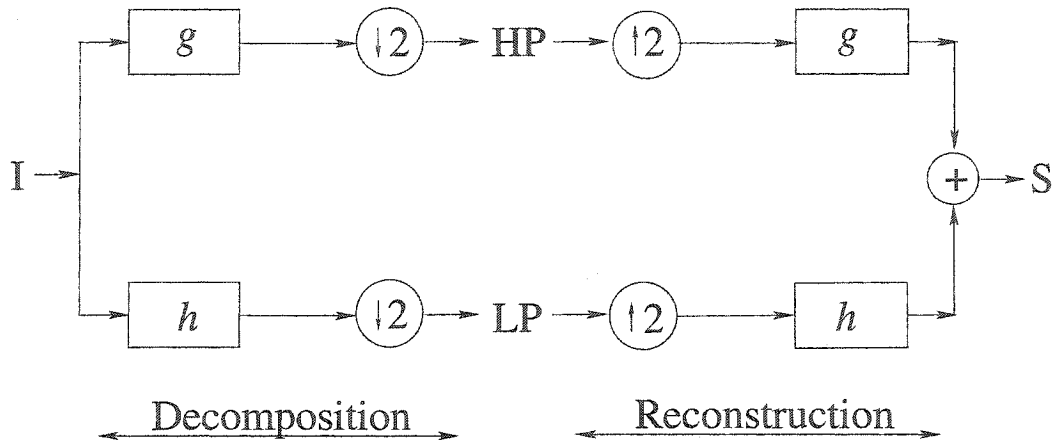

Figure 2.2: The filter bank algorithm for orthogonal wavelets: filtering and down-sampling of the signal I yields the low-pass signal LP and the high-pass signal HP. Signal S is reconstructed by up-sampling and filtering with the corresponding filters. In case of perfect reconstruction, the input and the output signals are the same

2.3.4 Orthogonal wavelets

If the $\phi_{j,k}$ and $\psi_{j,k}$ are orthonormal, i.e.,:

$$V_j \perp W_j, \tag{2.16}$$

$$\langle \phi_{j,l}, \phi_{j,l'} \rangle = \delta_{l-l'}, \tag{2.17}$$

$$\langle \psi_{j,l}, \psi_{j',l'} \rangle = \delta_{j-j'}\delta_{l-l'}, \tag{2.18}$$

then we can calculate the coefficients of the decomposition in (2.13) by taking the inner product of the function with scaling and wavelet functions:

$$\lambda_{j,l} = \langle f, \phi_{j,l} \rangle , \tag{2.19}$$

$$\gamma_{j,l} = \langle f, \psi_{j,l} \rangle . \tag{2.20}$$

Examples of orthogonal wavelets are the family of orthogonal wavelets constructed by Daubechies [19]. The scaling function and the wavelet function for the member

with 2 vanishing moments (also known as "D4" because the corresponding wavelet filter has 4 taps or filter coefficients) are shown in Figures 2.3(a) and (b), respectively. The Symmlet-8 is the least asymmetric compactly supported wavelet with 8 supporting moments and the corresponding scaling function and wavelet function are shown in Figures 2.3 (c) and (d), respectively.

2.3.5 Bi-orthogonal wavelets

To obtain some special properties otherwise not available with the orthogonality conditions, such as linear phase and symmetry, we use the bi-orthogonality conditions in which we have two multi-resolution analyses, a primal and a dual:

- Primal: $V_j,\ W_j,\ \phi_{j,k},\ \psi_{j,k}$.
- Dual : $\widetilde{V}_j,\ \widetilde{W}_j,\ \widetilde{\phi}_{j,k},\ \widetilde{\psi}_{j,k}$.

The bi-orthogonality conditions imply:

$$V_j \perp \widetilde{W}_j, \tag{2.21}$$

$$\widetilde{V}_j \perp W_j, \tag{2.22}$$

$$\left\langle \widetilde{\phi}_{j,l}, \phi_{j,l'} \right\rangle = \delta_{l-l'}, \tag{2.23}$$

$$\left\langle \widetilde{\psi}_{j,l}, \psi_{j',l'} \right\rangle = \delta_{j-j'}\delta_{l-l'}. \tag{2.24}$$

The coefficients of the decomposition in the bi-orthogonal wavelet basis are obtained by taking the inner product of the function with the *dual* scaling and wavelet functions:

$$\lambda_{j,l} = \left\langle f, \widetilde{\phi}_{j,l} \right\rangle, \tag{2.25}$$

$$\gamma_{j,l} = \left\langle f, \widetilde{\psi}_{j,l} \right\rangle. \tag{2.26}$$

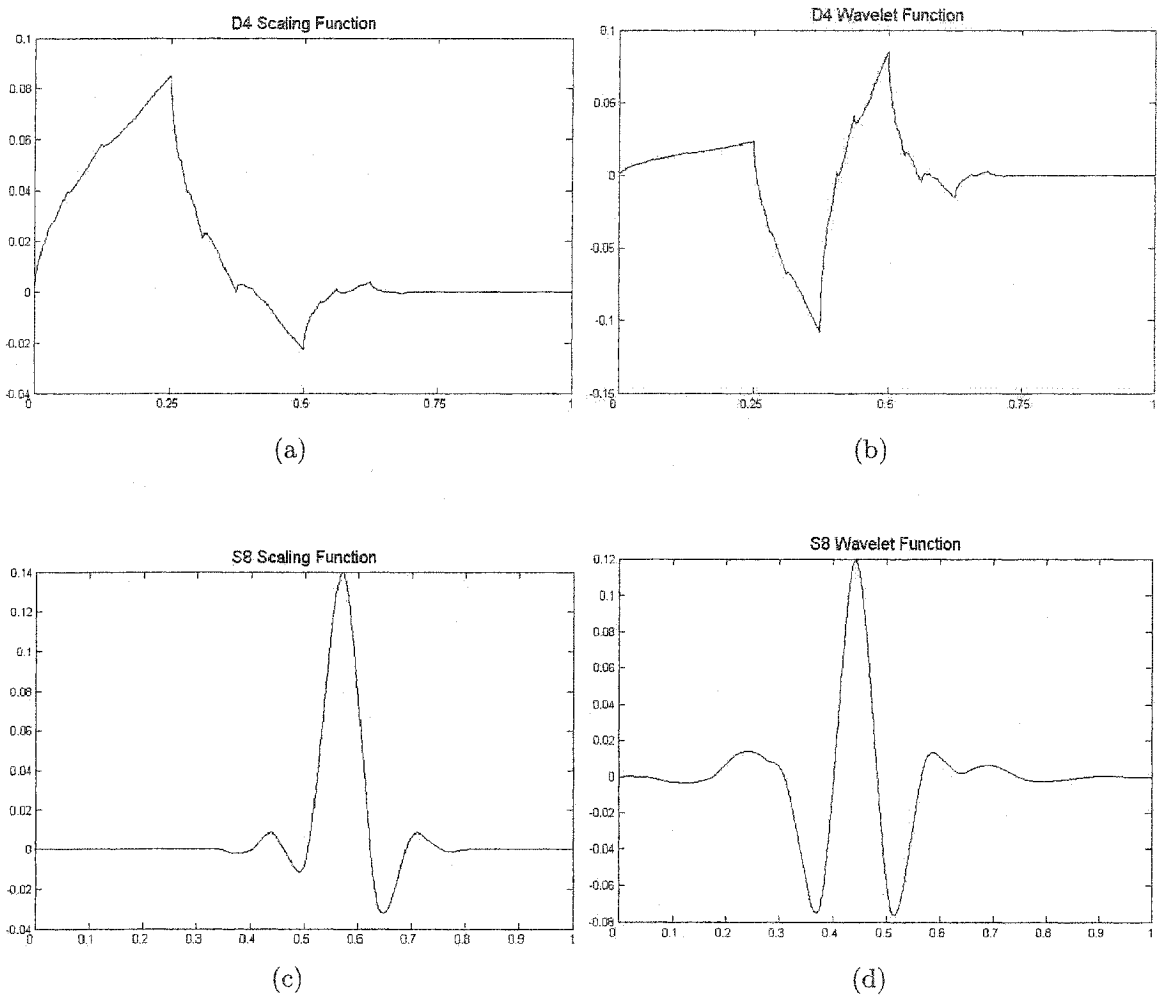

Figure 2.3: Orthogonal scaling and wavelet functions. (a) Daubechies scaling function with 4 vanishing moments, (b) Daubechies wavelet function with 4 vanishing moments, (c) Scaling function for the least asymmetric compactly supported wavelet, Symmlet, with 8 vanishing moments (Symmlet-8), and (d) Symmlet-8 wavelet function.

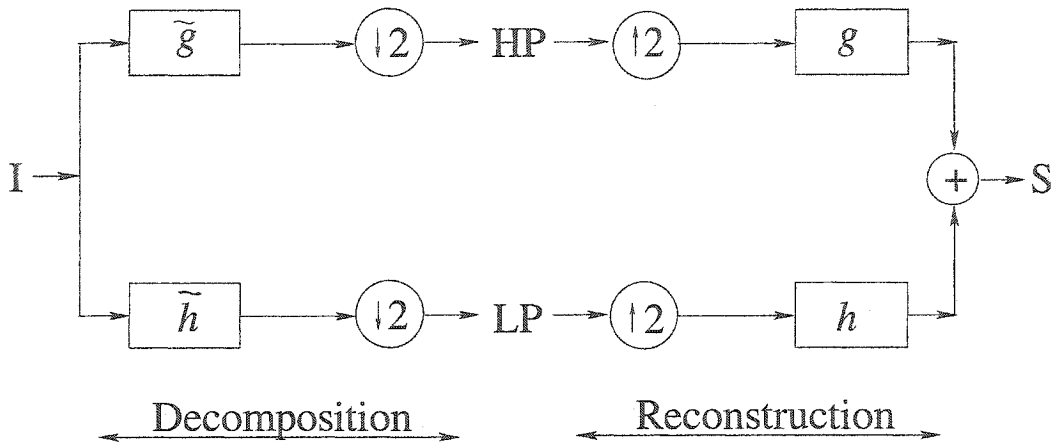

Figure 2.4: The filter bank algorithm for bi-orthogonal wavelets: filtering and down-sampling of the signal I yields the low-pass signal LP and the high-pass signal HP. Signal S is reconstructed by up-sampling and filtering with the corresponding filters. The filters used for decomposition are the dual of the ones used for reconstruction. In case of perfect reconstruction, the input and the output signals are the same

We can still use the filter bank algorithm if we use the dual filter pair $(\tilde{h},\ \tilde{g})$ (related to the dual multi-resolution analysis) for the decomposition and the primal filter pair $(h,\ g)$ (related to the primal multi-resolution analysis) for the reconstruction. Such a filter bank algorithm is depicted in Figure 2.4.

Examples of bi-orthogonal wavelets are the family of bi-orthogonal wavelets constructed by Cohen, Daubechies and Feauveau (CDF) [30]. The primal and dual scaling and wavelet functions for the bi-orthogonal 1-3 member of the CDF family is illustrated in the Figure 2.5.

2.3.6 Higher dimensions

The above wavelets were defined on a one-dimensional domain. To create wavelets for higher dimensional domains, we can perform the one-dimensional wavelet transform independently for each dimension in any order.

In the two-dimensional case we can get the square variant of the decomposition (see Figure 2.6) and the basis functions are the tensor products of the one-dimensional

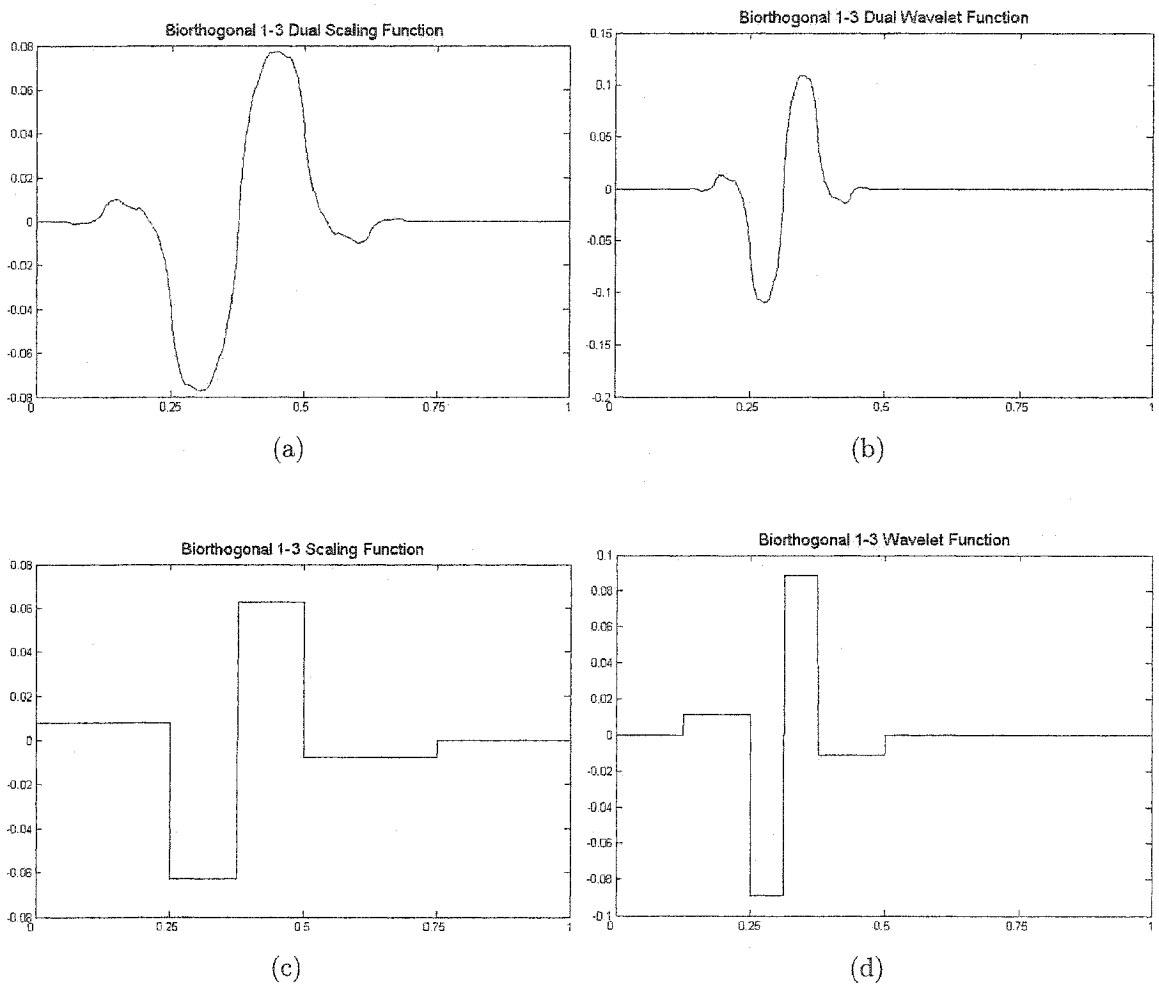

Figure 2.5: Scaling and wavelet functions for the Bi-orthogonal 1-3 case. (a) Dual scaling function, (b) Dual wavelet function, (c) Scaling function, and (d) Wavelet function.

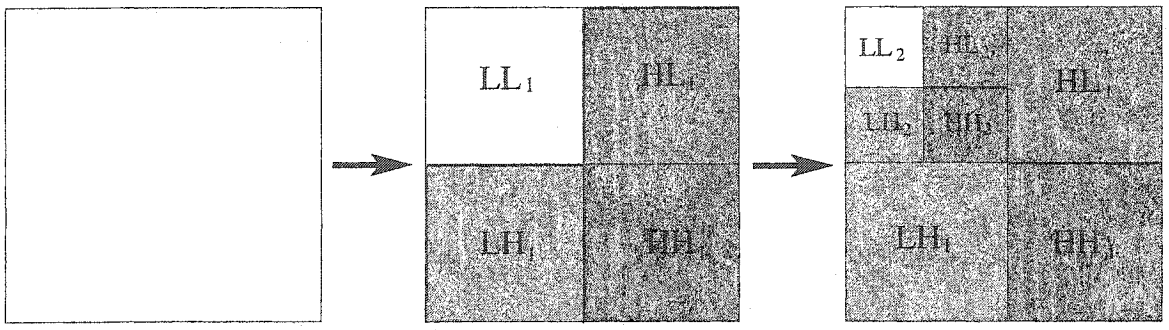

Figure 2.6: The two-dimensional wavelet transform (square variant) with two successive levels of decomposition.

basis functions. After one transform step we have:

$$\frac{\phi(x) \otimes \phi(x) | \phi(x) \otimes \psi(x)}{\psi(x) \otimes \phi(x) | \psi(x) \otimes \psi(x)} \tag{2.27}$$

The filter bank algorithm for the two-dimensional wavelet transform for one decomposition level is shown in Figure 2.7. The image is decomposed into four subbands, namely *LL*, *HL*, *LH* and *HH*, where *LL* represents the *approximation subband* containing the low-pass equivalent of the image, *HL* represents the *detail subband* containing the horizontal edge information in the image, *LH* represents detail subband containing the vertical edge information in the image, and *HH* represents the detail subband containing the diagonal edge information in the image. At each subsequent level of decomposition, the approximation subband is further decomposed into four more subbands.

2.4 The wavelet transform and translation invariance

The sub-sampling of the signal in the filter bank causes the wavelet transform to vary with translations. Only if delay or advance is a multiple of 2^n, with n the number

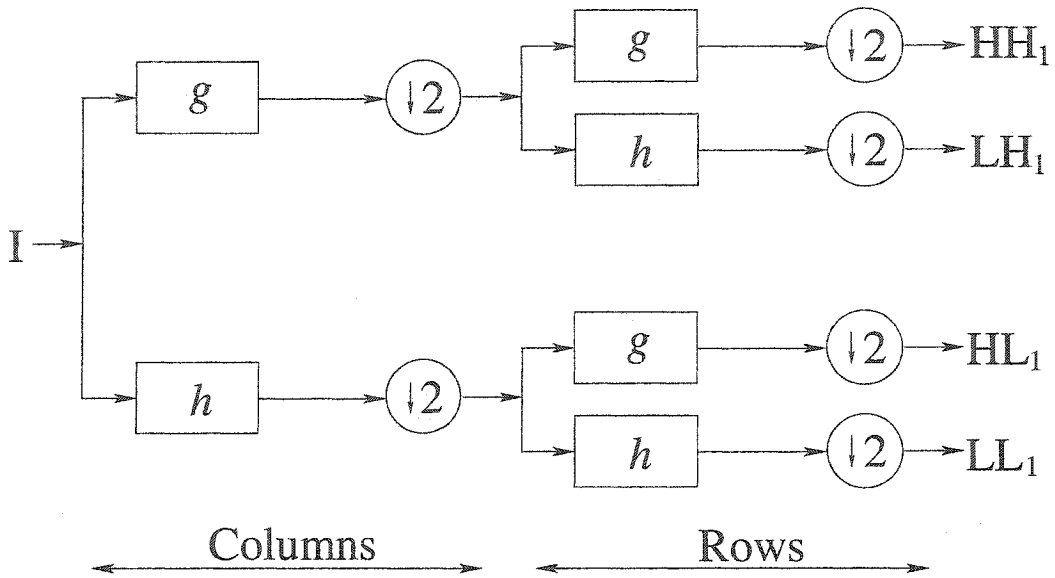

Figure 2.7: The filter bank algorithm for a two-dimensional orthogonal wavelet transform of the two-dimensional signal I (e.g., image). The one dimensional transform is first applied along the columns and then on each row. The resultant output has the same size as the input signal.

of transform levels, will the wavelet transform be a delayed or advanced version of the original transformed signal. In two dimensions, this condition needs to be true in both the vertical and horizontal directions.

The wavelet transform can be converted into an invariant transform by removing the sub-sampling step from the decomposition filter bank. This is called the *redundant wavelet transform* or *stationary*, or *non-decimated wavelet transform* [31]. At each resolution step the filters have to be up-sampled to keep a consistent multi-resolution analysis. Also, the computational complexity is increased to $O(pn)$, with $p \leq \log(n)$ the number of transform levels. For the inverse transform, a mean value of appropriate transform coefficients has to be calculated due to the redundancy in the forward transform.

Chapter 3

Image Denoising Using Wavelets

This chapter describes the application of wavelets in image denoising and introduces some of the commonly employed image denoising methods. We also describe a new method for denoising images in the wavelet domain using thresholds that are adapted using the hierarchical information corresponding to each coefficient.

3.1 Introduction

Image denoising represents a trade-off between noise suppression and preserving actual image features like edges and details. To remove noise without excessive smoothing of important details, a denoising algorithm needs to be *spatially adaptive.*

Figure 3.1 illustrates the 3-level orthogonal DWT of the test image *Lena.* The DWT of an image yields fairly well decorrelated wavelet coefficients. However, as can be seen, these coefficients are not entirely independent. The large-magnitude coefficients tend to occur near each other within subbands, and also at the same relative spatial locations in subbands at adjacent scales and orientations, as noted, e.g., in [32]. Note that the positions of the large wavelet coefficients indicate image edges, i.e., the DWT has an edge detection property. Figure 3.1 also illustrates the sparsity of the DWT of images, which makes it in particular suitable for image coding

(a) Test image - Lena (b) 3-level DWT

Figure 3.1: (a) Test image *Lena,* and (b) 3-level dyadic wavelet decomposition of the test image using Symmlet-8 orthogonal wavelet. The detail subbands have been scaled for display purposes.

and compression, and denoising.

The wavelet representation, due to its sparsity, edge detection and multi-resolution properties, naturally facilitates such spatially adaptive noise filtering. A common procedure is: (1) Compute the DWT or non-decimated wavelet transform; (2) Remove noise from the wavelet coefficients; and (3) Reconstruct the denoised image.

3.2 Input signal models and notations

3.2.1 Time domain representation

A digital image can be seen as a matrix of pixels. The row and column location of any coefficient in the matrix defines the location of the pixel in the image. We denote a discrete image as $\mathbf{x} = \{x_{ij} : i = 1, 2, \ldots, N \text{ and } j = 1, 2, \ldots, M\}$, where i and j denote the spatial position and N x M is the size of the image. The boldfaced

letters represent the matrix representations of the signals being considered.

In this thesis we consider the following additive model of a discrete image $\mathbf{x}$ and noise ε

$$\mathbf{g} = \mathbf{x} + \varepsilon. \tag{3.1}$$

The signal $\mathbf{g}$ is the received input. The noise ε is a matrix of random variables, while the unknown $\mathbf{x}$ is a deterministic signal. One might also start from a fully stochastic model, considering $\mathbf{x}$ as well to be a specific realization of a random matrix. The noise considered has zero mean and is uncorrelated, i.e.,

$$\mathrm{E}(\varepsilon) = 0, \tag{3.2}$$

$$\mathrm{E}(\varepsilon_{ij}, \varepsilon_{lk}) = \sigma_{ij}^2 \delta(i-l)\delta(j-k). \tag{3.3}$$

Such a noise matrix is called white. If all the noise coefficients follow the same distribution, they are said to be identically distributed. This implies that $\sigma_{ij}^2 = \sigma^2$ for all i and j. If Gaussian distributed noise variables are uncorrelated, they are *statistically independent.* This thesis concentrates on the case where the additive noise coefficients are independent and identically distributed (i.i.d.) and have a Gaussian distribution (additive white Gaussian noise, AWGN).

3.2.2 Wavelet domain representation

In the wavelet domain, a sparse representation leads to the compression of the most essential information in a signal into relatively few, large coefficients which correspond to areas of major spatial activity (edges, corners, peaks) in the image. On the other hand, corrupting noise is spread over all the coefficients.

Let $\mathbf{W}$ and $\mathbf{W}^{-1}$ be the two dimensional orthogonal or bi-orthogonal discrete wavelet transform (DWT) matrix and its inverse, respectively. Due to linearity of the

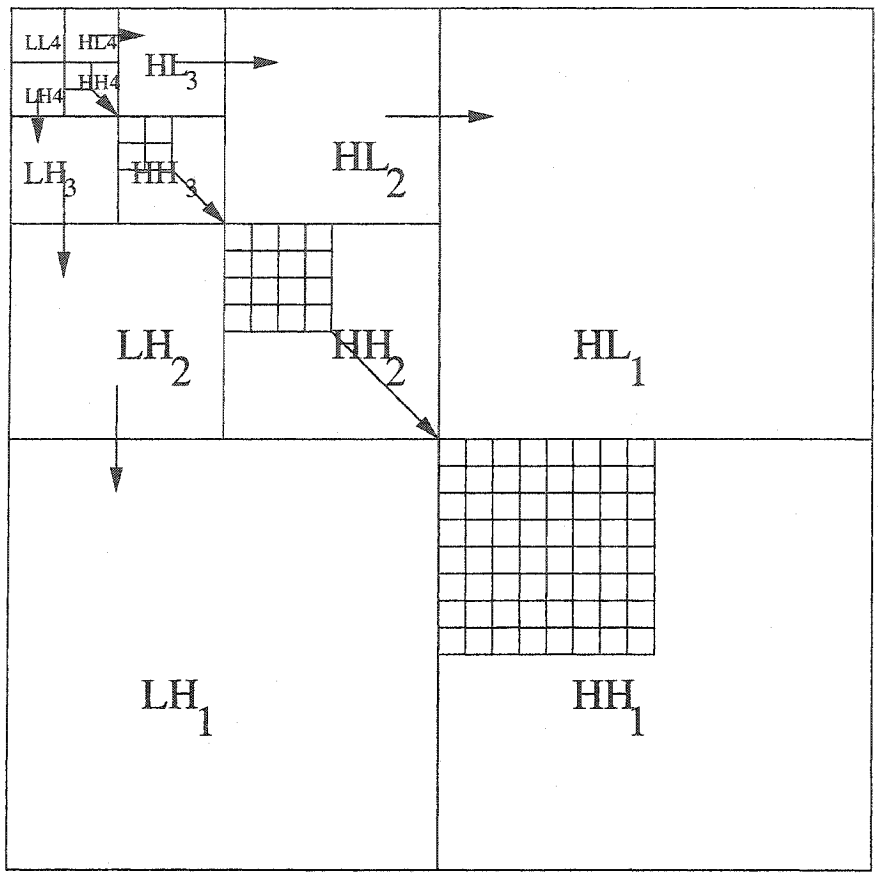

Figure 3.2: The subband structure for a 4-level DWT decomposition and the parent-child relationship among the wavelet coefficients in successive subbands.

wavelet transform, the additive model (3.1) remains additive in the wavelet domain also:

$$\mathbf{Y} = \mathbf{X} + \mathbf{N} \tag{3.4}$$

where, $\mathbf{Y} = \mathbf{W}\mathbf{g}$ represents the matrix of wavelet coefficients of the observed image signal. Similarly, $\mathbf{X} = \mathbf{W}\mathbf{x}$ and $\mathbf{N} = \mathbf{W}\varepsilon$ represent the matrix of wavelet coefficients of the original noise-free image and the additive noise, respectively. The *detail* subbands are HH_k, HL_k and LH_k, where k is the scale varying from $1, 2, \ldots J$, and J is the total number of decompositions. The size of the subband at scale k is $\frac{N}{2^k} \mathrm{x} \frac{M}{2^k}$. The subband LL_J is the low-resolution residue. Figure 3.2 shows the subband representation for a 4-level dyadic representation of an image.

An orthogonal wavelet transform maps the additive white Gaussian noise, with a variance σ^2, in the input image to an additive Gaussian noise, with a variance σ^2, in the wavelet domain. The case with bi-orthogonal wavelet transform is more complicated, but the variance of the transform coefficients of the noise is constant for each subband and can be estimated easily [33].

3.3 Noise variance estimation

If the noise variance σ^2 is not known in an application, then it has to be estimated from the input data. In the wavelet domain, the highest frequency subband of the decomposition is commonly used for this estimation. In the DWT of an image, the HH_1 subband contains mostly noise and only a few significant wavelet coefficients corresponding to the high frequency information in the original image. The median method is used to get a robust estimate of noise. The median causes the estimate to be insensitive to the isolated high amplitude coefficients reflecting high frequency information. In [14], it was proposed

$$\hat{\sigma} = \frac{\text{Median}\left[|\{Y_{ij} : i, j \in HH_1\}|\right]}{0.6745} \tag{3.5}$$

This expression above results from the relationship between the median and standard deviation of the random variables generated using the absolute value of the normally distributed random variables. The estimate in (3.5) is commonly used in image denoising [11, 34] and we use it in this thesis as well.

3.4 State-of-the-art overview of wavelet domain denoising

The wavelet transform, owing to its sparsity, edge detection and multi-resolution properties, naturally facilitates edge preserving noise suppression in images. But as is the case with noise suppression in the time domain, one question needs to be answered in the wavelet domain as well: *How to separate noise from the original image signal?*

Over the years, several different approaches have appeared in the literature as an answer to the above question. Some of these methods are unique to the wavelet domain, while others are adaptations of noise removal methods in time domain, where the adaptations have been done keeping in mind the special characteristics of the wavelet transform.

3.4.1 Image denoising using wavelet thresholding

Wavelet thresholding is one such approach that was conceived for the specific purpose of denoising in the wavelet domain. Its popularity stems from its simplicity, where the basic idea is that each coefficient in the orthogonal wavelet domain is *thresholded* by comparing against a threshold. Thresholding implies that a coefficient is set to zero if it is smaller than the threshold, otherwise, it is either kept or modified. While one of the first reports about this approach was by Weaver *et al.* [35], Donoho and Johnstone [36]-[14] are credited with the development of a systematic theory. They have shown that the various thresholding schemes for denoising are asymptotically optimal in the minimax mean square error (MSE) sense.

Two classical thresholding policies are *hard-thresholding* [13] and *soft-thresholding* [37], where each wavelet coefficient is multiplied by a given *shrinkage factor*, which is a function of the magnitude of the coefficient. In both the cases, this multiplication

with the shrinkage factor sets the coefficients that are below a certain threshold to zero. In hard-thresholding, the remaining coefficients are left unchanged, while in soft-thresholding, the magnitudes of the coefficients above the threshold are reduced by an amount equal to the threshold value. Owing to the discontinuous nature of the hard-thresholding scheme, it yields abrupt artifacts in the reconstructed images and thus, in image processing applications soft-thresholding is often preferred over the hard one (e.g., [11]). Various other thresholding policies, such as the "non-negative garrote" function [38] and the "hyperbola" function [25], have been proposed as compromises between the classical hard and soft thresholding policies. We provide a more detailed discussion on the thresholding techniques in Section 3.5.1.

For the wavelet thresholding to be effective, the choice of the threshold is of primary importance, and a number of publications have been devoted to it. Most of the methods for estimating the threshold assume that the noise corrupting the original noise-free image is additive white Gaussian noise (AWGN). One of the earliest well known threshold estimation methods is the *universal threshold* of Donoho and Johnstone [13]. This threshold aims at the removal of all the noisy coefficients that are smaller than the expected maximum of the the additive Gaussian noise in the wavelet domain. At different resolution scales in the wavelet domain, the threshold differs only in a constant factor that is dependent upon the number of coefficients in a given subband.

Subsequent to the work of [13] more sophisticated thresholds that are adaptively estimated for each level have been proposed. Donoho and Johnstone [14] proposed the subband adaptive *SURE* threshold, which was derived by minimizing the Stein's unbiased risk estimate [39] while using soft-thresholding. Nason [40] developed a *cross-validation* method for selecting a wavelet regression threshold that produced good estimates with respect to the mean square error. Jansen *et al.* [41] and Weyrich and Warhola [42] have used *generalized* cross-validation in a noise reduction algorithm

based on wavelet thresholding to estimate the optimal threshold without the knowledge of noise variance and have also applied it to correlated noise. The threshold estimation methods proposed in [43, 11] derive the optimum threshold by minimizing the mean squared error in a thresholded signal. An *a priori* distribution of the noise-free wavelet coefficients is assumed in these methods. While Ruggeri and Vidakovic [43] estimate the optimal threshold for using hard thresholding to suppress noise in the signal, Chang *et al.* [11] have proposed a nearly optimal threshold for noise removal using soft-thresholding. Hilton [44], taking into account the clustering properties of the wavelet coefficients, suggested a *data analytic* threshold. However, all of the above threshold estimation techniques yield a constant value for each detail subband, and thus are *spatially uniform.* A better option would be to decide for each coefficient separately whether to keep it or set it to zero using a *spatially varying* threshold. One such spatially adaptive threshold with *context-modeling* of wavelet coefficients was proposed by Chang *et al.* [45, 46].

3.4.2 Image denoising using multi-scale products

Approaches other than wavelet thresholding have also been proposed. In the real-world signals and images, the transitions are less abrupt than those produced by the noise. The actual edges in a signal or image produces large wavelet coefficients across many scales, i.e., they are *persistent* across scales; noise, on the other hand, dies out quickly as the scale increases. This persistent change in the wavelet transform coefficients through different scales can also be used as a criterion for selecting "important" or "significant" coefficients from which a denoised image is to be reconstructed.

In parallel with Donoho and Johnstone's work, Mallat and Zhong [47] were the first to introduce the complete multi-scale edge representation of signals using quadratic spline wavelets. They showed the detection and characterization of the multi-scale edges using the local maxima of the wavelet transform. Xu *et al.* [48] adapted this

idea in this basic and simple algorithm for removing additive white Gaussian noise (AWGN) from signals. They proposed using the correlation of the wavelet coefficients across adjacent scales to distinguish significant edges from noise, and called it *spatially selective noise filtration.* Pan *et al.* [49] examined the behavior of the AWGN in [48] and proposed a noise level estimation technique. While Xu *et al.* [48] use *inter-scale products* of the wavelet coefficients at adjacent scales in order to detect the edge coefficients, the selection of these significant coefficients has been based on the *inter-scale ratios* in [50]. A method similar to [48] was used by Sadler and Swami [51] and some theoretical justification was provided. They named their technique *multi-scale product method* (MPM). Ge and Mirchandani [52] have studied the relationship between the MPM approach and Donoho and Johnstone's hard-thresholding rule. They have further extended the MPM to a soft-thresholding-like method and have suggested a technique to extract the weak features while avoiding the extraction of noise for image reconstruction.

3.4.3 Bayesian methods for image denoising

To improve upon the ad-hoc nature of the thresholding policies, various Bayesian approaches to wavelet shrinkage have been developed, which are less ad-hoc and have been shown to be effective [53, 54, 55]. The shrinkers developed using the Bayesian rules inherently have the desirable property that they can heavily shrink the small coefficients and only slightly shrink the large coefficients.

For the development of the Bayesian shrinkage rules, it is necessary to assume an *a priori* distribution of the noise-free image wavelet coefficients. The histograms of the wavelet coefficients are sharply peaked at zero with heavy tails. Mallat [56] modeled the prior distribution of the image wavelet coefficients as a generalized Laplacian distribution (also known as the generalized Gaussian distribution (GGD)). This model is often used in image processing literature, e.g., [57, 11, 46, 58, 59, 60]. The image

wavelet coefficients are also modeled using a *Gaussian mixture*, where the mixture parameter can be a constant for each subband [61], or can be estimated for each subband coefficient [62, 63, 64]. *Gaussian scale mixture* (GSM) models have also been used in several methods, e.g., [65, 66, 67], where each coefficient is modeled as a product of two random variables. The spatial interactions among wavelet coefficients have also been modeled using the Markov Random Field (MRF) prior models for spatial clustering [68].

The Bayesian wavelet domain filtering techniques, that assume the wavelet coefficients as mutually independent, result in a simple shrinking of the noisy coefficients that is less ad-hoc than the classical thresholding, and also outperform the hard- and soft-thresholding rules in terms of the MSE [61, 53]. Moulin *et al.* [58] have developed a denoising scheme based on the maximum a posteriori estimates of the noise-free image subband coefficients. Under the minimum mean squared error (MMSE) criterion, the optimum estimate of the noise-free wavelet coefficients have been studied by Simoncelli and Adelson [59]. In this, they have assumed a GGD prior for the image coefficients. Another class of Bayesian shrinkers are derived from modeling the noisy wavelet coefficient themselves. Chipman *et al.* [61] have modeled these as mixtures of Gaussians and derived the MMSE estimates of the noise-free coefficients. Locally-adaptive wavelet domain Wiener filtering schemes are developed in [69, 65, 66, 67]. These result from the MMSE criterion when local GSM models are used as priors for the noisy wavelet coefficients. A locally adaptive Bayesian shrinking scheme based on the identification of the "signal of interest" has been developed in [70].

3.5 Denoising by wavelet thresholding

Wavelet thresholding is a popular and simple approach for denoising, and an overview of the current state-of-the-art was provided in the Section 3.4.1. For denoising images

in the wavelet domain using the thresholding of coefficients, two decisions need to be made. Firstly, the thresholding policy needs to be decided using which the coefficients would be thresholded. Secondly, an estimate of the threshold itself is needed in order to apply the thresholding policy.

In this section, we first describe the different kinds of thresholding rules and then discuss two of the most popular ways to estimate the threshold that is to be used by the thresholding rules.

3.5.1 Hard and soft thresholding

Two of the most popular thresholding rules are: hard-thresholding, (keep or kill), and soft-thresholding, (shrink or kill). The two thresholding schemes can be represented diagrammatically as in Figure 3.3. In both cases, coefficients below the threshold are set to zero. In hard-thresholding (Fig. 3.3(a)), the remaining coefficients are left unchanged. For an estimated threshold value T, hard-thresholding of a coefficient x can be presented as

$$T^{hard}(x) = \begin{cases} 0, \text{ if } |x| \leq T \\ x, \text{ if } |x| > T \end{cases} \tag{3.6}$$

In soft-thresholding (Fig. 3.3(b)), the magnitudes of the coefficients above the threshold are reduced by an amount equal to the threshold. For an estimated threshold T, the soft-thresholding of a coefficient x can be written as

$$T^{soft}(x) = \begin{cases} 0, & \text{if } |x| \leq T \\ \text{sign}(x)\left(|x| - T\right), & \text{if } |x| > T \end{cases} \tag{3.7}$$

In soft-thresholding, the estimates are biased: large coefficients are always reduced in magnitude; therefore, the mathematical expectations of their estimates differ from the observed values. The reconstructed image is often over-smoothed. On the other side, a disadvantage of hard-thresholding is its abrupt discontinuity: estimates have a

larger variance and may be highly sensitive to small changes in the data. In practice, especially when the noise level is high, hard-thresholding yields abrupt artifacts in the reconstructed image. Due to this, in image processing applications soft-thresholding is usually preferred to hard-thresholding.

A compromise between the classical hard- and soft-thresholding rules was proposed in [25] in the form of a hyperbola function. The thresholding rule can be expressed as:

$$T^{hyperbola}(x) = \begin{cases} 0, & \text{if } |x| \leq T \\ \text{sign}(x)\sqrt{x^2 - T^2}, & \text{if } |x| > T \end{cases} \tag{3.8}$$

Eq. (3.8) attenuates the large coefficients less as compared to the soft-thresholding rule and is continuous.

In this thesis, keeping in view the advantages, simplicity, and popularity, we use the soft-thresholding scheme in our algorithms.

3.5.2 Threshold selection

In wavelet thresholding, a considerable amount of literature has been devoted to the choice of the threshold. An appropriately chosen threshold parameter is necessary in order to remove the noise from the corrupted wavelet coefficients. If the threshold is too large, then the features in the reconstructed image would appear blurred or over-smoothed due to excessive loss of information. On the other hand, if the threshold is too small, then not enough noise is removed from the wavelet coefficients, and the reconstructed image is still noisy.

In this thesis, we concentrate on two of the more popular methods to estimate the threshold parameter: *SureShrink* and *BayesShrink*.

- ***SureShrink***

  For one-dimensional data, Donoho and Johnstone proposed a threshold [14] derived by minimizing the Steins unbiased risk estimate (SURE) [39]. The

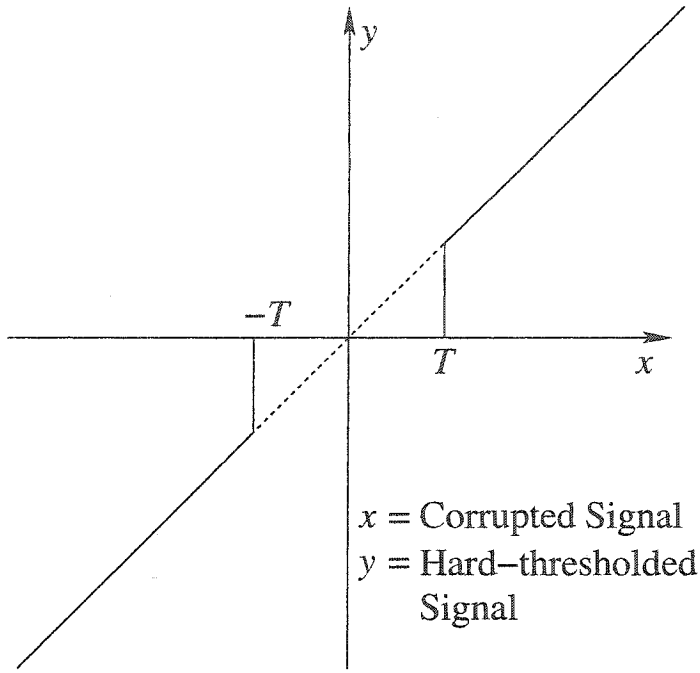

(a) Hard-threshold

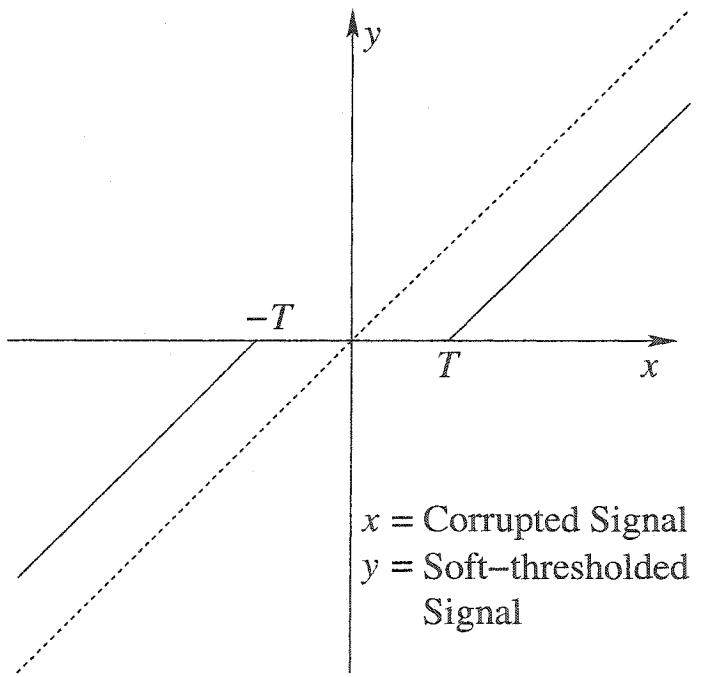

(b) Soft-threshold

Figure 3.3: (a) Hard-thresholding of a noisy signal, and (b) Soft-thresholding of a noisy signal

threshold depends upon the shrinkage function used and can be generalized to images. For the *detail* subband s, the threshold, T_s^S, to be used with the soft-thresholding function, is chosen as the value that minimizes the Steins unbiased estimate of the risk, $SURE^S(T, \mathbf{Y})$,

$$T_s^S = \arg\min_{T \geq 0} SURE^S(T, \mathbf{Y}), \tag{3.9}$$

where $\mathbf{Y}$ denotes the detail coefficients from the subband s, and

$$SURE^S(T, \mathbf{Y}) = N_s + \sum_{i=1,j=1}^{i=K,j=L} \left[\min\left(|Y_{ij}|, T\right)\right]^2 - 2\left[(\text{number of } Y_{ij}) : Y_{ij} \leq T\right], \tag{3.10}$$

Here, N_s is the number of coefficients Y_{ij} in $\mathbf{Y}$, and K and L represent the size of the subband s in terms of the number of rows and columns, respectively. The threshold above assumes $\sigma = 1$. For images with AWGN having $\sigma \neq 1$, the coefficients are normalized by an estimate of the noise standard deviation before calculating the threshold with (3.10). The estimation of the standard deviation of the corrupting noise is explained in Section 3.3.

It was shown in [14] that, in the case where the wavelet coefficient decomposition is sparse, a hybrid method combining the *universal* and the *SURE* thresholds is preferable over *SURE*. For a transformed image having N x M coefficients that have been normalized to have a unit variance, the universal threshold is given by

$$T = \sqrt{2\log(KL)} \tag{3.11}$$

This hybrid method, when combined with the soft-thresholding function, is referred to as *SureShrink* in the literature [14]. If

$$\frac{1}{N_s} \sum_{i=1,j=1}^{i=K,j=L} \left[\left(\frac{Y_{ij}}{\hat{\sigma}}\right)^2 - 1\right] \leq \frac{(\log_2 KL)^{\frac{3}{2}}}{\sqrt{KL}} \tag{3.12}$$

then *SureShrink* uses the *universal* threshold, otherwise *SURE* threshold is used for the coefficients in the subband s.

- ***BayesShrink***

  Chang *et al.* [11] use a Bayesian mathematical framework for images to derive a subband dependent threshold that is nearly optimal for soft-thresholding. The rule is called *BayesShrink*.

  The subband coefficients of an original noise-free natural image can be modeled using a GGD prior. The distribution of the noise-free subband coefficients, $p_y(y)$, can be expressed as:

$$p_y(y) = \frac{\nu}{2s\Gamma(\frac{1}{\nu})} \exp\left(-\left|\frac{y}{s}\right|^{\nu}\right), \quad s, \nu > 0 \tag{3.13}$$

  where $\Gamma(x) = \int_0^\infty t^{x-1}e^{-t}dt$ is the Gamma function. Under this prior assumption, the nearly optimal threshold, assuming soft-thresholding can be expressed as:

$$T_B = \frac{\hat{\sigma}^2}{\hat{\sigma}_X} \tag{3.14}$$

  where $\hat{\sigma}^2$ is the estimated noise variance, and $\hat{\sigma}_X$ is the estimated signal standard deviation in the considered subband. The noise variance is estimated by using (3.5). The estimate of the signal standard deviation is

$$\hat{\sigma}_X = \sqrt{\max\left(\hat{\sigma}_Y^2 - \hat{\sigma}^2, 0\right)} \tag{3.15}$$

  where

$$\hat{\sigma}_Y^2 = \frac{1}{N_s} \sum_{i=1,j=1}^{i=K,j=L} Y_{ij}^2 \tag{3.16}$$

  is the estimate of the variance of the observations, with $N_s \gg 1$ being the number of transform coefficients Y_{ij} in the subband under consideration. In

case $\hat{\sigma}^2 > \hat{\sigma}_Y^2$, all coefficients from the subband are set to zero.

The normalized threshold, $\frac{T_B}{\hat{\sigma}}$, is inversely proportional to $\hat{\sigma}_X$, the standard deviation of the noise-free coefficients in the subband considered, and inversely proportional to $\hat{\sigma}$, the standard deviation of the noise. When $\frac{\hat{\sigma}}{\hat{\sigma}_X} \ll 1$, the signal is much stronger than the noise, $\frac{T_B}{\hat{\sigma}}$ is chosen to be small so as to preserve most of the signal and remove some of the noise. On the other hand, when $\frac{\hat{\sigma}}{\hat{\sigma}_X} \gg 1$, the noise dominates the signal, $\frac{T_B}{\hat{\sigma}}$ is chosen to be large so as to aggressively remove most of the noise from the signal.

3.6 Hierarchical adaptation of thresholds

The parent-child relationship between the different subband coefficients has been exploited successfully for a long time for compression (e.g. [71]). For subbands LH_k, HL_k and HH_k, with scale $k < J-1$, the parent subbands are defined as LH_{k+1}, HL_{k+1} and HH_{k+1}, respectively (see also Fig. 3.2). Similarly, for the subbands LH_k, HL_k and HH_k, with scale $2 < k < J$, the children subbands are defined as LH_{k-1}, HL_{k-1} and HH_{k-1}, respectively. For the approximation subband LL_J, the children subbands are defined as HH_{J-1}, HL_{J-1} and LH_{J-1}. For a subband coefficient, Y_{ij}, at the position (i,j) in a subband, the parent coefficient, P_{ij}, is the $(\lceil \frac{i}{2} \rceil, \lceil \frac{j}{2} \rceil)$ coefficient in the parent subband, where $\lceil . \rceil$ maps the input value to the nearest lower integer.

Since the coefficient values in subsequent subbands are correlated, a coefficient having a relatively higher value in a parent subband, which usually represents an edge or high frequency information, gives a fair indication that the corresponding children coefficients would more probably have relatively higher values than not. A zero in a parent subband indicates a zero or low value in the children coefficients. Using this philosophy, we scale the threshold calculated for the entire subband using the individual parent coefficients, thus yielding an adaptive threshold acting individually

on each subband coefficient. We do the computations for all the HL subbands in decreasing order of scales, followed by LH and HH subbands. Since a parent subband is denoised earlier than the progeny, we use the denoised parent coefficients to get an accurate estimate of the corresponding coefficient values for the actual image. We define the hierarchically adapted threshold, HAT_{ij} for each subband coefficient as

$$HAT_{ij} = \frac{T}{\left(\alpha + \beta \frac{|P_{ij}|}{\max_{i,j}(|P_{ij}|)}\right)} \tag{3.17}$$

where, T is the threshold calculated using *BayesShrink* or *SureShrink*, and P_{ij} are the soft-thresholded parent coefficients. The variable in the denominator, $\alpha > 0$, has been added to avoid the singularity that occurs when the thresholded parent coefficient is zero. The variable $\beta > 0$ is used to vary the contribution of the parent coefficient in the final scaling of the subband optimal threshold. The parameters α and β are experimentally determined and their estimation would be discussed in Section 3.9.

In case the relative value of the parent coefficient is low (e.g., zero), the threshold value is made higher to threshold the current subband coefficient more strongly as the value of the original coefficient would most likely be low and the rest of the contribution to this coefficient is due to white noise. In case of a high relative value of a parent coefficient, the threshold is lowered so as to retain more of the current coefficient.

3.7 Image denoising algorithm

This section describes the image denoising algorithm, which achieves near optimal soft thresholding in the wavelet domain for recovering the original signal from the noisy one. The algorithm is very simple to implement and computationally efficient. The steps to denoise the corrupted image using the hierarchically adapted threshold are described in Algorithm 1 (also see Fig. 3.4).

Algorithm 1 Image denoising using hierarchically adapted threshold

STEP I	Perform multi-scale decomposition [56] of the image corrupted by Gaussian noise using wavelet transform.
STEP II	Estimate the threshold for each subband (except the lowpass residual) [11, 14].
STEP III	For each subband coefficient, calculate the hierarchically adapted threshold using (3.17).
STEP IV	Apply soft thresholding to the subband coefficients using (3.7).
STEP V	Invert the multi-scale decomposition to reconstruct the denoised image .

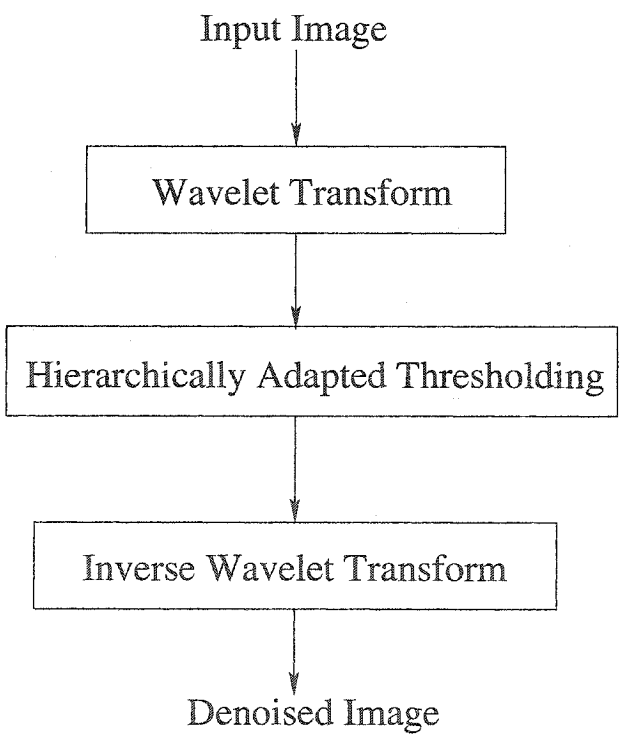

Figure 3.4: Block diagram for image denoising in the wavelet domain using hierarchically adapted thresholding

3.8 Performance evaluation in image denoising

The objective of image denoising is to produce an estimate, $\hat{\mathbf{x}}$, of the unknown noise-free image, $\mathbf{x}$, which approximates it best under a given evaluation criteria. A common criteria is the minimization of the *mean squared error* (MSE) of the result as compared to the original image

$$\text{MSE} = \frac{1}{NM} \|\mathbf{x} - \hat{\mathbf{x}}\|^2 = \frac{1}{NM} \sum_{i=1,j=1}^{i=N,j=M} (x_{ij} - \hat{x}_{ij})^2 . \tag{3.18}$$

The *signal to noise ratio* (SNR) can be expressed in terms of the MSE as

$$\text{SNR} = 10 \log_{10} \frac{\|\mathbf{x}\|^2}{\|\mathbf{x} - \hat{\mathbf{x}}\|^2} = 10 \log_{10} \frac{\|\mathbf{x}\|^2}{NM.\text{MSE}} \tag{3.19}$$

where SNR is in dB. In image processing, another common performance measure is the *peak signal to noise ratio* (PSNR), which, for 0-255 level gray-scaled images, is defined as

$$\text{PSNR} = 10 \log_{10} \frac{255^2}{NM.\text{MSE}} \text{ dB} \tag{3.20}$$

As such, the objective measures defined above do not reflect the *human perception* or the *visual quality* of the images. Thus, a more subjective measure, as visual inspection of the resulting images, is also required along with the objectives measures like MSE, SNR and PSNR.

3.9 Experimental results and discussions

Experiments are conducted on ten different natural gray scale test images of varying sizes. Test images *Airplane*, *House*, *Peppers* and *Cameraman* are of size 256 x 256 pixels. The test images *Lena*, *Barbara*, *Boat*, *Mandrill* and *Goldhill* are of size 512 x 512 pixels, while test image *Monarch* is of size 512 x 768 pixels. Ten dif-

	σ									
Lena	5	10	15	20	25	30	35	40	45	50
Initial PSNR	34.15	28.14	24.62	22.14	20.24	18.71	17.44	16.36	15.43	14.62
BayesShrink	36.82	33.40	31.48	30.19	29.22	28.47	27.85	27.3	26.81	26.34
HA *BayesShrink*	**37.16**	**33.81**	**31.92**	**30.78**	**29.77**	**28.96**	**28.25**	**27.72**	**27.15**	**26.76**
SureShrink	36.71	33.43	31.31	30.06	29.03	28.39	27.83	26.91	26.33	25.79
HA *SureShrink*	**36.98**	**33.85**	**31.83**	**30.56**	**29.35**	**28.82**	**28.16**	**27.34**	**26.78**	**26.05**

Table 3.1: PSNR results for denoising experiments with *Lena* image corrupted with different noise powers.

	σ									
Barbara	5	10	15	20	25	30	35	40	45	50
Initial PSNR	34.15	28.14	24.62	22.14	20.24	18.71	17.44	16.36	15.43	14.62
BayesShrink	35.81	31.06	28.76	27.36	26.27	25.37	24.63	24.01	23.49	23.04
HA *BayesShrink*	**35.98**	**31.37**	**29.01**	**27.72**	**26.58**	**25.69**	**24.96**	**24.38**	**23.82**	**23.4**
SureShrink	35.48	30.66	28.79	27.37	26.25	25.25	24.33	23.86	23.23	22.46
HA *SureShrink*	**35.72**	**30.98**	**29.02**	**27.75**	**26.55**	**25.54**	**24.68**	**24.15**	**23.52**	**22.68**

Table 3.2: PSNR results for denoising experiments with *Barbara* image corrupted with different noise powers.

ferent levels of additive white Gaussian corrupting noise with standard deviations, $\sigma = 5, 10, 15, 20, 25, 30, 35, 40, 45$ and 50 have been used to corrupt the test images before the application of the denoising algorithm. The wavelet transform employs Symmlet-8 filters at four scales of decomposition. Denoising has been achieved by soft thresholding the detail wavelet coefficients.

To assess the performance of the proposed scheme, *BayesShrink* and *SureShrink*

	σ									
Boat	5	10	15	20	25	30	35	40	45	50
Initial PSNR	34.15	28.14	24.62	22.14	20.24	18.71	17.44	16.36	15.43	14.62
BayesShrink	35.03	31.94	29.96	28.58	27.54	26.71	26.04	25.47	24.97	24.52
HA *BayesShrink*	**35.31**	**32.42**	**30.32**	**28.93**	**27.87**	**27.10**	**26.41**	**25.84**	**25.42**	**24.86**
SureShrink	34.55	31.90	29.86	28.57	27.57	26.54	25.75	25.16	24.76	24.39
HA *SureShrink*	**34.81**	**32.31**	**30.24**	**28.95**	**27.92**	**26.89**	**26.12**	**25.46**	**25.08**	**24.68**

Table 3.3: PSNR results for denoising experiments with *Boat* image corrupted with different noise powers.

	σ									
Mandrill	5	10	15	20	25	30	35	40	45	50
Initial PSNR	34.15	28.14	24.62	22.14	20.24	18.71	17.44	16.36	15.43	14.62
BayesShrink	35.49	31.24	29.04	27.56	26.43	25.52	24.76	24.09	23.51	22.98
HA *BayesShrink*	**35.81**	**31.66**	**29.48**	**28.12**	**26.97**	**25.92**	**25.13**	**24.46**	**23.91**	**23.34**
SureShrink	35.50	31.27	28.96	27.51	26.43	25.46	24.74	24.09	23.49	22.99
HA *SureShrink*	**35.79**	**31.63**	**29.34**	**27.98**	**26.92**	**25.86**	**25.03**	**24.43**	**23.85**	**23.3**

Table 3.4: PSNR results for denoising experiments with *Mandrill* image corrupted with different noise powers.

	σ									
Goldhill	5	10	15	20	25	30	35	40	45	50
Initial PSNR	34.15	28.14	24.62	22.14	20.24	18.71	17.44	16.36	15.43	14.62
BayesShrink	35.67	31.9	29.84	28.56	27.68	27.05	26.51	26.03	25.6	25.19
HA *BayesShrink*	**35.98**	**32.34**	**30.35**	**29.21**	**28.23**	**27.52**	**26.97**	**26.45**	**25.91**	**25.50**
SureShrink	35.37	31.86	29.85	28.31	27.64	26.95	26.27	25.61	25.32	25.01
HA *SureShrink*	**35.69**	**32.3**	**30.38**	**28.72**	**27.98**	**27.45**	**26.74**	**26.21**	**25.72**	**25.43**

Table 3.5: PSNR results for denoising experiments with *Goldhill* image corrupted with different noise powers.

	σ									
Airplane	5	10	15	20	25	30	35	40	45	50
Initial PSNR	34.15	28.14	24.62	22.14	20.24	18.71	17.44	16.36	15.43	14.62
BayesShrink	37.46	33.55	31.54	30.31	29.45	28.69	27.91	27.12	26.31	25.55
HA *BayesShrink*	**37.79**	**34.09**	**32.02**	**30.75**	**29.91**	**29.03**	**28.31**	**27.50**	**26.68**	**25.93**
SureShrink	38.74	34.7	32.10	30.85	29.65	27.64	25.97	25.46	24.99	24.50
HA *SureShrink*	**38.98**	**34.92**	**32.42**	**31.13**	**29.98**	**28.03**	**26.45**	**25.94**	**25.42**	**24.89**

Table 3.6: PSNR results for denoising experiments with *Airplane* image corrupted with different noise powers.

	σ									
House	5	10	15	20	25	30	35	40	45	50
Initial PSNR	34.15	28.14	24.62	22.14	20.24	18.71	17.44	16.36	15.43	14.62
BayesShrink	36.88	32.86	30.76	29.35	28.37	27.60	26.97	26.42	25.91	25.45
HA *BayesShrink*	**37.12**	**33.17**	**31.14**	**29.92**	**28.93**	**28.14**	**27.56**	**26.91**	**26.47**	**25.96**
SureShrink	36.94	32.42	30.66	29.14	28.33	27.33	26.12	25.77	25.43	25.10
HA *SureShrink*	**37.18**	**32.85**	**31.12**	**29.63**	**28.91**	**27.89**	**26.67**	**26.14**	**25.96**	**25.54**

Table 3.7: PSNR results for denoising experiments with *House* image corrupted with different noise powers.

	σ									
Peppers	5	10	15	20	25	30	35	40	45	50
Initial PSNR	34.15	28.14	24.62	22.14	20.24	18.71	17.44	16.36	15.43	14.62
BayesShrink	35.94	31.56	29.43	28.04	26.89	25.89	24.95	24.1	23.39	22.71
HA *BayesShrink*	**36.31**	**31.92**	**29.92**	**28.59**	**27.53**	**26.47**	**25.52**	**24.59**	**23.92**	**23.06**
SureShrink	35.37	31.91	29.39	27.96	25.61	24.73	23.67	22.90	22.46	22.17
HA *SureShrink*	**35.71**	**32.43**	**30.15**	**28.74**	**26.23**	**25.24**	**24.36**	**23.57**	**23.13**	**22.86**

Table 3.8: PSNR results for denoising experiments with *Peppers* image corrupted with different noise powers.

	σ									
Cameraman	5	10	15	20	25	30	35	40	45	50
Initial PSNR	34.15	28.14	24.62	22.14	20.24	18.71	17.44	16.36	15.43	14.62
BayesShrink	35.95	31.27	28.86	27.28	26.07	25.13	24.35	23.69	23.11	22.60
HA *BayesShrink*	**36.45**	**31.85**	**28.57**	**27.96**	**26.79**	**25.81**	**25.02**	**24.34**	**23.82**	**23.03**
SureShrink	35.38	30.93	28.81	26.89	25.68	24.42	23.88	23.06	22.46	22.09
HA *SureShrink*	**35.79**	**31.61**	**29.53**	**27.62**	**26.38**	**25.14**	**24.57**	**23.78**	**23.05**	**22.62**

Table 3.9: PSNR results for denoising experiments with *Cameraman* image corrupted with different noise powers.

	σ									
Monarch	5	10	15	20	25	30	35	40	45	50
Initial PSNR	34.15	28.14	24.62	22.14	20.24	18.71	17.44	16.36	15.43	14.62
BayesShrink	37.20	33.09	30.76	29.27	28.26	27.47	26.79	26.17	25.60	25.07
HA *BayesShrink*	**37.62**	**33.79**	**31.43**	**29.93**	**28.95**	**28.12**	**27.42**	**26.82**	**26.12**	**25.56**
SureShrink	37.05	33.35	30.80	29.31	28.22	27.49	26.82	25.85	25.37	24.61
HA *SureShrink*	**37.46**	**33.91**	**31.43**	**29.95**	**28.97**	**28.25**	**27.42**	**26.46**	**25.96**	**24.93**

Table 3.10: PSNR results for denoising experiments with *Monarch* image corrupted with different noise powers.

	σ									
Average	5	10	15	20	25	30	35	40	45	50
Initial PSNR	34.15	28.14	24.62	22.14	20.24	18.71	17.44	16.36	15.43	14.62
BayesShrink	36.23	32.19	30.04	28.65	27.62	26.79	26.08	25.44	24.87	24.35
HA *BayesShrink*	**36.55**	**32.64**	**30.42**	**29.2**	**28.15**	**27.28**	**26.56**	**25.91**	**25.32**	**24.75**
SureShrink	36.11	32.24	30.05	28.60	27.44	26.42	25.54	24.87	24.38	23.91
HA *SureShrink*	**36.41**	**32.68**	**30.55**	**29.11**	**27.92**	**26.91**	**26.02**	**25.35**	**24.85**	**24.30**

Table 3.11: Averaged PSNR results for denoising experiments.

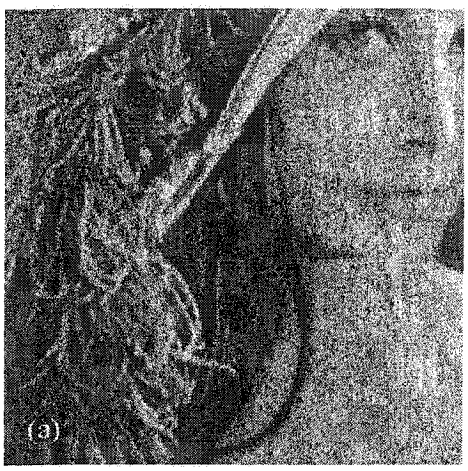

(a) Zoomed Lena image

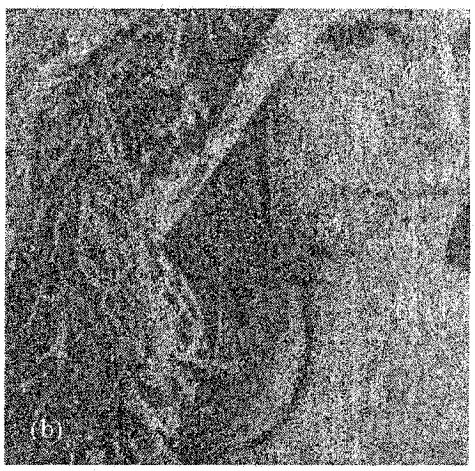

(b) Noisy Lena, PSNR = 22.14 dB

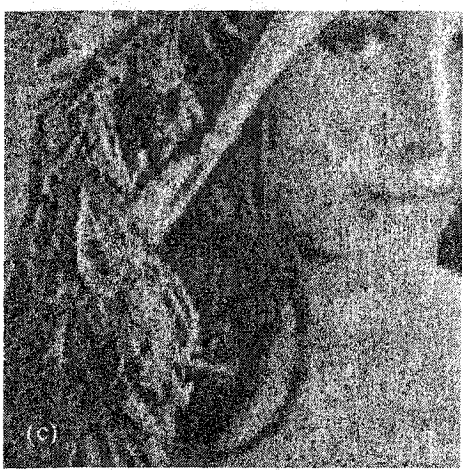

(c) *BayesShrink*, PSNR = 30.19 dB

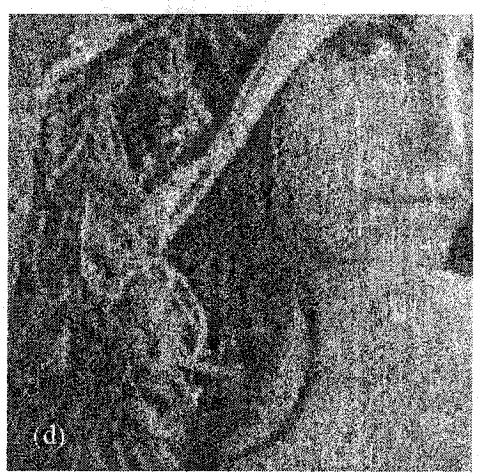

(d) HA *BayesShrink*, PSNR = 30.78 dB

(e) *SureShrink*, PSNR = 30.06 dB

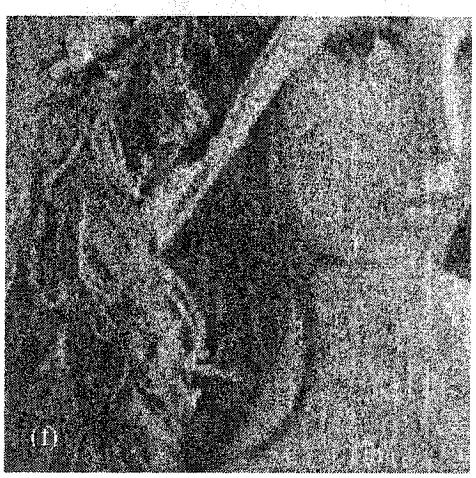

(f) HA *SureShrink*, PSNR = 30.56 dB

Figure 3.5: Performance comparison for different denoising methods with *Lena* corrupted with AWGN having $\sigma = 20$ as input.

(a) Zoomed Goldhill image

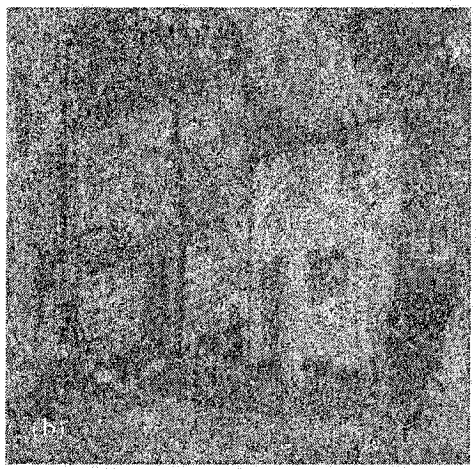

(b) Noisy Goldhill, PSNR = 17.44 dB

(c) *BayesShrink*, PSNR = 26.51 dB

(d) HA *BayesShrink*, PSNR = 26.97 dB

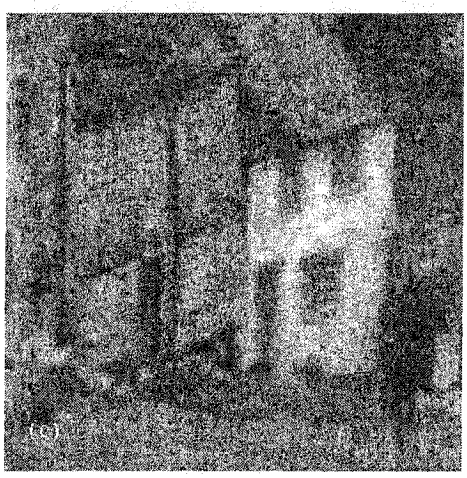

(e) *SureShrink*, PSNR = 26.27 dB

(f) HA *SureShrink*, PSNR = 26.74 dB

Figure 3.6: Performance comparison for different denoising methods with *Goldhill* corrupted with AWGN having $\sigma = 35$ as input.

(a) Zoomed Barbara image

(b) Noisy Barbara, PSNR = 18.71 dB

(c) *BayesShrink*, PSNR = 25.37 dB

(d) HA *BayesShrink*, PSNR = 25.69 dB

(e) *SureShrink*, PSNR = 25.25 dB

(f) HA *SureShrink*, PSNR = 25.54 dB

Figure 3.7: Performance comparison for different denoising methods with *Barbara* corrupted with AWGN having $\sigma = 30$ as input.

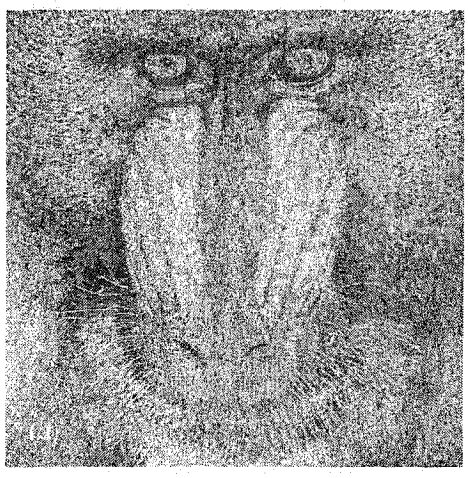

(a) Zoomed Mandrill image

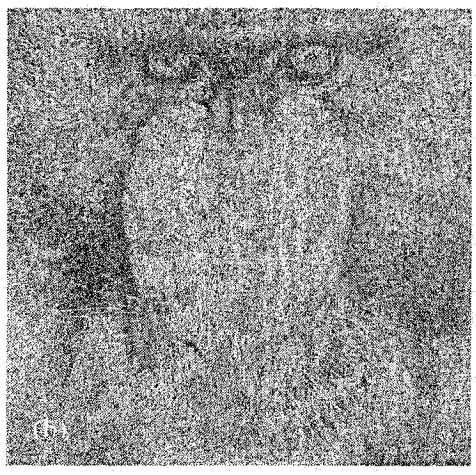

(b) Noisy Mandrill, PSNR = 22.14 dB

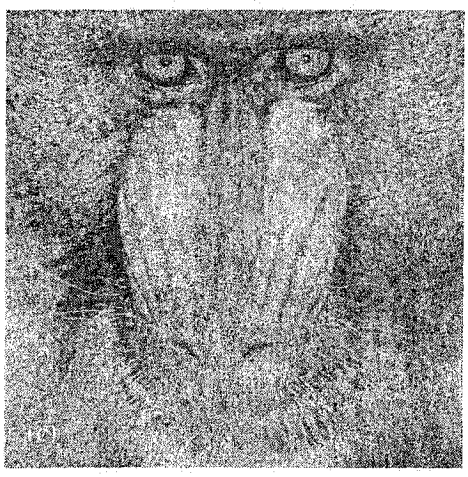

(c) *BayesShrink*, PSNR = 27.56 dB

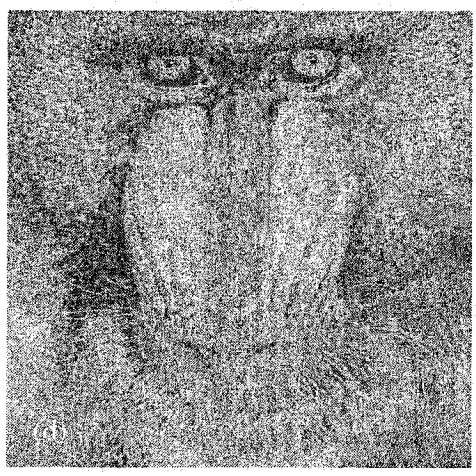

(d) HA *BayesShrink*, PSNR = 28.12 dB

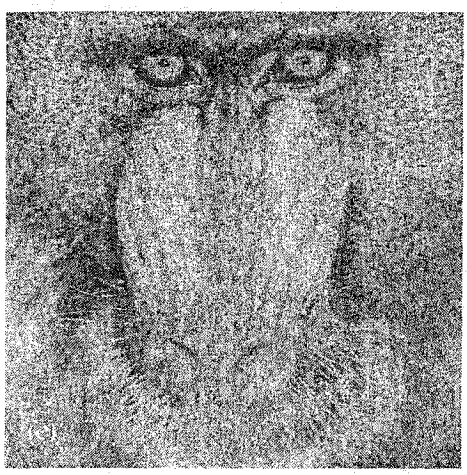

(e) *SureShrink*, PSNR = 27.51 dB

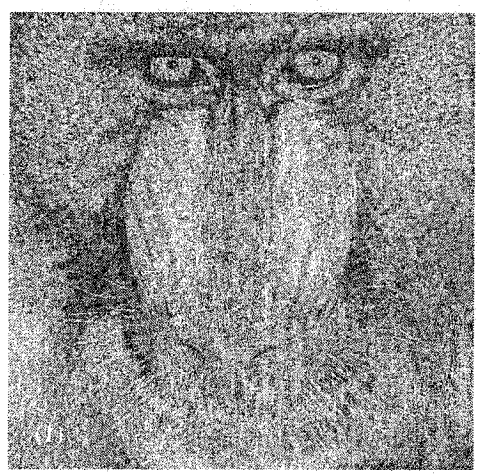

(f) HA *SureShrink*, PSNR = 27.98 dB

Figure 3.8: Performance comparison for different denoising methods with *Mandrill* corrupted with AWGN having $\sigma = 20$ as input.

have been compared with their adapted versions, namely, hierarchically adapted *BayesShrink* (HA *BayesShrink*) and hierarchically adapted *SureShrink* (HA *SureShrink*), respectively.

To estimate the optimal values of the parameters α and β, the PSNR values for the entire dataset of ten images corrupted with ten different noise powers are calculated over a range of values α and β. The values of α and β corresponding to the maximum of the averaged PSNR over the entire dataset are then used to generate the final results. The estimated optimal values of the parameters are $\alpha = 0.43$ and $\beta = 4.3$.

The PSNR from various methods are compared in Tables 3.1-3.10, and the data are collected from an average of ten runs. Since the main comparison is of *SureShrink* with adapted *SureShrink* and of *BayesShrink* with adapted *BayesShrink*, the better one among these is highlighted in bold font for each test set. The adapted thresholds perform better than the original ones in PSNR comparison. The average increase obtained in the PSNR varies from 0.3 dB to 1 dB.

The averaged PSNR over the entire tested dataset for the different noise powers is given in Table 3.11. The proposed adaptation yields an average gian of 0.4–0.8 dB over the subband adaptive thresholds over the entire range of images used.

Figures 3.5-3.8 show the output images resulting from the four considered denoising algorithms as applied to the test images *Lena*, *Barbara*, *Goldhill* and *Mandrill*. The output images produced using the adapted thresholds are visually more pleasing than the outputs using the unadapted thresholds. The noise artifacts visible in the smooth regions in the images for *SureShrink* and *BayesShrink* have been adaptively reduced by a significant amount with the use of the hierarchically adapted thresholds. Also, since the adapted algorithms utilize only one addition, one multiplication, and two divisions more than the original algorithms for each pixel, the computational complexity is not increased very much.

Chapter 4

Joint Denoising and Compression of Images

4.1 Introduction and motivation

While denoising acts to improve the quality of images for the purpose of viewing, lossy compression serves to reduce image size for storage and transmission purposes at the cost of degradation in quality. Subband (wavelet) coders (e.g., [72, 71, 60]) have for long outperformed the discrete cosine transform (DCT)-based systems (e.g., the JPEG standard [73]). Research has been aimed at obtaining maximum compression at the cost of minimum possible distortion. Pixel classification, quantizer design and source encoding have been the center of focus for improvements.

Compression exploits inter-pixel correlation to remove redundancy in the image and reduce the number of bits required to store the information. However, white noise is totally uncorrelated. An image corrupted with additive white Gaussian noise when transformed to a wavelet domain gives rise to image coefficients, which are in turn corrupted with additive Gaussian noise. In case of significant noise variance, it becomes extremely difficult to compress such a set of data while keeping distortion

within reasonable limits. Despite this fact, most of the available coders still do not provide for an adaptive removal of the additive noise in the images and thus, their output suffers in the presence of such corrupting noise.

Figure 4.1 shows the soft-thresholding of wavelet coefficients for denoising and the quantization of the wavelet coefficients for the purpose of compression. Realizing the similarity between the zero-zone quantization of wavelet coefficients in subband coding schemes and the thresholding of these coefficients in denoising, lossy compression has been proposed for denoising in several works ([74, 11, 75, 76, 77]). These are mostly based on Rissanen's minimum description length (MDL) principle [78] and can be interpreted as operating at particular points on the rate-distortion (R-D) curve. Also, as is the case in [11], the resultant compression depends upon the magnitude of the additive noise and fails to yield good compression results with low-noise-corrupted images.

In this chapter, we discuss the development of an adaptive subband (wavelet) coder that performs joint denoising and compression of the input image based both on the additive white Gaussian noise level in the image and the compression rate desired [79].

4.2 Problem statement

Consider an input image that has been corrupted with additive white Gaussian Noise (AWGN). The signal notations in the time and the wavelet transform domain, used in this chapter, are the same as those introduced in Section 3.2. We denote by $\mathbf{X}$ and $\mathbf{Y}$ the set of noise-free and noisy wavelet coefficients, respectively. The set of wavelet coefficients, $\mathbf{Y}$, is obtained by taking a J-level orthogonal wavelet transform of the input noise corrupted image. The coefficients in $\mathbf{X}$ correspond to the original noise-free image and thus, are not available to us.

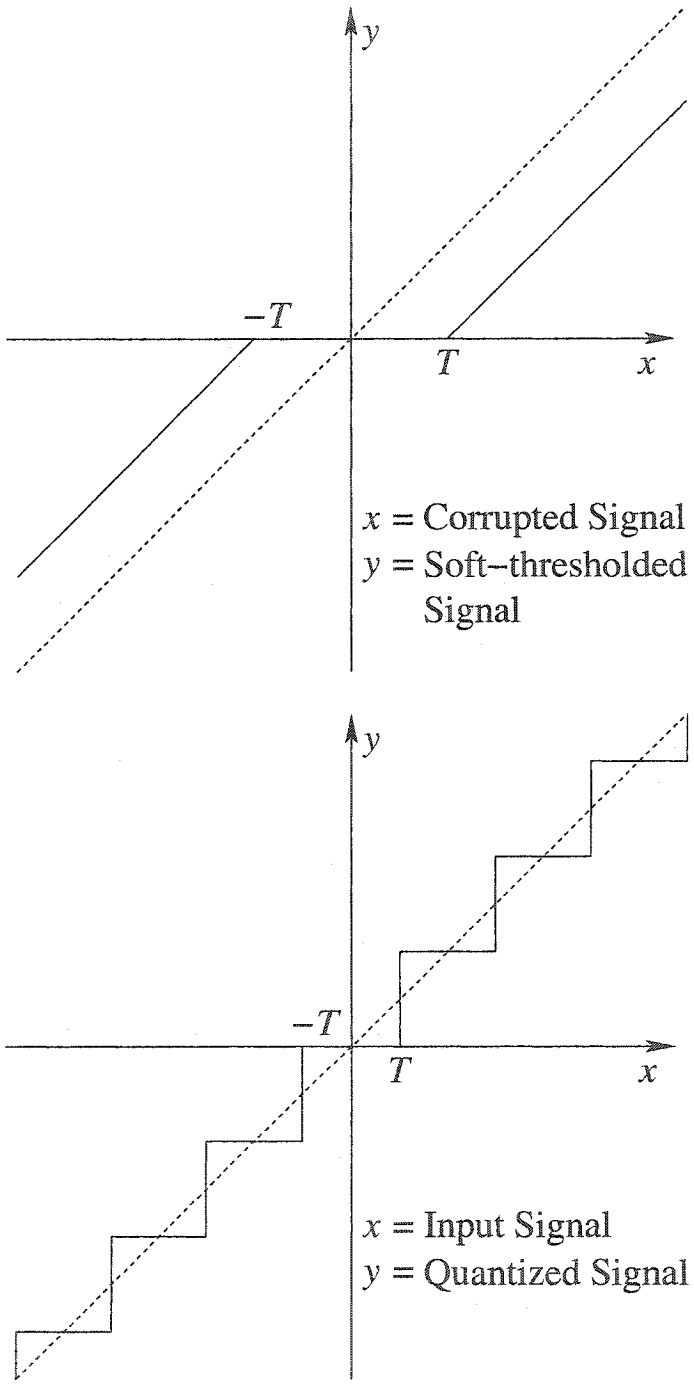

Figure 4.1: Similarity between soft-thresholding used for denoising in the wavelet domain and quantization used for compression

We discuss the problem of jointly denoising and compressing (using context-based classification and quantization with adaptive zero-zone and reconstruction levels) the wavelet coefficient matrix $\mathbf{Y}$ to get a quantized estimate $\hat{\mathbf{X}}$ of $\mathbf{X}$ at the compressor output while minimizing D, the sum of the distortion functions over all the $(3J+1)$ subbands, under the constraint that the output bit rate after source encoding is R. The distortion function for each subband s is defined as

$$D_s(X_{ij}, \hat{X}_{ij}) = \sum_{i=1,j=1}^{i=K,j=L} \left(\hat{X}_{ij} - X_{ij}\right)^2 \tag{4.1}$$

where K and L represent the number of coefficients in each row and column, respectively, of the considered subband s. The total distortion to be minimized is calculated by taking the sum of all the $(3J+1)$ subband distortions,

$$D = \sum_{s=1}^{3J+1} D_s. \tag{4.2}$$

This would have been the standard optimal bit allocation problem as resolved in [80] if the actual image signal transform $\mathbf{X}$ would have been available. But note that we have the noise-corrupted signal $\mathbf{Y}$ instead. To resolve this problem, we estimate a noise threshold parameter, T_B, using *BayesShrink* [11] as discussed in Section 3.5.2 and use this parameter in the quantizer design and context classification.

4.3 Data and rate adaptive quantizer

Centroid reconstruction UTQ is a simple, yet efficient choice as it yields a low complexity approximation for the optimum entropy-constrained scalar quantizer (ECSQ) [81]. The UTQ is completely defined by its fixed step-size Δ and thus has a reduced design and description complexity where the reconstruction levels are optimized by the centroid reconstruction. However, to find the centroid one has to assume an

a priori distribution model for the data to be quantized. In recent literature, the transform coefficients of the original image within each subband have been modeled using a variety of distributions (a brief review of which is provided in Section 3.4.3). Mihcak *et al.* proposed the modeling of each detail wavelet coefficient as conditional Gaussian random variable [65]. Chang et al. have modeled each wavelet coefficient as a generalized Gaussian random variable [11], while Simoncelli *et al.* used a generalized Laplacian model for the subband statistics of the wavelet coefficients [59]. More recently, Tsakalides *et al.* [82] have shown that alpha-stable distribution, a family of heavy-tailed densities, are sufficiently flexible to appropriately model the wavelet coefficients of images in coding applications .

An optimal scalar quantizer has been proposed in [82] for such heavy-tailed alpha-stable distributions. However, no closed form expression is given for the quantizer in [82] and it is computationally expensive. At low bit rates, the quantizer based on a zero mean Laplacian distribution performs almost as well as the quantizer based on the alpha-stable distribution. The closed form expressions resulting from the use of a Laplacian distribution to model the subband coefficients leads to a simple quantizer design and compensates well the small increase in quantization error due to the model mismatch. Thus, in this thesis, we assume that the subband coefficients resulting from the original uncorrupted image, $\{X_{ij} : i = 1, 2, \ldots, K$ and $j = 1, 2, \ldots, L.$ K x $L =$ size of subband$\}$, are i.i.d. random variables from a Laplacian distribution. This is equivalent to considering the $|X_{ij}|$ as i.i.d. data from an exponential source for $f_X(x) = \lambda e^{-\lambda x}$, for $x \geq 0$.

However, as is the case for the problem under consideration, we do not have the original or the desired noise-free images. Instead, we receive AWGN corrupted images, which after the wavelet transform, do not yield the Laplacian distributed subband coefficients. Thus, we have the noise corrupted wavelet coefficients, Y_{ij}, in lieu of the Laplacian distributed uncorrupted coefficients, X_{ij}. Hence, to estimate the mean, λ,

of the exponentially distributed coefficients, $|X_{ij}|$, we calculate the log-likelihood of λ using the K x L noisy observations $\{Y_{ij},\ i = 1, 2, \ldots, K$ and $j = 1, 2, \ldots, L\}$ in a subband. For our purposes, we express the log-likelihood, $l(\lambda)$, of λ as

$$l(\lambda) = \log \prod_{i=1,j=1}^{i=K,j=L} \lambda e^{-\lambda \max(|Y_{ij}| - T_B, 0)}$$

$$\Rightarrow l(\lambda) = KL \log \lambda - \lambda \sum_{i=1,j=1}^{i=K,j=L} \max(|Y_{ij}| - T_B, 0) \tag{4.3}$$

By maximizing the above expression (4.3) with respect to λ, the maximum likelihood estimator (MLE), $\hat{\lambda}$ of λ is obtained as

$$\hat{\lambda} = \frac{KL}{\sum_{i=1,j=1}^{i=K,j=L} \max(|Y_{ij}| - T_B, 0)} \tag{4.4}$$

In [11], the threshold parameter has been used to calculate the zero-zone range. However, a variable rate coder with such a UTQ design adds a significant amount of quantization noise at low required bit-rates and low additive noise content. This occurs because of the small size of the zero-zone, which causes the rest of the coefficients to be quantized coarsely. Thus, we adapt the zero-zone range dependent upon the threshold parameter, T_B, and the number of levels required in the quantizer (Fig. 4.2).

Each of the subbands has a different energy level and variance, with less energy being in the high resolution detail subbands. Thus, each dataset (each subband or each class in case of classification) is quantized using a separate quantizer so as to quantize different coefficients in different subbands or classes according to their variance or energy. Consider a UTQ with $(2L + 1)$ steps that has L bins each for the positive and the negative coefficients. In a standard UTQ, the zero-zone would be limited by

$$\Delta_Z = \frac{\max(|Y_{ij}|)}{2L + 1} \tag{4.5}$$

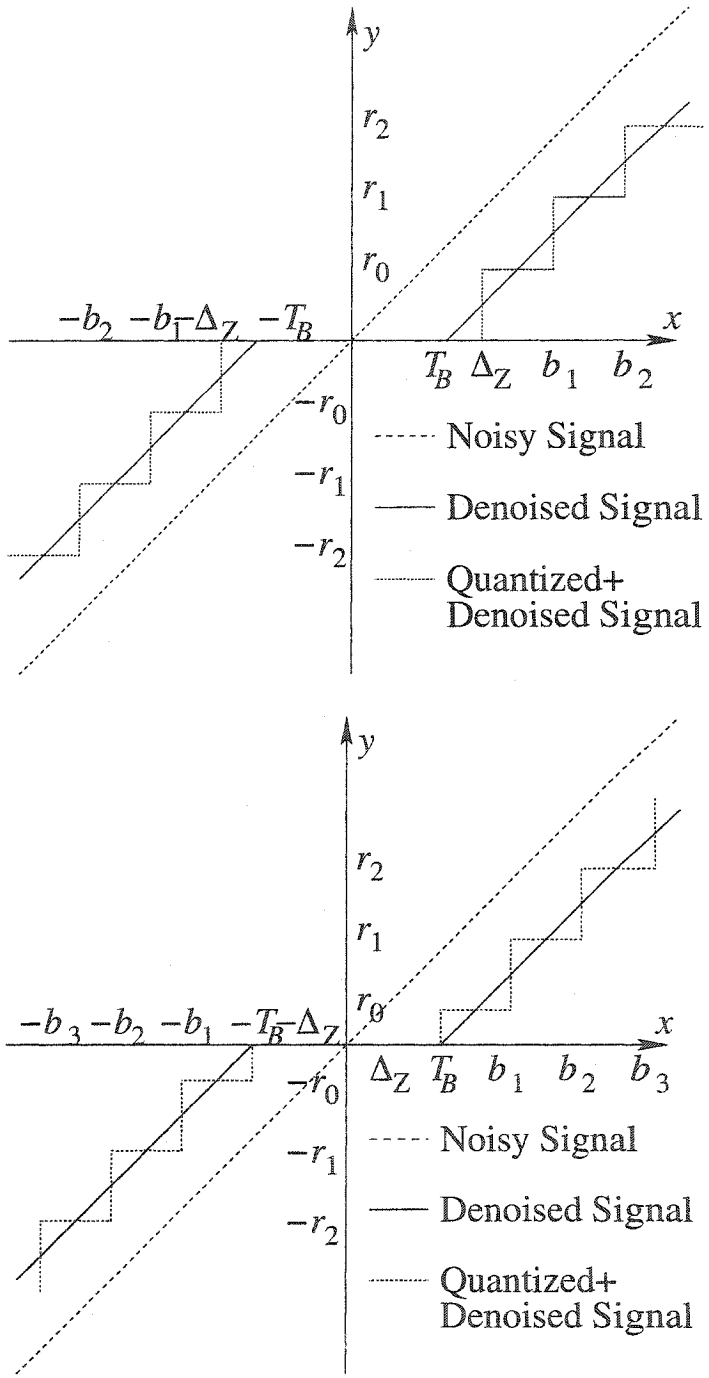

Figure 4.2: Data and rate adaptive quantizer: (a) $\Delta_Z > T_B$; (b) $\Delta_Z < T_B$

For our design, we define the zero-zone as

$$b_0 = \max(T_B, \Delta_Z) \tag{4.6}$$

The rest of the breakpoints on the positive side, $b_1, b_2, \ldots, b_L$, are calculated as

$$b_j = b_0 + j\Delta, \; j = 1, 2, \ldots, L \tag{4.7}$$

where

$$\Delta = \frac{\max(|Y_{ij}| - b_0}{L}. \tag{4.8}$$

For the negative coefficients, the breakpoints are obtained using the symmetry of the designed UTQ, $b_{-j} = -b_j$.

Optimally, the reconstruction levels are obtained using the subband coefficients resulting from the original image. However, in our case, where only the noise corrupted subband coefficients are available, we calculate the reconstruction levels by using the closed form expression made available by the assumption that the absolute values of the subband coefficients of the original uncorrupted image are i.i.d. random variables from an exponential distribution

$$r_j = \frac{(b_j - T_B)e^{-\hat{\lambda}(b_j - T_B)} - (b_{j+1} - T_B)e^{-\hat{\lambda}(b_{j+1} - T_B)}}{e^{-\hat{\lambda}(b_j - T_B)} - e^{-\hat{\lambda}(b_{j+1} - T_B)}} + \frac{1}{\hat{\lambda}}, \text{ for } j = 0, 1, \ldots L-1 \tag{4.9}$$

which reduces to

$$r_j = \frac{(b_j - T_B)e^{-\hat{\lambda}b_j} - (b_{j+1} - T_B)e^{-\hat{\lambda}b_{j+1}}}{e^{-\hat{\lambda}b_j} - e^{-\hat{\lambda}b_{j+1}}} + \frac{1}{\hat{\lambda}}, \text{ for } j = 0, 1, \ldots L-1 \tag{4.10}$$

where the estimated mean, $\hat{\lambda}$, for each subband or class can be calculated using (4.4). For negative coefficients, the reconstruction levels are obtained using the symmetry of the developed UTQ, where $r_{-j} = -r_j$.

This estimation has a good appeal. At low bit rates, the zero-zone width is quite large in a quantizer to achieve the necessary compression and thus, all the noisy coefficients lying below the threshold are automatically set to zero. This causes much of the noise to be eliminated from the quantized image. At higher available bit rate, even if the actual zero-zone width falls below the threshold region, T_B, it is kept at the threshold value to remove the coefficients which are estimated to be present only because of the noise. The modification in the reconstruction levels brings the noise level in the quantized output down. Also, such a scheme works better as compared to a two stage design, where the subband coefficients are soft thresholded first and then quantized. In such a case, a greater number of coefficients are set to zero than is actually required.

An optimal bit allocation algorithm decides the number of levels assigned to each quantizer. The generalized BFOS algorithm [80] minimizes the distortion D at the outputs of all the quantizers under the constraint that the output bit rate of the entropy source encoder is less than or equal to R. Another algorithm given by Shoham *et al.* [83], uses a Lagrange multiplier to minimize the joint rate-distortion (R-D) cost function. An entropy coder, such as the adaptive arithmetic coder, provides the final encoded bit-rate for the minimization requirements in the above algorithms.

4.4 Optimal bit allocation

An important step in compressing the given data is to segregate the data into different classes. Each subband in the wavelet transform domain acts as a class in case the classification of the transform coefficients in the subbands is not done. Depending on the importance of the data it contains, each class is allocated a portion of the total bit budget, such that the compressed image has the minimum possible distortion. This procedure is called *Bit Allocation.*

Algorithm 2 Optimal bit allocation using the generalized BFOS algorithm

STEP I Initially, allocate to each class or subband, s, a predefined maximum number of bits, $B(s)$.

STEP II For each class, reduce one bit from its quota of allocated bits, and calculate the distortion due to the reduction of that one bit.

STEP III Of all the classes, reduce one bit from the class having the minimum distortion for a reduction of one in STEP II.

STEP IV Calculate the total distortion, D, for all classes using (5.11).

STEP V Calculate the total rate for all the classes as

$$R_t = \sum_{i=1}^{C} p(i)B(i),$$

where $p(i)$ is the total probability of the i^{th} class or subband, which is computed using (4.13) and $B(i)$ is the allocated number of bits for the i^{th} class or subband and C is the total number of classes or subbands.

STEP VI Compare the target rate R with R_t. If $R < R_t$, then GOTO STEP II, else STOP.

The R-D theory is often used for solving the problem of allocating bits to a set of classes, or for bit-rate control in general. The theory aims at reducing the distortion for a given target bit-rate, by optimally allocating bits to the various classes or subbands of data. One approach to solve the problem of *optimal* bit allocation using the R-D theory is the generalized BFOS algorithm given in [80]. The algorithm is described in Algorithm 2.

In the bit allocation algorithm, bits $B(s)$ are allocated to each class or subband and the distortion is computed. For a class or subband s having a total number of coefficients N_s (K rows and L columns) we compute the distortion as

$$D_s(\widetilde{X}_{ij}, Y_{ij}^Q) = \sum_{i=1,j=1}^{i=K,j=L} \left(\widetilde{X}_{ij} - Y_{ij}^Q\right)^2 \tag{4.11}$$

where Y_{ij}^Q are obtained by the quantization of the available noisy coefficients in each

class, Y_{ij}, using the quantizer defined by (4.6-4.10) with $L = 2^{B(i)}$ steps, and $\widetilde{X}_{ij}$ is obtained as

$$\widetilde{X}_{ij} = \text{sign}(Y_{ij}) \max(|Y_{ij}| - T_B, 0). \tag{4.12}$$

When the optimality is achieved in bit allocation, the quantized output, Y_{ij}^Q, is equivalent to the required denoised and quantized estimate, $\hat{X}_{ij}$, of the noise-free image subband coefficients, X_{ij}.

The probability of occurrence of the class or subband s needs to be computed in Algorithm 2 and we define it as

$$p(s) = \frac{N_s}{NM} \tag{4.13}$$

where N_s is the number of coefficients in the class and N and M are the number of rows and columns in the full image, respectively. In the generalized BFOS approach, one bit is reduced at a time until optimality is achieved either in the distortion or the target rate, or both.

4.5 Context-based classification

An extensive study by Joshi *et al.* [84] on various classification-based compression algorithms demonstrates substantial gains in subband image coding applications. We use a classification scheme similar to that used by Yoo *et al.* [85], but appropriately modify it to account for the noisy coefficients and joint compression and denoising. Since the data being classified is the output of the quantizer, or in more realistic terms, an estimation of the quantizer output, as we do not have the quantizer output, the overhead involved with such a scheme is quite low.

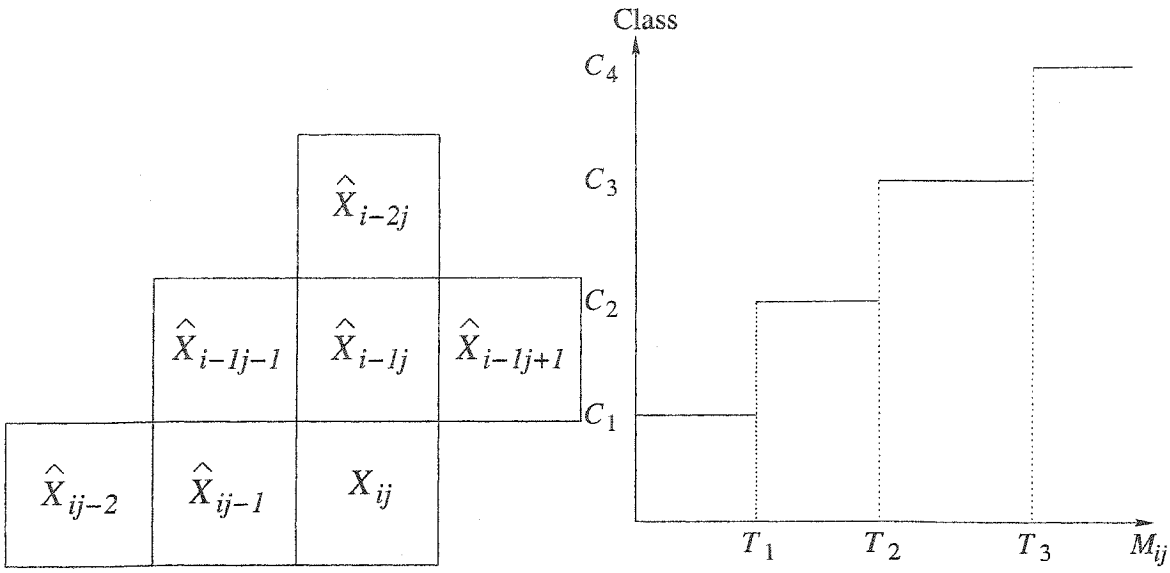

Figure 4.3: (a) Causal template composed of 6 quantized coefficients that is used as the classification context, (b) Classification of the predicted activity into different classes

4.5.1 Activity computation

For this classification, the activity, M_{ij}, of each quantized coefficient is calculated using a causal model involving 6 coefficients (see Fig. 4.3) as

$$M_{ij} = a_0|\hat{X}_{i-1j}| + a_1|\hat{X}_{ij-1}| + a_2|\hat{X}_{i-1j-1}| + a_3|\hat{X}_{i-1j+1}| + a_4|\hat{X}_{i-2j}| + a_5|\hat{X}_{ij-2}| \quad (4.14)$$

where $\hat{X}_{ij}$ are the estimated quantized and denoised outputs and a_k, $0 \leq k \leq 5$, are weights satisfying $\sum_{k=1}^{5} a_k = 1$ and are determined experimentally. This predicted activity is then compared with calculated classification thresholds to determine the class for Y_{ij}.

However, note that we do not have the quantized coefficients *a priori* or even the original image subband coefficients, X_{ij}. As in [85], we approximate the output of the quantizer by quantizing the subband coefficients with a uniform quantizer having a step size close to what we finally expect. However, keeping in mind the denoising that is to be performed in the output, the coefficients, $\widetilde{X}_{ij}$ are used for uniform

quantization and are obtained using (4.12). Note that $\widetilde{X}_{ij}$ are obtained in a fashion similar to soft thresholding [37].

The activity, M_{ij}, for each coefficient is thus calculated using the absolute values of uniformly quantized $\widetilde{X}_{ij}$ in (4.14).

4.5.2 Classification thresholds

For threshold calculation, we follow the same algorithm as in [85, 60] but with a modified estimation of the mean of each class. To classify subband coefficients into N classes, choose $(N_0 - 1)$ initial thresholds T_k and N_0 initial classes such that $N_0 \gg N$ and there are approximately an equal number of coefficients in each class.

The steps to estimate the classification thresholds $\{T_1, T_2, \ldots, T_{N-1}\}$ are described in Algorithm 3. The activity calculated in the previous section is compared with the class thresholds T_k to place the corresponding coefficients Y_{ij} in different classes. The class means estimated in STEP I of Algorithm 3, $\hat{\lambda}_k$, can be utilized for quantizer design as described in Section 4.3.

4.6 Final algorithm for joint denoising and compression of images

The final algorithm for the joint denoising and compression of images is presented in Algorithm 4. The block diagram of the scheme is also presented in Fig. 4.4.

For the reconstruction of the compressed and denoised image on the receiver side, the estimated means and the classification thresholds are used to reclassify and reconstruct the coefficients. Then, the inverse wavelet transform of the coefficients would result in the denoised and compressed estimate of the original noise-free image.

Algorithm 3 Estimation of classification thresholds

STEP I Although the subband coefficients of the original image have been assumed to be Laplacian distributed, the subband coefficients obtained from the AWGN corrupted available image are not Laplacian distributed. Thus, the estimates of the means, $\hat{\lambda}_0, \hat{\lambda}_1, \ldots, \hat{\lambda}_{N_0-1}$ are found using

$$\hat{\lambda}_s = \frac{N_s}{\sum |\widetilde{X}_{ij}|},$$

where $\widetilde{X}_{ij} \in$ class s and N_s is the total number of coefficients in class s. Set $K = N_0$.

STEP II Find k^* such that

$$k^* = \arg \min_{0 \le k \le K} \frac{\hat{\lambda}_k^{2r_k} \hat{\lambda}_{k+1}^{2r_{k+1}}}{\hat{\lambda}_{k'}^2}$$

where $r_k = \frac{N_k}{(N_k+N_{k+1})}$, $r_{k+1} = 1 - r_k = \frac{N_{k+1}}{(N_k+N_{k+1})}$ and $\hat{\lambda}_{k'} = \frac{(N_k+N_{k+1})}{(\frac{N_k}{\hat{\lambda}_k} + \frac{N_{k+1}}{\hat{\lambda}_{k+1}})}$.

STEP III Merge classes C_{k^*} and C_{k^*+1}. For $k = k^*$ do

$$C_k = C_{k^*} \cup C_{k^*+1} \text{ and } \hat{\lambda}_k = \hat{\lambda}_{k'}.$$

For $k > k^*$, do

$$C_k = C_{k+1},\ T_k = T_{k+1} \text{ and } \hat{\lambda}_k = \hat{\lambda}_{k+1}.$$

STEP IV Set $K = K - 1$. STOP if $K = N$. Otherwise GOTO STEP II.

Algorithm 4 Proposed scheme for joint denoising and compression of images corrupted with AWGN

STEP I Decompose the corrupted image in to J detail levels using DWT.

STEP II Estimate the threshold level for the noise corrupted subband coefficients using *BayesShrink*.

STEP III Perform the classification of the subband data into N number of classes as described in Section 4.5.

STEP IV Quantize each class using the data and rate adaptive quantizer described in Section 4.3.

STEP V Use any entropy coder, such as an adaptive arithmetic coder, to generate the encoded bit stream.

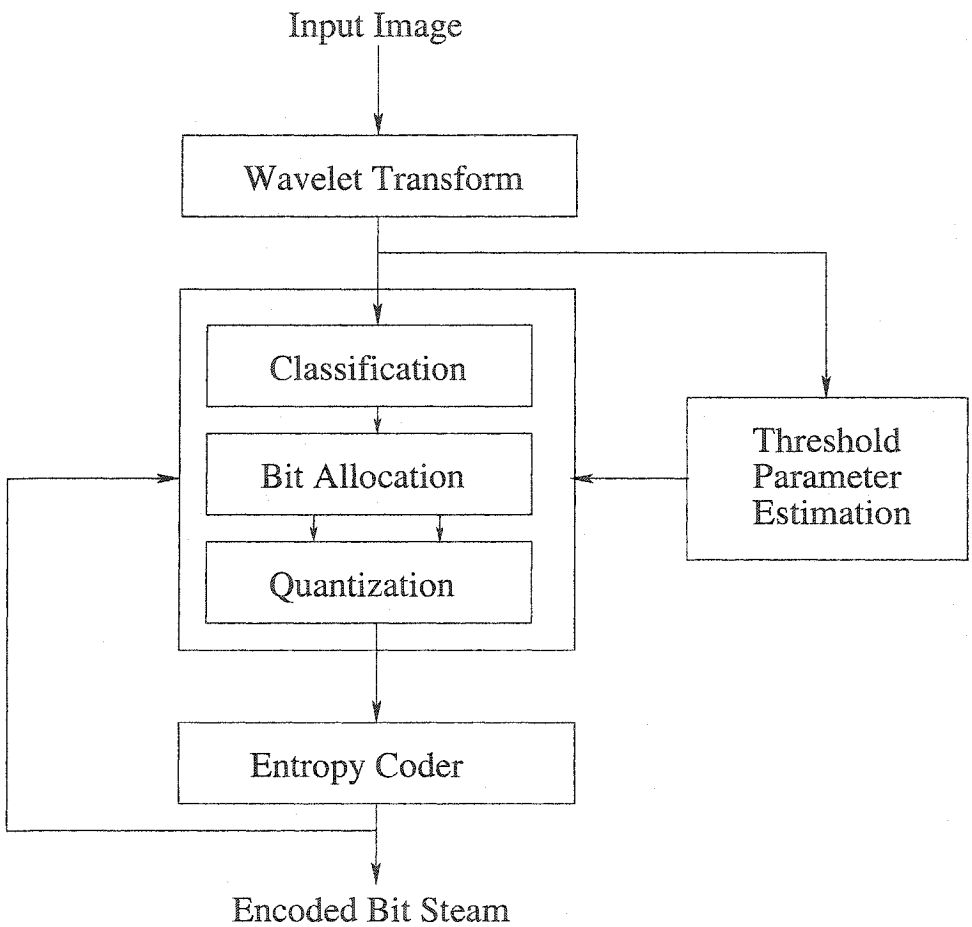

Figure 4.4: Block diagram of the data and rate adaptive encoder for images corrupted with AWGN.

4.7 Joint denoising and compression of medical ultrasound images

4.7.1 Introduction

Ultrasonography has emerged as one of the most powerful techniques for imaging organs and soft tissue structures in the human body. It is noninvasive, portable, versatile and relatively low-cost. Thus, today, it is being used at an ever-increasing rate for medical diagnostics. The influence of tele-medicine has been increasing at a fast rate and this has further fuelled the emergence of ultrasonography as an important diagnostic tool.

However, like all coherent imaging processes, narrow-band ultrasound suffers from speckle noise. Speckle occurs when the surface roughness of the object being imaged is of the order of the wavelength of the coherent source radiation incident on the surface [86] and is generated by interaction of the reflected waves from various independent scatterers within a resolution cell [87]. In images generated as a result of these processes, the speckle manifests itself as a random pixel-to-pixel multiplicative noise having a granular appearance that makes it very difficult to visually or automatically interpret the image data. Therefore, speckle removal is a critical preprocessing step in many coherent imaging tasks, such as segmentation and classification.

The storage required for the large amount of data being generated, coupled with the need to transmit it on the communication channels for the purpose of tele-medicine, has created a pressing need for compression of such medical ultrasound images. The speckle present in the image increases the entropy of the image. In the case of a significant input noise, it becomes extremely difficult to compress such an image while keeping the distortion within reasonable limits. In fact, for the case of multiplicative speckle noise corrupted ultrasound images, no compression method has been proposed that specifically accounts for the corrupting speckle while compressing

the image.

In this section, we demonstrate the application of the proposed data and rate adaptive quantizer and the classification scheme to such medical ultrasound images corrupted with multiplicative speckle noise [88]. To address the multiplicative nature of the speckle noise, we follow a homomorphic approach developed by Jain [86], which by taking the logarithm of the image, converts the multiplicative noise into additive noise. We then apply the proposed adaptive subband (wavelet) coder that performs joint denoising and compression of the log-transformed input ultrasound image based both on the noise level in the image and the compression rate desired.

4.7.2 Speckle noise model and the modified algorithm

A general model for images corrupted with speckle noise was proposed by Jain [86] and was also used by Zong [89] and Achim *et al.* [90]. We describe the speckle model in the following discussion.

Denote by $\mathbf{v} = \{v_{ij} : i = 1, 2, \ldots, N \text{ and } j = 1, 2, \ldots, M\}$ a noisy observation (i.e., the recorded speckled image) of the original two-dimensional image $\mathbf{u} = \{u_{ij} : i = 1, 2, \ldots, N \text{ and } j = 1, 2, \ldots, M\}$. Let η and ϑ be the sets of corrupting multiplicative and additive speckle noise components, respectively. The received speckle corrupted image can be expressed as

$$v_{ij} = u_{ij}.\eta_{ij} + \vartheta_{ij}, \; i = 1, 2, \ldots, N \text{ and } j = 1, 2, \ldots, M. \tag{4.15}$$

Generally, the effect of the additive component of the speckle noise is less significant than the multiplicative component in medical ultrasound images. Thus, in what follows we will neglect the additive term and express (4.15) as

$$v_{ij} = u_{ij}.\eta_{ij}, \; i = 1, 2, \ldots, N \text{ and } j = 1, 2, \ldots, M. \tag{4.16}$$

A detailed study of the statistical properties of speckle noise η was provided by Goodman [87]. Some of the realistic speckle noise models that have been proposed in literature include the K-distribution [91], Gamma distribution [92], log-normal distribution [93], and correlated speckle pattern [90], [91]. Following [93, 94], we use a *log-normal* distribution to describe the speckle statistics in the time domain.

If a random variable X follows a log-normal distribution, then $\ln X$ follows a normal distribution with mean μ and variance σ^2. A log-normal random variable can be generated using

$$X_{log-normal} = \exp\left(X_{normal}\sqrt{2\log\frac{M}{m}} + \ln m\right) \tag{4.17}$$

where M and m are the mean and median values of the distribution, respectively, while X_{normal} is a zero-mean, unit-variance Gaussian random variable. For the log-normal distribution, the mean and variance are given by

$$M = \exp\left(\mu + \frac{\sigma^2}{2}\right) \tag{4.18}$$

$$\sigma^2_{log-normal} = \exp\left(2\mu + 2\sigma^2\right) - \exp\left(2\mu + \sigma^2\right) \tag{4.19}$$

A usual way to estimate the speckle noise in speckle corrupted images is to calculate the mean-to-standard-deviation ratio, also termed as the equivalent number of looks (ENL). The ENL of a speckle corrupted image can be expressed as

$$\left(\frac{\text{mean of the speckle corrupted image}}{\text{standard deviation of the speckle corrupted image}}\right)^2 = \text{ENL} = \text{constant} \tag{4.20}$$

For the log-normal distribution there exists a straight-forward equivalence between the ENL in a speckle corrupted image and the median of the log-normal distribution [90].

In order to transform the multiplicative speckle noise model in (4.16) to an additive

Algorithm 5 Modified algorithm for joint denoising and compression of ultrasound images corrupted with multiplicative speckle

STEP I	Perform the homomorphic operation by taking the logarithm of the image.
STEP II	Decompose the corrupted image in to J detail levels using DWT.
STEP III	Estimate the threshold level for the noise corrupted subband coefficients using *BayesShrink*.
STEP IV	Perform the classification of the subband data into N number of classes as described in Section 4.5.
STEP V	Quantize each class using the data and rate adaptive quantizer described in Section 4.3.
STEP VI	Use any entropy coder, such as an adaptive arithmetic coder, to generate the encoded bit stream.

noise model, we use the homomorphic operation. Thus, taking the logarithm of (4.16) we have

$$\ln v_{ij} = \ln u_{ij} + \ln \eta_{ij},\ i = 1, 2, \ldots, N \text{ and } j = 1, 2, \ldots, M. \tag{4.21}$$

We rewrite expression (4.21) as follows

$$g_{ij} = x_{ij} + \varepsilon_{ij},\ i = 1, 2, \ldots, N \text{ and } j = 1, 2, \ldots, M. \tag{4.22}$$

where, g_{ij}, x_{ij} and ε_{ij} are the logarithms of v_{ij}, u_{ij} and η_{ij}, respectively, and N x M is the size of the image. We now consider ε_{ij} as an additive noise coefficients that are independent of x_{ij} and follow a normal distribution .

We now apply the algorithm described in Section 4.6 to the resultant image that is corrupted with additive white Gaussian noise. The entire algorithm for the case of multiplicative speckle-corrupted medical ultrasound images can be thus described as in Algorithm 5, where a homomorphic operation is performed in addition to Algorithm 4 to convert the multiplicative speckle to additive Gaussian noise (see also Fig. 4.5).

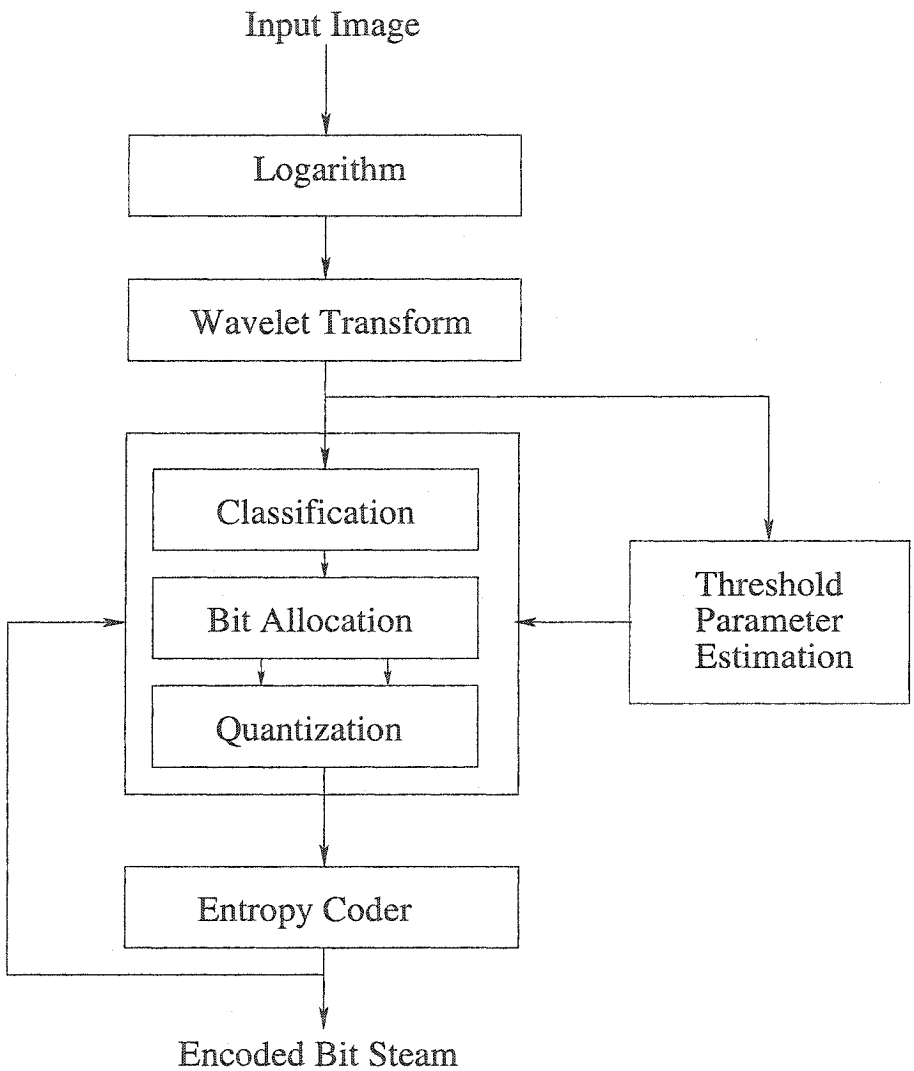

Figure 4.5: Block diagram of the data and rate adaptive encoder for medical ultrasound images corrupted with multiplicative speckle noise.

4.8 Experimental results and discussions

4.8.1 For additive White Gaussian noise

We have implemented a variable rate image coder based on classification and quantization schemes that take into account the noise level in the image while classifying and quantizing. Test images include the 512x512 pixel size natural images *Goldhill*, *Lena*, *Barbara*, and *Mandrill* and an 256x256 pixel size artificial computer generated image *Synthetic*. The algorithm has been tested for six different noise powers corresponding to noise standard deviations of 10, 15, 20, 25, 30 and 35. The performance of the proposed subband coder with data and rate adaptive quantizer, which we call AQ, has been compared with the state-of-the-art MDL principle-based joint compression and denoising scheme (MDLQ). We also present results where classification has been used along with AQ (C+AQ).

A 4-level dyadic decomposition of the images has been performed using the 9/7-tap bi-orthogonal wavelet filters. Bit allocation for different classes (or subbands) has been performed by using the generalized BFOS algorithm [80], which minimizes the output distortion under the output source entropy constraint. An adaptive arithmetic coder is used to produce the output bit stream. The proposed classification (4 classes) and quantization have been applied to the detail subbands only. The approximation subband has been modeled as a uniform distribution and a uniform quantizer has been used on this subband. The overhead rate includes the 16 bits to specify each of the classification thresholds and the estimated $\hat{\lambda}$ for each class.

The weighting coefficients a_k in the classification algorithm are estimated experimentally so as to maximize the gain achieved during classification. This maximization is using the average PSNR gain for the entire image database when classification is employed.

In order to show that the original image wavelet subband coefficients can be

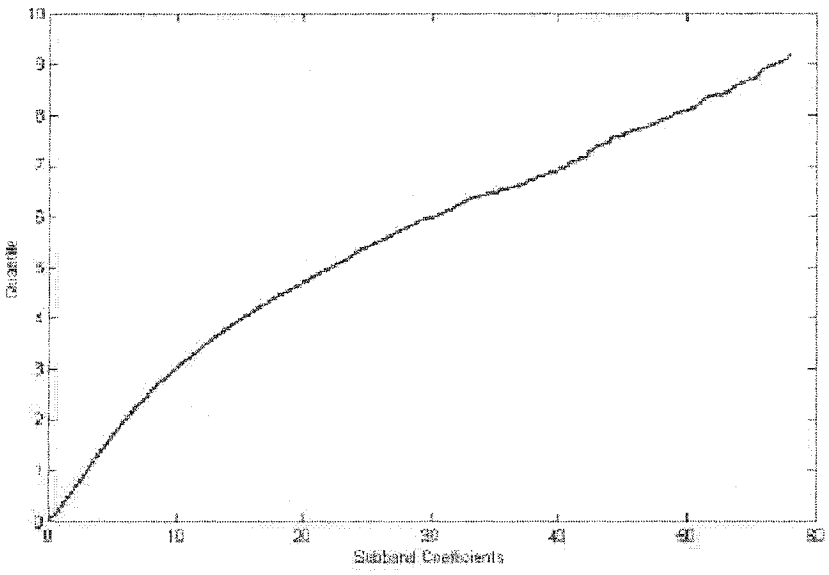

Figure 4.6: The Q-Q plot of the HL_1 subband coefficients of image *Lena* against a Laplacian distributed set of data. The magnitude of the subband coefficients has been taken for the plot.

approximated as a Laplacian distribution, the Q-Q plot of the subband coefficients of the HL_1 subband of Lena is plotted in Figure 4.6. The quantile plot is an effective and frequently used statistical tool to verify if a data set conforms to an assumed distribution. The relatively straight line in Figure 4.6 justifies the approximation of the subband coefficients by a Laplacian distribution.

To validate the classification algorithm, the mean and variance of the data in one of the detail subbands of Lena and Barbara, classified to the 4 different classes, respectively, has been presented in Table 4.1. The data in each of the 4 classes has a mean that is approximately zero and the variance of the classes has been classified in an increasing order. Figure 4.7 shows the 4-level classification of the subband data from one subband each of Lena and Barbara. The brighter regions represent areas with greater activity and have been identified successfully.

Tables 4.2-4.6 compare the PSNR performance of the proposed data and rate adaptive UTQ (AQ)-based coder with MDLQ at different noise standard deviations

	Class 1	Class 2	Class 3	Class 4
Lena				
Mean	0.431	-0.598	0.688	-0.718
Variance	544.09	764.06	1241.3	2818.4
Barbara				
Mean	0.0533	0.0640	0.0512	0.4596
Variance	110.59	166.78	913.13	3321.0

Table 4.1: Mean and variance of coefficients in different classes for a 4-level classification of the HL_2 detail subband of *Lena* and the HL_1 detail subband of *Barbara*.

Goldhill	σ/ bit-rate (bpp)					
	10/1.0703	15/0.7159	20/0.5382	25/0.4304	30/0.4304	35/0.3206
Initial PSNR	28.12	24.59	22.10	20.16	18.57	17.24
MDLQ	30.35	28.64	27.58	26.29	25.61	24.84
AQ	30.93	29.03	27.81	27.23	26.66	26.40
C+AQ	**31.13**	**29.43**	**28.48**	**27.58**	**26.99**	**26.42**

Table 4.2: Performance comparison (in PSNR) for the test image *Goldhill* corrupted with different additive noise powers.

Lena	σ/ bit-rate (bpp)					
	10/0.6775	15/0.5003	20/0.4049	25/0.3459	30/0.3006	35/0.2730
Initial PSNR	28.12	24.59	22.10	20.16	18.57	17.24
MDLQ	31.88	30.44	29.49	28.66	27.68	26.03
AQ	32.19	30.23	29.46	28.57	27.72	27.21
C+AQ	**33.12**	**31.41**	**30.40**	**29.44**	**28.75**	**28.03**

Table 4.3: Performance comparison (in PSNR) for the test image *Lena* corrupted with different additive noise powers.

Barbara	σ/ bit-rate (bpp)					
	10/1.0999	15/0.9814	20/0.8859	25/0.7883	30/0.6837	35/0.5935
Initial PSNR	28.12	24.59	22.10	20.16	18.57	17.24
MDLQ	28.61	27.29	25.96	24.74	24.26	23.67
AQ	28.84	27.44	26.23	25.06	24.64	23.95
C+AQ	**30.34**	**28.49**	**27.36**	**26.29**	**25.03**	**24.50**

Table 4.4: Performance comparison (in PSNR) for the test image *Barbara* corrupted with different additive noise powers.

(a) Lena Image (b) Barbara Image

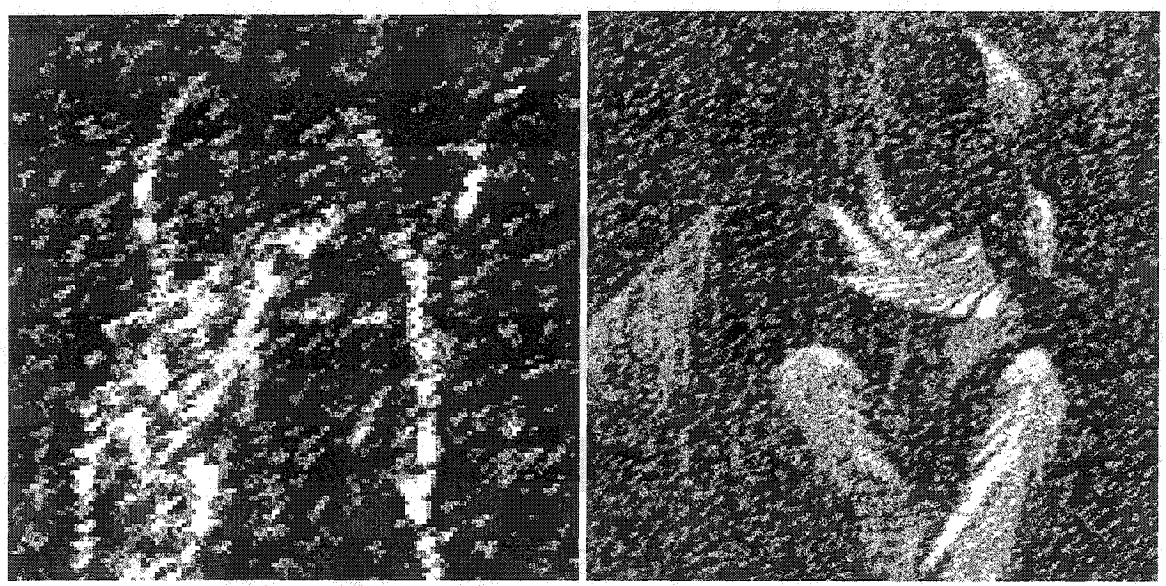

(c) Classified HL2 detail subband of Lena (d) Classified HL1 detail subband of Barbara

Figure 4.7: 4-level classification of one subband each of *Lena* and *Barbara* images corrupted with AWGN having $\sigma = 20$.

Mandrill	σ/ bit-rate (bpp)					
	10/1.50	15/1.191	20/1.0389	25/0.9161	30/0.8141	35/0.7288
Initial PSNR	28.12	24.59	22.10	20.16	18.57	17.24
MDLQ	26.03	24.35	23.36	22.63	22.03	21.52
AQ	26.62	24.59	23.48	22.90	22.23	21.63
C+AQ	**27.10**	**25.38**	**24.03**	**23.36**	**22.56**	**22.07**

Table 4.5: Performance comparison (in PSNR) for the test image *Mandrill* corrupted with different additive noise powers.

Synthetic	σ/ bit-rate (bpp)					
	10/0.9696	15/0.6066	20/0.4398	25/0.3723	30/0.3054	35/0.2741
Initial PSNR	28.12	24.59	22.10	20.16	18.57	17.24
MDLQ	33.04	30.58	29.34	27.96	26.95	26.34
AQ	33.47	31.10	30.21	29.34	28.75	28.26
C+AQ	**34.08**	**31.42**	**30.68**	**29.40**	**28.96**	**28.48**

Table 4.6: Performance comparison (in PSNR) for the test image *Synthetic* corrupted with different additive noise powers.

for different test images. The PSNR has been calculated using the original, uncorrupted image and the denoised and compressed outputs. The results of the proposed classification (C+AQ) have also been presented in the table. The bits per pixel at which the outputs of the proposed schemes (AQ and C+AQ) have been generated are the same as those produced in the output of MDLQ. The proposed scheme AQ gives an average improvement of about 0.5 dB in the PSNR values. For computer-generated images like Synthetic, an increase of almost 1 dB over MDLQ is obtained for all noise levels. Classification results in a further increase of 0.5 dB to 1 dB over the non-classified scheme, AQ.

The output images (Figs. 4.8, 4.9, 4.10, 4.11 and 4.12) produced by AQ are more visually pleasing and have less amount of quantization noise added to them. The finer details like hair in *Lena*, the windows in *Goldhill* and the edges of the geometric shapes in *Synthetic* are much better preserved in the AQ outputs as compared to the outputs of MDLQ. In the smoother regions also, lot less noise spikes are visible.

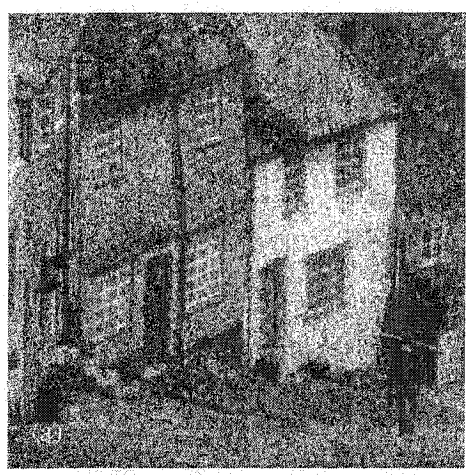

(a) Zoomed Goldhill Image

(b) Noisy Goldhill, PSNR = 20.16 dB

(c) MDLQ, PSNR = 26.29 dB, bpp = 0.43

(d) AQ, PSNR = 27.23 dB, bpp = 0.43

(e) C+AQ, PSNR = 27.58 dB, bpp = 0.43

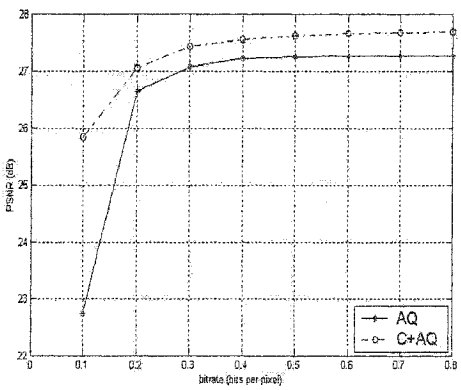

(f) Rate-Distortion curve

Figure 4.8: (a)-(e) Performance comparison of various methods on *Goldhill* corrupted with AWGN having $\sigma = 25$. (f) Rate-Distortion curve for the proposed methods with *Goldhill* corrupted with AWGN having $\sigma = 25$ as input.

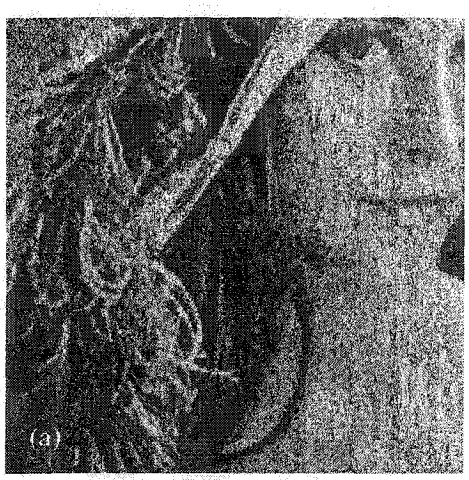

(a) Zoomed Lena Image

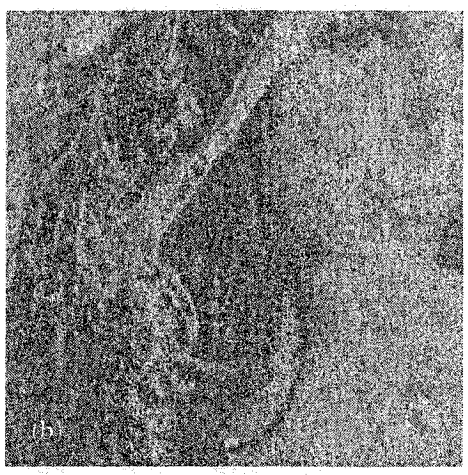

(b) Noisy Lena, PSNR = 17.24 dB

(c) MDLQ, PSNR = 26.03 dB, bpp = 0.273

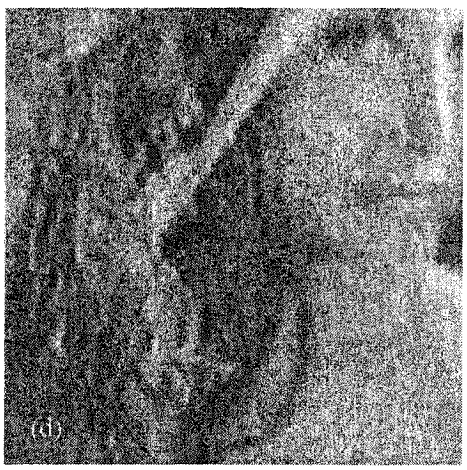

(d) AQ, PSNR = 27.21 dB, bpp = 0.273

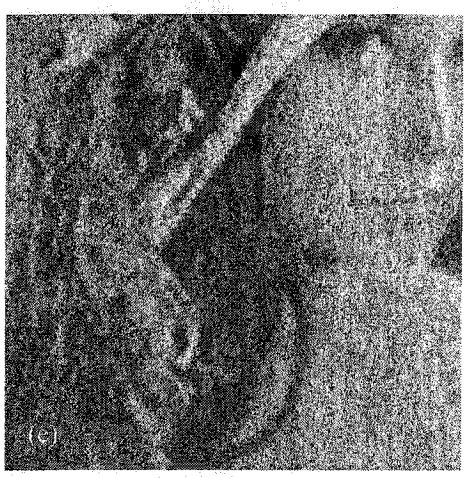

(e) C+AQ, PSNR = 28.03 dB, bpp = 0.273

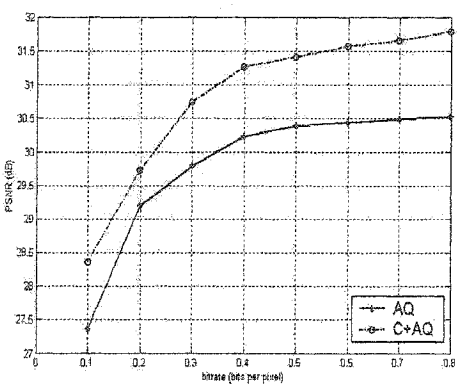

(f) Rate-Distortion curve

Figure 4.9: (a)-(e) Performance comparison of various methods on *Lena* corrupted with AWGN having $\sigma = 35$. (f) Rate-Distortion curve for the proposed methods with *Lena* corrupted with AWGN having $\sigma = 15$ as input.

(a) Zoomed Barbara Image

(b) Noisy Barbara, PSNR = 24.59 dB

(c) MDLQ, PSNR = 27.29 dB, bpp = 0.98

(d) AQ, PSNR = 27.44 dB, bpp = 0.98

(e) C+AQ, PSNR = 28.49 dB, bpp = 0.98

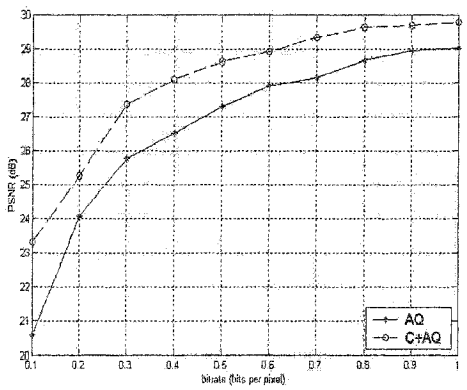

(f) Rate-Distortion curve

Figure 4.10: (a)-(e) Performance comparison of various methods on *Barbara* corrupted with AWGN having $\sigma = 15$. (f) Rate-Distortion curve for the proposed methods with *Barbara* corrupted with AWGN having $\sigma = 10$ as input.

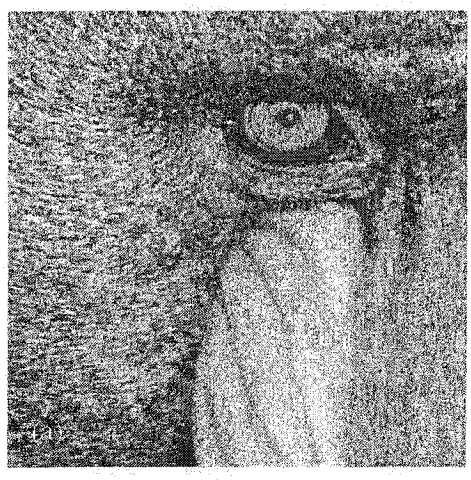

(a) Zoomed Mandrill Image

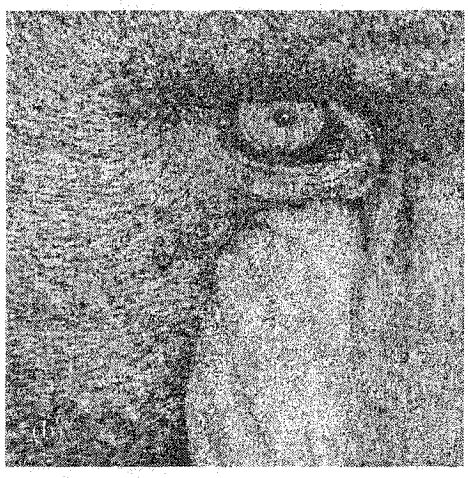

(b) Noisy Mandrill, PSNR = 28.12 dB

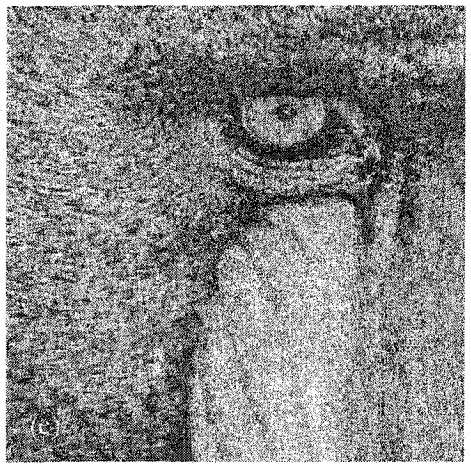

(c) MDLQ, PSNR = 26.03 dB, bpp = 1.5

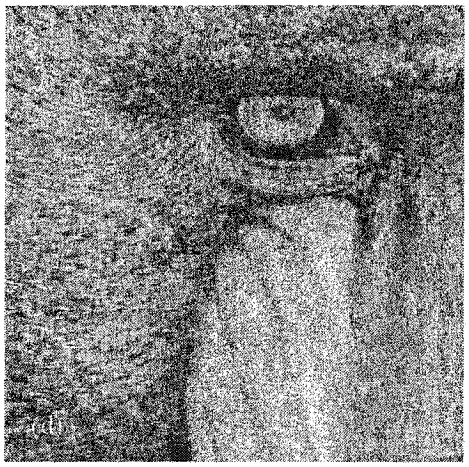

(d) AQ, PSNR = 26.62 dB, bpp = 1.5

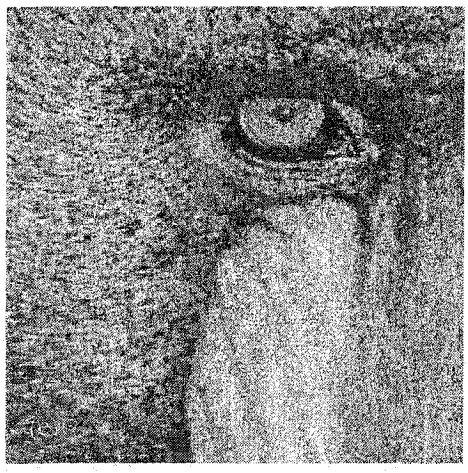

(e) C+AQ, PSNR = 27.1 dB, bpp = 1.5

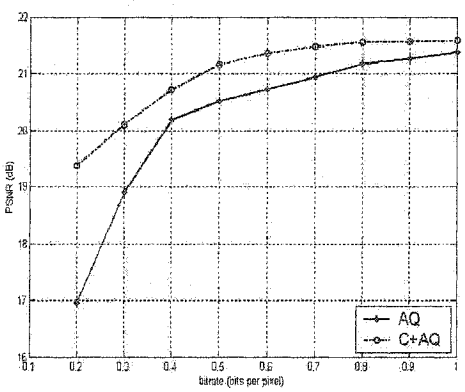

(f) Rate-Distortion curve

Figure 4.11: (a)-(e) Performance comparison of various methods on *Mandrill* corrupted with AWGN having $\sigma = 10$. (f) Rate-Distortion curve for the proposed methods with *Mandrill* corrupted with AWGN having $\sigma = 10$ as input.

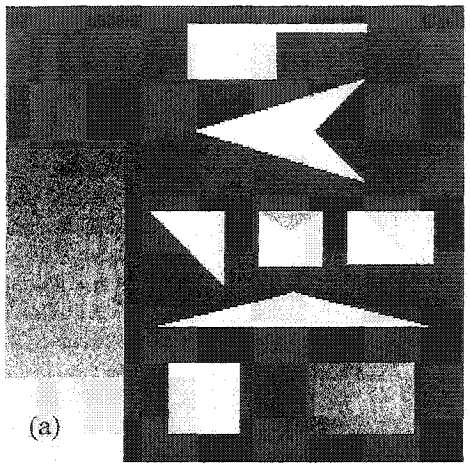

(a) Synthetic Image

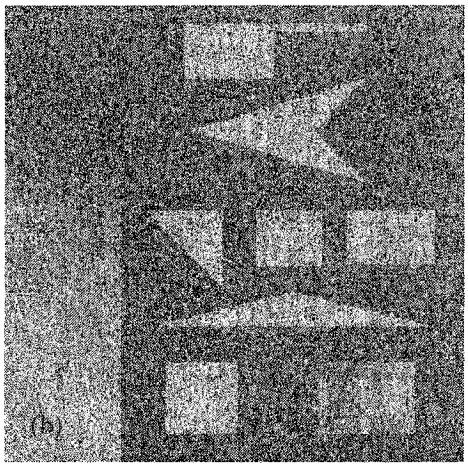

(b) Noisy Synthetic, PSNR = 22.08 dB

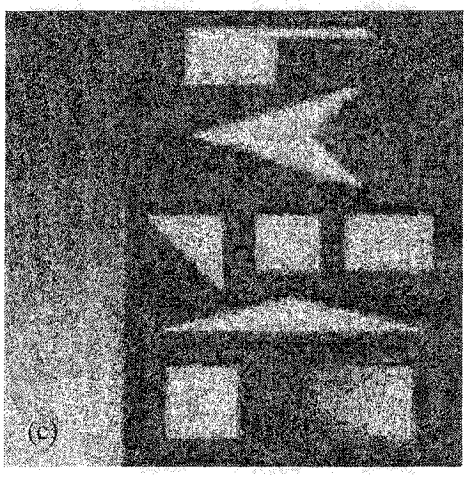

(c) MDLQ, PSNR = 29.34 dB, bpp = 0.44

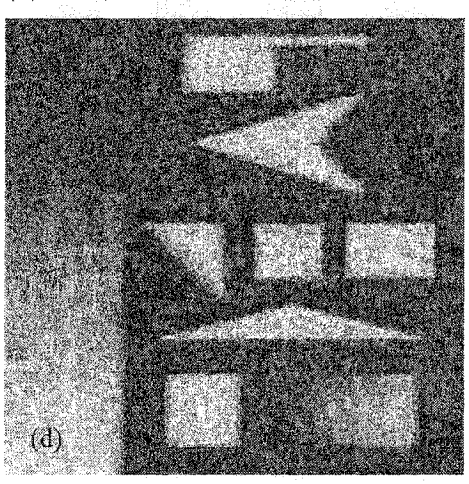

(d) AQ, PSNR = 30.21 dB, bpp = 0.44

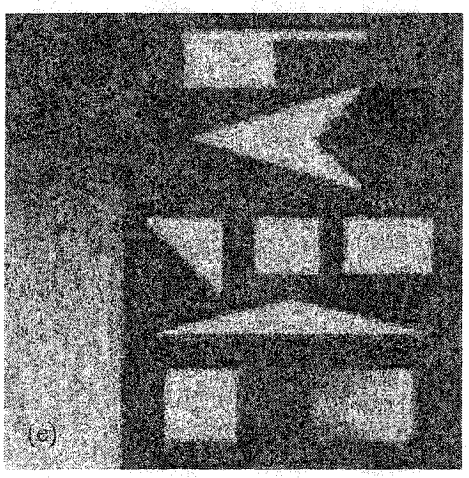

(e) C+AQ, PSNR = 30.68 dB, bpp = 0.44

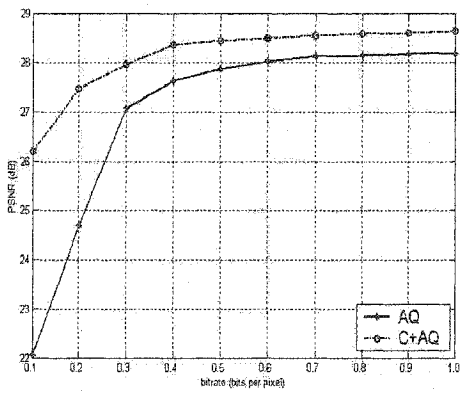

(f) Rate-Distortion curve

Figure 4.12: (a)-(e) Performance comparison of various methods on *Synthetic* corrupted with AWGN having $\sigma = 20$. (f) Rate-Distortion curve for the proposed methods with *Synthetic* corrupted with AWGN having $\sigma = 20$ as input.

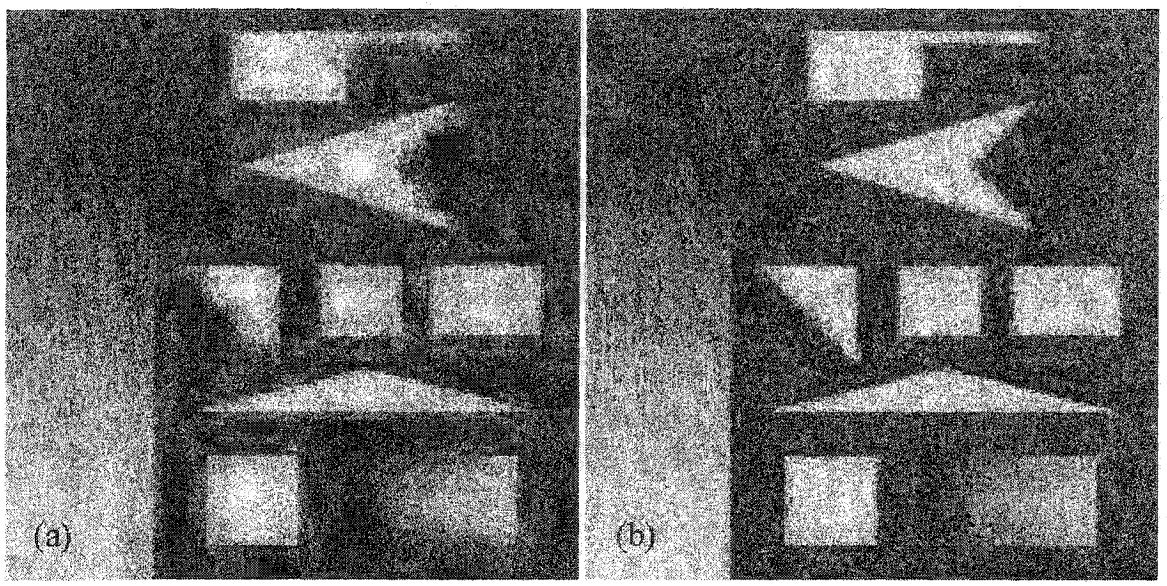

(a) AQ output for sigma=10, bpp=0.3 (b) C+AQ output for sigma=10, bpp=0.3

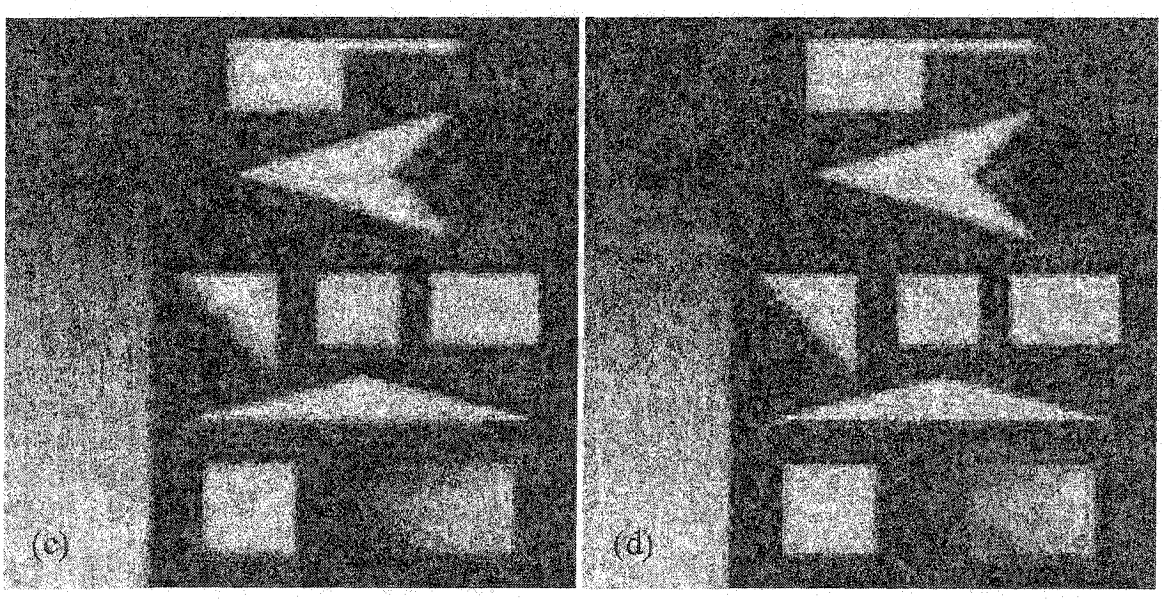

(c) AQ output for sigma=20, bpp=0.3 (d) C+AQ output for sigma=20, bpp=0.3

Figure 4.13: Comparing the effect of classification on the performance of the subband coder having the data and rate adaptive quantizer at its core.

The classification scheme (C+AQ) has been successful in identifying regions of high variability, which have been quantized more finely as compared to AQ and MDLQ and are perceptually more clear. The superior performance of the classified scheme over AQ is visible in Figure 4.13, where the edge regions are much more clear in classified outputs for the same operating criteria. A further improvement in the performance can be achieved by using a better quantizer like a trellis coded one instead of the UTQ and better classification.

Figures 4.8(f), 4.9(f), 4.10(f), 4.11(f) and 4.12(f) show the R-D characteristics of the two proposed schemes for the four images at noise standard deviations of 25, 35, 10 and 20, respectively. At low bit-rates, good rate distortion characteristics are exhibited at all the noise levels shown, with a decrease in the distortion occurring as the output bit-rate is increased. However, as higher bit-rates are approached, further improvement in the PSNR becomes negligibly small. Furthermore, in MDLQ the minimization of the description length has been done over all step sizes and number of quantization levels for each subband to determine the step size for each subband quantizer. In the proposed scheme, this determination of step size is done for all the subbands (or classes) together using the generalized BFOS algorithm [80], thus making the proposed scheme computationally more efficient than MDLQ.

4.8.2 For multiplicative speckle noise

We present our results using two popular 512x512 pixel gray-scale images, *Lena* and *Goldhill*, with various levels of corrupting multiplicative noise as the test data. We also depict the efficacy of our algorithm for medical ultrasound images by choosing an original speckled ultrasound image showing the neonatal brain suffering from white matter damage (leukomalacia), *Brain*. The natural test images are chosen so as to have different amount of detail information. The noise used to corrupt these images is generated using the log-normal distribution described in Section 4.7.2. One of the

Lena	ENL=14		ENL=10		ENL=6	
	PSNR	Bit-rate	PSNR	Bit-rate	PSNR	Bit-rate
Initial PSNR	17.90	8	16.43	8	14.55	8
JPEG	21.39	0.25	19.79	0.37	16.81	0.45
Frost + JPEG	23.98	0.25	24.68	0.37	24.27	0.45
C+AQ	**24.84**	0.25	**25.38**	0.37	**24.93**	0.45

Table 4.7: Performance comparison (in PSNR) for the test image *Lena* corrupted with different multiplicative noise powers.

Goldhill	ENL=14		ENL=10		ENL=6	
	PSNR	Bit-rate	PSNR	Bit-rate	PSNR	Bit-rate
Initial PSNR	18.39	8	16.91	8	14.97	8
JPEG	21.95	0.22	19.86	0.38	17.39	0.34
Frost + JPEG	23.77	0.22	23.29	0.38	21.65	0.34
C+AQ	**24.58**	0.22	**24.45**	0.38	**23.54**	0.34

Table 4.8: Performance comparison (in PSNR) for the test image *Goldhill* corrupted with different multiplicative noise powers.

metrics used to describe the content of the speckle noise in an image is the equivalent number of looks (ENL), which is related to the median of the log-normal distribution [93]. We consider corrupted images with ENL values of 6, 10 and 14.

To assess the performance of the proposed algorithm, we compare it with the compression results produced by the direct application of the JPEG compression [73] to the speckled images. We also compare the proposed scheme with a two-stage approach, where the image is despeckled first and then compressed using the JPEG compression standard. For the despeckling stage we choose the filter given in [95], with a mask size of 5x5. In a detailed comparison of the standard despeckling filters in [93], this filter has been shown to be one of the best despeckling filters. The comparison metric used is the peak signal to noise ratio (PSNR), where the noise considered is present due to the corrupting speckle and the distortion occurring during compression.

As is evident from Tables 4.7 and 4.8, the PSNR resulting from the proposed algorithm at the stated bit-rates are much better than those obtained by the direct

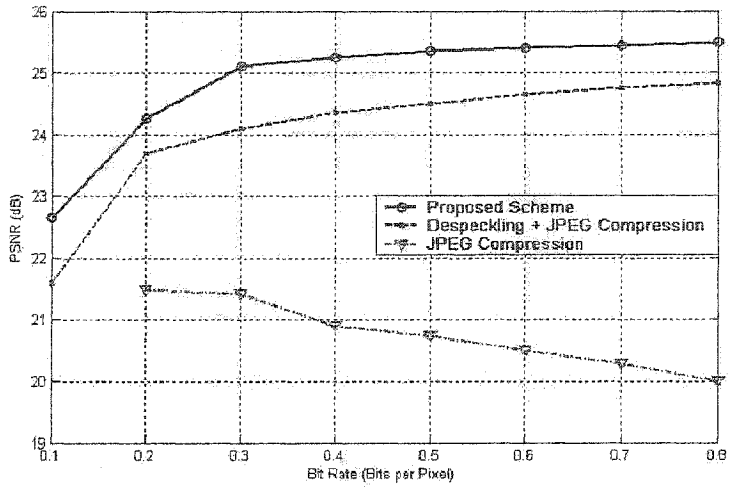

Figure 4.14: Rate-Distortion curves comparing the performance of the proposed scheme with JPEG compression and a two stage scheme wherein the speckled image is first despeckled using Frost filter and then compressed using JPEG compression standard. The comparison has been made for the speckled Lena image with ENL=14 and PSNR=17.90 dB. The 5x5 window has been chosen for the design of the Frost filter.

application of the JPEG compression to the noisy images. As compared to the two-stage compression of the speckled images, the proposed algorithm performs better to the tune of 0.51 dB. The rate-distortion curves for the three compared schemes are shown in Figure 4.14 for a corrupted Goldhill image with an ENL = 12. The proposed scheme performs better than the other two schemes for the compared compression bit-rates. The visual performance of the proposed scheme is also better than the other two as is evident from Figures 4.15 and 4.16.

For the original ultrasound image of the neonatal brain that has been considered (Fig. 4.17), the proposed algorithm manages to reduce the speckle in the image and preserve the edges in the image while compressing it to extremely low bit-rates. The visual performance of the proposed scheme is better than the other two.

(a) Lena Image

(b) Speckled Lena, ENL = 10, PSNR = 16.42 dB

(c) JPEG compression, PSNR = 19.79 dB, bpp = 0.37

(d) Despeckling followed by JPEG compression, PSNR = 24.68 dB, bpp = 0.37

(e) C+AQ, PSNR = 25.38 dB, bpp = 0.37

Figure 4.15: Performance comparison of the proposed scheme with JPEG compression and a two-stage scheme where the speckled image is first denoised and the compressed using the corrupted *Lena* image.

(a) Goldhill Image

(b) Speckled Goldhill, ENL = 6, PSNR = 14.95 dB

(c) JPEG compression, PSNR = 17.39 dB, bpp = 0.34

(d) Despeckling followed by JPEG compression, PSNR = 21.65 dB, bpp = 0.34

(e) C+AQ, PSNR = 23.5 dB, bpp = 0.34

Figure 4.16: Performance comparison of the proposed scheme with JPEG compression and a two-stage scheme where the speckled image is first denoised and the compressed using the corrupted *Goldhill* image.

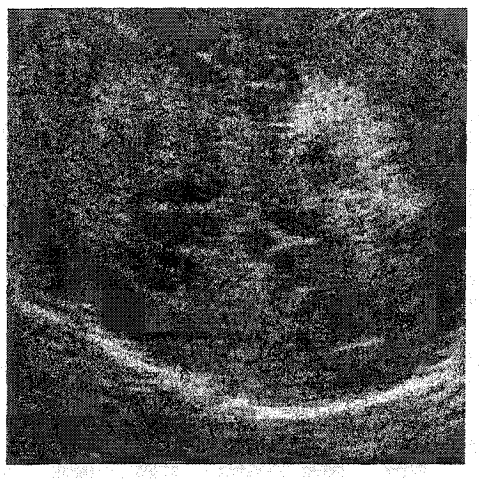

(a) Original speckled Ultrasound image

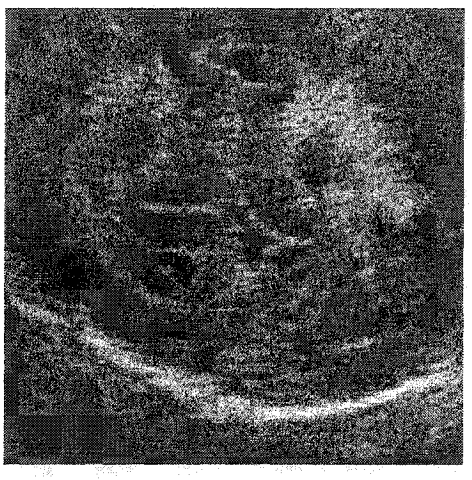

(b) JPEG compression, bpp=0.27

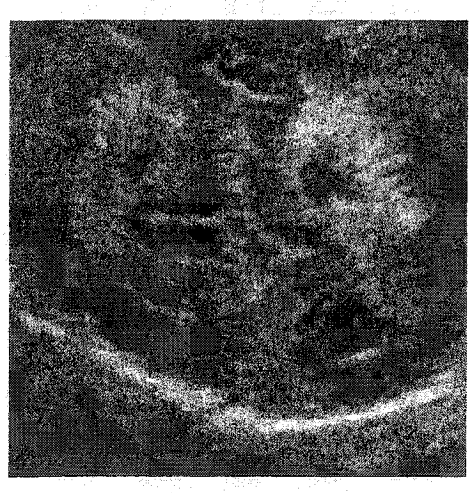

(c) Despeckling followed by JPEG compression, bpp = 0.27

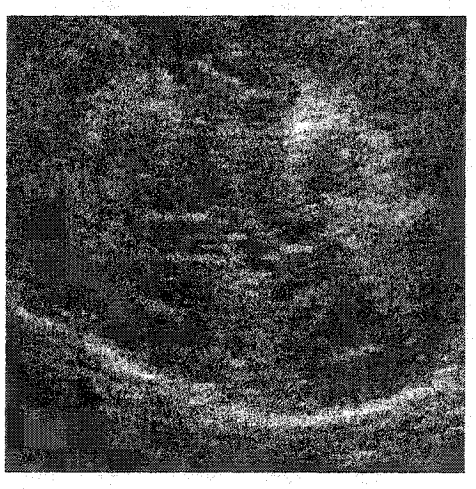

(d) C+AQ, bpp = 0.27

Figure 4.17: Performance comparison of the proposed scheme with JPEG compression and a two-stage scheme where the speckled image is first denoised and the compressed using the original speckle corrupted Ultrasound image, *Brain*.

4.9 Summary

In this chapter we have discussed the problem of joint denoising and compression of images. We have primarily concerned ourselves with the removal of the corrupting additive white Gaussian noise during the process of compression. The development of a simple wavelet domain algorithm has been presented that adapts the zero-zone and the reconstruction levels of a centroid reconstruction UTQ according to the input noise level and the compression rate desired by the user.

We have also presented a context-based classification scheme that classifies the corrupted subband coefficients into different classes based on local activity. Each class has a different variance level and thus, is quantized differently. A class showing more activity, i.e., having a higher variance, is quantized more finely, while a class showing low activity is quantized coarsely, thus resulting in better preservation of image features.

We have further extended the proposed joint denoising and compression algorithm for the removal of multiplicative speckle noise via the use of homomorphic transform. This adapted version of the algorithm has been successfully applied for speckle removal from medical ultrasound images while compressing them.

Experimental results demonstrate that the proposed coder based on the data and rate adaptive quantizer outperforms MDL principle-based scheme and results in a higher PSNR and visually more pleasing images. The proposed classification successfully differentiates between the regions of low and high activity and leads to output images with edges and finer details that are better preserved. We have also shown the application of the adapted scheme for speckle removal while compressing images corrupted with multiplicative speckle noise. The homorphic transform has been used to transform the multiplicative noise into an additive noise. Experimental results show the superior performance of the proposed scheme as compared to standard JPEG compression and a two stage scheme, which performs despeckling and compression of

the input images sequentially.

Chapter 5

Conclusion

In this thesis we have explored the processing of digital images using wavelets. Specifically, we have concentrated on the reduction of noise from images corrupted with additive white Gaussian noise and on the compression of such noisy images in a fashion that simultaneously reduces any corrupting noise in the image. We have also extended the proposed algorithm for joint denoising and compression for the case where multiplicative speckle noise corrupts the original image.

5.1 Conclusion

To denoise an image corrupted with AWGN, we have suggested a simple and adaptive modification of the threshold parameters that utilizes the correlation that exists between the coefficient values at different resolutions. We have validated the adaptation by applying it to two of the most popular threshold selection criteria used for image denoising, viz. *BayesShrink* and *SureShrink*. The following conclusions are evident from the results presented in Chapter 3.

- The proposed scheme uses only the corresponding parent coefficient for each subband coefficient for the purpose of adaptation as opposed to the use of

several neighboring coefficients in the case of context-based schemes.

- Only two parameters, α and β , are used in the scheme. Although the optimal parameter values vary from image to image depending upon the image content, we have experimentally determined an optimal combination for the parameters using an extensive dataset of digital images and a number of different noise powers. From our experiments, the values of $\alpha = 0.43$ and $\beta = 4.3$ yield the maximum average PSNR over the entire dataset.

- The images denoised using the adapted thresholds have a better PSNR and are also visually more appealing than the images denoised using the original thresholds. The number of noise spikes evident in smooth regions of the denoised images is much less for our scheme.

- Since the proposed scheme utilizes only the corresponding denoised parent coefficient, the computational complexity of such a scheme is not much more than that of the original threshold calculation scheme and is much less than the context-based denoising schemes.

In order to jointly denoise and compress an image corrupted with AWGN, we have proposed an adaptive quantizer (AQ) that adapts its zero-zone and reconstruction levels according to the noise level present in the input images and the compression rate required by the user. We have also proposed a classification scheme based on context to raise the performance of the AQ based coder. The features evident from the simulations presented in Chapter 4 are as follows.

- The proposed encoder adapts to the noise level in the input.

- It adapts to the required compression rate.

- In the case where the additive noise is very less or totally absent, it behaves

as an ordinary subband coder compressing the input image according to the desired compression rate.

- The bit allocation among the various subbands is done optimally using the generalized BFOS algorithm.
- The proposed quantizer and encoder lends itself to classification. The proposed context-based classification leads to finer quantization of image areas containing lots of detail and thus yields better visual results.
- AQ works as good as or better than the MDL-based scheme proposed in [11]. The classified encoder (C+AQ) consistently yields much better results, both in terms of the PSNR and the visual quality.
- The computational complexity is of the same order or less as compared to the MDL-based scheme [11].
- We have also extended the proposed joint denoising and compression scheme for multiplicative speckle noise. We have shown its application for the removal of the speckle noise that commonly plagues the medical ultrasound images. Our experiments show that via the use of homomorphic filtering technique, the proposed scheme can be successfully adapted for such an application and can perform better than typical compression methods like JPEG and can also outperform two stage techniques, where the speckle corrupted images are first denoised using a despeckling filter and then compressed using the JPEG compression scheme.

5.2 Future work

One interesting aspect while denoising images in the wavelet domain is the estimation of the noise variance. The median absolute deviation method, generally used and

also followed in this thesis, fails to give an accurate estimation of the variance of the corrupting noise if the input image has a high degree of high frequency content. A more robust and accurate method would lead to a better estimation of the threshold parameter and thus improve the performance of the denoising system.

In the proposed adaptive quantizer, we have used a uniform threshold quantizer as the base model. The use of more sophisticated quantizers, like the trellis coded quantizer, could lead to better quantized outputs, although at the cost of increased computation. The trade-off between the improvement in the performance of the scheme and the increase in computational complexity could be studied.

It would also be interesting to jointly select the noise threshold parameter and the bin width for the quantizer and analyze their inter-dependency. Also, a collection of wavelet bases could be used for the wavelet decomposition instead of one chosen wavelet to allow a better representation of the signals.

References

[1] A. R. Weeks, *Fundamentals of Electronic Image Processing*, SPIE/IEEE Series on Imaging Science and Engineering, SPIE Optical Engineering Press and IEEE Press, 1996.

[2] R. Malladi and J. Sethian, "A unified approach to noise removal, image enhancement, and shape recovery," *IEEE Trans. Image Processing*, 5:1154-1168, 1996.

[3] J. Sethian, *Level Set Methods and Fast Marching Methods: Evolving Interfaces in Computational Geometry, Fluid Mechanics, Computer Vision and Materials Science*, Cambridge University Press, 1999.

[4] A. Chambolle, R. A. De Vore, N. Lee, and B. J. Lucier, "Nonlinear wavelet image processing: variational problems, compression, and noise removal through wavelets," *IEEE Trans. Image Processing*, 7:319-335, 1998.

[5] T. Chan and H. Zhou, "Optimal construction of wavelet coefficients using total variation regularization in image compression," Technical Report in Computational and Applied Mathematics 00-27, UCLA, 2000.

[6] M. Black, G. Sapiro, D. Marimont, and D. Heeger, "Robust anisotropic diffusion," *IEEE Trans. Image Processing*, 7:421-432, 1998.

[7] J. Weickert, B. M. ter Haar Romeny, and M. Viergever, "Efficient and reliable schemes for nonlinear diffusion filtering," *IEEE Trans. Image Processing*, 7:398-410, 1998.

[8] T. Chan and H. Zhou, "Adaptive ENO-wavelet transforms for discontinuous functions," Technical Report in Computational and Applied Mathematics 99-21, UCLA, 1999.

[9] I. Egiazarian, J. Astola, M. Helsingius, and P. Kuosmanen, "Adaptive denoising and lossy compression of images in transform domain," *Journal of Electronic Imaging*, 8(3):233-245, July 1999.

[10] A. Bruce and H. Gao, *Applied Wavelet Analysis with S-Plus*, Springer-Verlag, 1996.

[11] S. G. Chang, B. Yu, and M. Vetterli, "Adaptive wavelet thresholding for image denoising and compression," *IEEE Trans. Signal Processing*, 9(9):1532-1546, Sept. 2000.

[12] R. A. De Vore and B. J. Lucier, "Fast wavelet techniques for near-optimal processing," *IEEE Military Communications Conference*, 1992, pp. 48.3.1-48.3.7, New York.

[13] D. L. Donoho and I. M. Johnstone, "Ideal spatial adaptation via wavelet shrinkage," *Biometrika*, 81:425-455, 1994.

[14] D. L. Donoho and I. M. Johnstone, "Adapting to unknown smoothness via wavelet shrinkage," *Journal of the American Statistical Assoc.*, 90(432), 1200-1224, Dec 1995.

[15] R. T. Ogden, *Essential Wavelets for Statistical Applications and Data Analysis*, Birkhauser, 1997.

[16] B. Vidakovic, *Statistical Modeling by Wavelets*, Wiley Series in Probability and Statistics, John Wiley & Sons, Inc., 1999.

[17] J. B. Weaver, X. Yansun, Jr. D. M. Healy, and L. D. Cromwell, "Filtering noise from images using wavelet transforms," *Magnetic Resonance in Medicine*, 24:288-295, July 1999.

[18] C. Chui, *Wavelets*, Academic Press, 1992.

[19] I. Daubechies, *Ten Lectures on Wavelets*, Philadelphia: SIAM, 1992.

[20] S. Mallat, *A Wavelet Tour of Signal Processing*, Academic Press, 1998.

[21] Y. Meyer, *Wavelets: Algorithms and Applicaions*, SIAM, 1993.

[22] M. Vetterli and J. Kovacevic, *Wavelets and Subband Coding*, Prentice-Hall, 1995.

[23] A. Graps, "An Introduction to wavelets," *IEEE Computational Science and Engineering*, 2(2), 1995.

[24] G. Strang, "Wavelets," *American Scientist*, 82:250-255, April 1994.

[25] B. Vidakovic, "Nonlinear wavelet shrinkage with bayes rules and bayes factors," *J. of the American Statistical Association*, 93:173-179, 1998.

[26] A. Cohen and J. Kovacevic, "Wavelets: the mathematical background," *Proc. IEEE*, 84:514-522, 1996.

[27] S. Mallat, "Wavelets for Vision," *Proc. IEEE*, 84(4):604-614, April 1996.

[28] G. Strang, and V. Strela, "Short wavelets and matrix dilation equations," *IEEE Trans. Signal Proc.*, 43:108-115, 1995.

[29] N. H. Nielsen and M. V. Wickerhauser, "Wavelets and time-frequency analysis," *Proc. IEEE*, 84(4):523-541, April 1996.

[30] A. Cohen, I. Daubechies, J. Feauveau, "Biorthogonal bases of compactly supported wavelets," *Comm. Pure Appl. Math*, 45:485-560, 1992.

[31] G. P. Nason and B. W. Silverman, "The stationary wavelet transform and some statistical applications," in *Wavelets and Statistics*, A. Antoniadis and G. Oppenheim, editors, pp. 281-299, Springer-Verlag, New York, 1995.

[32] E. P. Simoncelli, "Modeling the joint statistics of image in the wavelet domain," in *Proc. SPIE Conf. on Wavelet Applications in Signal and Image Processing VII*, 3813, Denver, CO, 1999.

[33] A. Pizurica, *Image Denoising Using Wavelets and Spatial Context Modeling*, Ph.D. Thesis, Ghent University, 2002.

[34] R. R. Coifman and D. L. Donoho, "Translation-invariant denoising," in *Wavelets and Statistics*, A. Antoniadis and G. Oppenheim, editors, pp. 125-150, Springer-Verlag, New York, 1995.

[35] J. Weaver, Y. Xu, D. Healy, and J. Driscoll, "Filtering MR images in the wavelet transform domain," *Magnetic Resonance in Medicine*, 21:288-295, 1991.

[36] D. L. Donoho and I. M. Johnstone, "Minimax estimation vis wavelet shrinkage," Technical Report, Statistics, Stanford, 1992.

[37] D. L. Donoho and I. M. Johnstone, "Denoising by soft-thresholding," *IEEE Trans. Inform. Theory*, 41(3):613-627, May 1995.

[38] H.-Y. Gao, "Wavelet shrinkage denoising using non-negative garrote," *J. Comp. Grap. And Stat.*, 7:469-488, 1998.

[39] C. Stein, "Estimation of the mean of a multivariate normal distribution," *Annals of Statistics*, 9(6):1135-1151, 1981.

[40] G. P. Nason, "Wavelet regression by cross-validation," Technical Report 447, Department of Statistics, Stanford University, 1994.

[41] M. Jansen, M. Malfait, and A. Bultheel, "Generalized cross-validation for wavelet thresholding," *Signal Processing*, 56(1):33-44, Jan 1997.

[42] N. Weyrich and G. T. Warhola, "Wavelet shrinkage and generalized cross-validation for image denoising," *IEEE Trans. on Image Proc.*, 7(1):82-90, Jan 1998.

[43] F. Ruggeri and B. Vidakovic, "A Bayesian decision theoretic approach to wavelet thresholding," *Statist. Sinica*, 9(1):183-197, 1999.

[44] M. L. Hilton and R. T. Ogden, "Data analytic wavelet threshold selection in 2D denoising," *IEEE Trans. Signal Processing*, 45:496-500, 1997.

[45] S. G. Chang, B. Yu, and M. Vetterli, "Spatially adaptive wavelet thresholding with context modeling for image denoising," in *Proc. IEEE Intl. Conf. on Image Process. (ICIP)*, Chicago, IL, Oct 1998.

[46] S. G. Chang, B. Yu, and M. Vetterli, "Spatially adaptive wavelet thresholding with context modeling for image denoising," *IEEE Trans. Signal Processing*, 9(9):1522-1531, Sept. 2000.

[47] S. G. Mallat and S. Zhong, "Characterization of signals from multiscale edges," *IEEE Trans. PAMI*, 14(7):710-732, July 1992.

[48] Y. Xu, J. B. Weaver, D. M. Healy, and J. Lu, "Wavelet transform domain filters: a spatially selective noise filtration technique," *IEEE Trans. on Image Proc.*, 3:747-758, Nov 1994.

[49] Q. Pan, L. Zhang, G. Dai, and H. Zhang, "Two denoising methods by wavelet transform," *IEEE Trans. Signal Processing*, 47(12), 3401-3406, Dec. 1999.

[50] T.-C. Hsung, D. P.-K. Lun, and W.-C. Siu, "Denoising by singularity detection," *IEEE Trans. on Signal Process.*, 47(11):3139-3144, Nov 1999.

[51] B. M. Sadler and A. Swami, "Analysis of multiscale products for step detection and estimation," *IEEE Trans. Inform. Theory*, 45(3), 1043-1051, Apr. 1999.

[52] J. Ge and G. Mirchandani, "Softening the multiscale product method for adaptive noise reduction," in *37th Asilomar Conference on Signals, Systems, and Computers*, Pacific Grove, CA, USA, Nov. 9-12, 2003.

[53] B. Vidakovic, "Wavelet-based nonparametric Bayes methods," in *Practical Nonparametric and Semiparametric Bayesian Statistics*, Lecture Notes in Statistics 133, Dey. Miller and Sinha, editors, Springer-Verlag, pp. 133-155, 1998.

[54] M. Clyde, G. Parmigiani, and B. Vidakovic, "Multiple shrinkage and subset selection in wavelets," *Biometrika*, 85(2):391-401, 1998.

[55] F. Abramovich, T. Sapatinas, and B. W. Silverman, "Wavelet thresholding via a Bayesian Approach," *J. of the Royal Statist. Society B*, 60:725-749, 1998.

[56] S. Mallat, "A theory for multiresolution signal decomposition: the wavelet representation," *IEEE Trans. Pattern Analysis and Machine Intell.*, 11(7):674-693, July 1989.

[57] M. Antonini, M. Barlaud, P. Mathieu and I. Daubechies, "Image coding using wavelet transform," *IEEE Trans. Image Proc.*, 1:205-220, Feb 1992..

[58] P. Moulin and J. Liu, "Analysis of multiresolution image de-noising schemes using generalized gaussian and complexity priors," *IEEE Trans. Inform. Theory*, 45:909-919, Apr 1999.

[59] E. P. Simoncelli and E. H. Adelson, "Noise removal via Bayesian wavelet coring," in *Proc. IEEE Internat. Conf. Image Proc. (ICIP)*, pp. 379-382, Lausanne, Switzerland, 1996.

[60] Y. Yoo, A. Ortega, and B. Yu, "Image subband coding using context-based classication and adaptive quantization," *IEEE Trans. Image Proc.*, 8:1702-1715, Dec 1999.

[61] H. A. Chipman, E.D. Kolaczyk, and R.E. McCulloch, "Adaptive bayesian wavelet shrinkage," *J. of the Amer. Statist. Assoc.*, 92:1413-1421, 1997.

[62] M. S. Crouse, R. D. Nowak, and R. G. Baranuik, "Wavelet-based statistical signal processing using hidden markov models," *IEEE Trans. Signal Proc.*, 46:886-902, 1998.

[63] G. Fan and X.-G. Xia, "Image denoising using local contextual hidden markov model in the wavelet domain," *IEEE Signal Processing Lett.*, 8(5):125-128, May 2001.

[64] J. K. Romberg, H. Choi, and R. G. Baraniuk, "Bayesian tree structured image modeling using wavelet-domain hidden Markov models," *IEEE Trans. Image Proc.*, 10(7): 1056-1068, July 2001.

[65] M. K. Mihcak, I. Kozintsev, K. Ramchandran, and P. Moulin, "Low-complexity image denoising based on statistical modeling of wavelet coefficients," *IEEE Signal Proc. Lett.*, 6(12):300-303, Dec 1999.

[66] V. Strela, J. Portilla, and E. Simoncelli, "Image denoising using a local Gaussian scale mixture model in the wavelet domain," in *Proc. SPIE, 45th Annual Meeting*, San Diego, July 2000.

[67] J. Portilla, V. Strela, M. J. Wainwright, and E. P. Simoncelli, "Adaptive Wiener denoising using a Gaussian scale mixture model in the wavelet domain," in *Proc. IEEE Internat. Conf. on Image Proc. (ICIP)*, Thessaloniki, Greece, October 7-10, 2001.

[68] M. Malfait, D. Roose, "Wavelet-based image denoising using a markov random field a priori model," *IEEE Trans. Image Proc.*, 6(4):549-565, Apr 1997.

[69] X. Li and M. Orchard, "Spatially adaptive denoising under overcomplete expansion," in *Proc. IEEE Internat. Conf. on Image Proc. (ICIP)*, Vancouver, Canada, Sept. 2000.

[70] A. Pizurica, W. Philips, I. Lemahieu and M. Acheroy, "A joint inter- and intrascale statistical model for wavelet based Bayesian image denoising," *IEEE Trans. Image Proc.*, 11(5):545-557, May 2002.

[71] J. M. Shapiro, "Embedded image coding using zerotrees of wavelet coefficients," *IEEE Trans. Signal Processing*, 41:3445-3462, Dec. 1993

[72] A. Said and W. A. Pearlman, "A new, fast, and efficient image codec based on set partitioning of hierarchical trees," *IEEE Trans. Circuits Syst. Video Technol.*, 6:243-250, June 1996.

[73] W. Pennebaker and J. Mitchell, *JPEG Still Image Data Compression Standard*, New York: Van Nostrand Reinhold, 1994.

[74] S. G. Chang, B. Yu, and M. Vetterli, "Bridging compression to wavelet thresholding as a denoising method," in *Proc. Conf. Information Sciences Systems*, Baltimore, MD, Mar. 1997, pp. 568-573.

[75] M. Hansen and B. Yu, "Wavelet thresholding via MDL for natural images," *IEEE Trans. Inform. Theory* (*Special Issue on Information Theoretic Imaging*), 46:1778-1788, 2000.

[76] J. Liu and P. Moulin, "Complexity-regularized image denoising," in *Proc. IEEE Intl. Conf. Image Processing*, 2:370-373, Oct. 1997.

[77] B .K. Natarajan, "Filtering random noise from deterministic signals via data compression," *IEEE Trans. Signal Processing*, 43:2595-2605, Nov. 1995.

[78] J. Rissanen, *Stochastic Complexity in Statistical Enquiry*, Singapore: World Scientific, 1989.

[79] N. Gupta, E. I. Plotkin and M. N. S. Swamy, "Data and rate adaptive quantization for joint denoising and compression of images," in *Proc.* 37^{th} *IEEE Asilomar Conference on Signals, Systems and Computers*, Pacific Grove, CA, Nov. 2003.

[80] E. A. Riskin, "Optimal bit allocation via the generalized BFOS algorithm," *IEEE Trans. Info. Theory*, 37(2):400-402, Mar. 1991.

[81] N. Farvardin and J. W. Modestino, "Optimum quantizer performance for a class of nonGaussian memoryless sources," *IEEE Trans. Inform. Theory*, 30:485-497, May 1984.

[82] P. Tsakalides, P. Reveliotis and C. L. Nikias, "Scalar quantization of heavytailed signals," *IEE Vis. Image Signal Process.*, 147(5), Oct. 2000.

[83] Y. Shoham and A. Gersho, "Efficient bit allocation for an arbitrary set of quantizers," *IEEE Trans. Acoust., Speech, Signal Processing*, 36:1445-1453, Sept. 1988.

[84] R. L. Joshi *et al.*, "Comparison of different methods of classification in subband coding of images," *IEEE Trans. Image Processing*, 6:1473-1486, Nov. 1997.

[85] Y. Yoo, A. Ortega, and B. Yu, "Adaptive quantization of image subbands with efficient overhead rate selection," in *Proc. ICIP'96*, Lausanne, Switzerland, 1996.

[86] A. K. Jain, *Fundamental of Digital Image Processing*, NJ: PrenticeHall, 1989.

[87] J. W. Goodman, "Some fundamental properties of speckle," *J. Opt. Soc. Amer.*, 66:1145-1150, Nov. 1976.

[88] N. Gupta, M. N. S. Swamy, and E. I. Plotkin, "Despeckling of medical ultrasound images using data and rate adaptive, lossy compression," submitted to *IEEE Transactions on Medical Imaging*, Oct. 2003.

[89] X. Zong, A. F. Laine, and E. A. Geiser, "Speckle reduction and contrast enhancement of echocardiograms via multiscale nonlinear processing," *IEEE Trans. Med. Imag.*, 17:532-540, Aug. 1998.

[90] A. Achim, A. Bezerianos, and P. Tsakalides, "Novel Bayesian multiscale method for speckle removal in medical ultrasound images," *IEEE Trans. Med. Imaging*, 20(8), Aug. 2001.

[91] C. Oliver and S. Quegan, *Understanding Synthetic Aperture Radar Images*, Norwood, MA: Artech House, 1998.

[92] A. C. Frery, H. J. Muller, C. C. F. Yanasse, and S. J. S. Sant'Anna, "A model for extremely heterogenous clutter," *IEEE Trans. Geoscience Remote Sensing*, 35:648-659, May 1997.

[93] L. Gagnon and A. Jouan, "Speckle filtering of SAR images a comparative study between complexwavelet based and standard filters," *SPIE Proc.*, no. 3169, pp. 8091, 1997.

[94] A. Achim, P. Tsakalides, and, A. Bezerianos, "SAR image denoising via Bayesian wavelet shrinkage based on heavytailed modeling," *IEEE Trans. Geoscience Remote Sensing*, 41(8):1773-1784, Aug. 2003.

[95] V. S. Frost, J. A. Stiles, K. S. Shanmugan, and J. C. Holtzman, "A model for Radar images and its application of adaptive digital filtering of multiplicative noise," *IEEE Trans. Pattern Anal. And Mach. Intelligence*, 4:157-166, 1982.